2018

Isotope Based Superconductors for Fusion Application

Hyunseock Jie
University of Wollongong

UNIVERSITY
OF WOLLONGONG
AUSTRALIA

Isotope Based Superconductors for Fusion Application

Hyunseock Jie

Supervisors:
Dr. Md Shahriar Al Hossain
Prof. Shi Xue Dou
Prof. Jung Ho Kim
Dr. Vladimir Luzin

The University of Wollongong

School of Physics

May, 2018

Abstract

At present, the design of the International Thermonuclear Experimental Reactor (ITER) project involves a superconducting magnet system that is based on NbTi and Nb_3Sn. The system consists of 18 Nb_3Sn Toroidal Field (TF) Coils, a 6 module Nb_3Sn Central Solenoid (CS), 6 NbTi Poloidal Field (PF) Coils, and 9 NbTi pairs of Correction Coils (CCS). In the current ITER plan, 112 tonnes of Nb_3Sn superconducting magnets will be used. Despite outstanding high magnetic field properties, the current superconductor solution, Nb_3Sn, is not ideal and has several drawbacks.

First and foremost, Nb based superconductors must be cooled down to 4 K using very expensive and not-readily-available liquid helium. The world shortage of helium supplies is an inherent issue, as helium resources are limited and recovery following use is unsustainable and unreliable. Secondly, if the 10 mSv/h requirement for the remote handling of recycling, set by ITER, is to be satisfied, there will be an impact on the maintenance and radioactive waste treatment schedules. Therefore, it is critical to consider the radio activation of components such as superconducting magnets over time within the fusion reactor from the viewpoints of radiological and environmental pollution. This implies that thicker shielding is necessary in front of the Nb based superconducting magnets if long-term operation is considered. Therefore, it is essential that all of the components within the fusion reactor should be composed of low-activation materials. Lastly, a practical test using the SULTAN facility (PSI, Switzerland) on Nb_3Sn based cables demonstrated that they have limited reliability. In this test, the deterioration of superconducting properties was observed at magnetic field/ current cycling that was 10 times lower than the required target, and there was mechanical degradation. Mechanical degradation has been proved to be the reason why the mechanical properties need to be improved. Therefore, alternative solutions for decreasing these drawbacks are in demand.

The aim of this thesis was to study and demonstrate the possibility of using $Mg^{11}B_2$ superconducting material for fusion reactor application because of its ideal properties. MgB_2 has a higher critical temperature (T_c = 39 K), which means that the cryogenic system does not necessarily require a cryogenic agent. Indeed, MgB_2 superconductors have acceptable performance at a temperature as high as 20 K, while the conventional superconductors require 4.2 K. It has a simple binary crystal structure, is a chemically stable compound, and has a relatively low manufacturing cost and lower specific gravity. In terms of the boron precursor, natural boron has the following isotopic ratio: 19.78wt% boron-10 (^{10}B) and 80.22wt% boron-11 (^{11}B), and it is used as a neutron absorption material. ^{10}B is easily transformed to ^{7}Li and He by the (n, α) reaction ($^{10}B + n \rightarrow {}^{7}Li + He$ (gas)), which results in reduction of the MgB_2 volume fraction. Unlike ^{10}B, ^{11}B does not react with neutrons and is stable in the neutron irradiation environment. Thus, if the ^{11}B based precursor is used instead of natural boron, MgB_2 has a low-activation property, and it will be the most suitable superconducting material for the radioactive environment.

In this thesis, the in-situ powder-in-tube (PIT) process using ^{11}B isotope powder as the boron precursor is introduced, and we believe that it is the best fabrication method for forming low-activation MgB_2 superconducting wire for fusion reactor application. Because the critical current

performance of the ^{11}B based MgB_2 ($Mg^{11}B_2$) is still low, attempts must be made to overcome and investigate the mechanism responsible to improve its current carrying capability. For the best superconducting properties, the fabrication procedure was modified by using cold high pressure densification (CHPD) combined with hot isostatic pressing (HIP), and doping with carbon. The results showed that the densification technique should represent a promising alternative innovative manufacturing method for industrial production of practical MgB_2 wires with outstanding critical current density, J_c. Glycine-doped $Mg^{11}B_2$ bulk superconductor was synthesized from isotopic ^{11}B powder to enhance the high field properties compared with natural boron based MgB_2 superconductor. Indeed, the evolution of the microstructure and corresponding superconducting properties were systematically investigated by controlling the manufacturing conditions. Furthermore, the critical issue related to the residual stress in the $Mg^{11}B_2$ wire has been studied in this thesis. This is because the behavior of the residual stress/ strain would be expected to affect the mechanical properties and have a detrimental effect on the critical current in the superconducting wire, along with the construction and manufacturing conditions of the superconducting magnet. Thus, the neutron diffraction analysis method was introduced, and we examined the residual stress in the $Mg^{11}B_2$ wire.

In summary, we have performed both experimental and analytical studies to understand the stress/strain behavior and the related mechanical properties that are correlated with superconducting properties to anticipate future unwanted damage to the $Mg^{11}B_2$ superconducting wire. We believe that this thesis work can contribute to the enhancement of our fundamental knowledge of the residual stress in superconducting wire and the links among the stress, the microcracks, and the superconducting properties deterioration in one unifying micromechanical mechanism.

Acknowledgments

Many people have contributed to the work presented in this thesis, and I would like to express my sincere gratitude to all of them. First things first, I would like to thank my principal supervisor Dr. Md Shahriar Al Hossain for his guidance, advice, support, and encouragement. I have come to know him as a person with various talents and full of enthusiasm in research, discussions, and teaching. He has always provided me with fresh and interesting research ideas, and it is never a waste of time for me. It has been really a great pleasure and a special experience to work for him. In parallel, I would like to thank my principal supervisor Dr. Vladimir Luzin at the Australian Nuclear Science & Technology Organisation (ANSTO). He has always been ready to discuss experimental results, theories, and computation. Indeed, he introduced me to the neutron diffraction analysis method with computational analysis, which I had never experienced. I will never forget his thoughtful discussions and support to understand and resolve stress/strain behavior.

Secondly, I would like to thank my co-supervisor Professor Jung Ho Kim for introducing me into the Institute for Superconducting and Electronic Materials (ISEM). It is a great pleasure to express thanks for his careful correction of the manuscript of my first year proposal review and its presentation. I also want to thank Dr. Keun Hwa Chae for his unconditional and unlimited support to complete experiments in the Pohang Accelerator Laboratory (PAL) and the Korea Institute of Science and Technology (KIST). Thanks for always helping me. I would also like to extend my gratitude to the following professors: Prof. S. X. Dou, Prof. Yusuke Yamauchi, and Assoc. Prof Konstantin Konstantinov, and also to Dr. Xun Xu for serving on the examination committee for my first year proposal review presentation.

I owe great thanks to Dr. Jeonghun Kim for his meaningful research discussions as a colleague and collaborator. It has been a great experience to work with other group members who have given me essential assistance. I always enjoyed the discussions and the relationships with my colleagues: Mr. Wenbin Qiu, Mr. Hiroki Kobayashi, Mr. Sudipta Pramanik, Dr. Özlem Cicek, Dr. Dipakkumar J. Patel, and Dr. Zongqing. I would like to offer special thanks to Mr. Jaecheol Choi, Mr. Shunsuke Tanaka, Mr. Jaewoo Lee, Mr. Hyungil Choi, and Mr. Kyubin Shim for their kind help and all our discussions. I would like to express my gratitude to all AIIM facility officers and staffs including Mrs. Narelle Badger, and Mrs. Crystal Mahfouz for administrative support, and Mrs. Joanne George and Dr. Candace Gabelish for procurement and safety related support.

Finally, I would like to thank my parents and friends who have encouraged me and supported me during my studies.

Certification

I, Hyunseock Jie, declare that this thesis submitted in fulfilment of the requirements for the conferral of the degree Doctor of Philosophy, from the University of Wollongong, is wholly my own work unless otherwise referenced or acknowledged. This document has not been submitted for qualifications at any other academic institution.

_____

Hyunseock Jie
13th May 2018

Table of Contents

List of Figures

List of Tables

Chapter 1

Introduction

1.1. General Overview

The superconductor has played a significant role in the development of efficient power transmission technology [1], alternative energy resources [2] and magnetic resonance imaging (MRI) [3]. For reliable design of long distance transmission, nuclear fusion power generators, and liquid-helium-free cooling systems, superconductors always have called for a deep understanding of the cost, performance, engineering, and cryogenics, all indispensable. Therefore, it has become important to discover new reliable superconducting materials. At the same time, the development of advanced cryogenic techniques is necessary to make the next-generation superconducting magnet [4]. Currently, magnesium diboride (MgB_2) has become one of the most promising superconducting materials because of its several advantages. It has a simple crystal structure [5], reasonable mechanical properties [6], moderately high superconducting critical temperature (Tc) [7] and a potentially high upper critical field [8]. In addition, from the cost-effectiveness point of view, MgB_2 has low cost [9] and low weight compared with other superconducting materials [10]. Therefore, it goes without saying that MgB_2 is able to make use of new liquid-helium-free cryogenic apparatus in applications such as MRI and kilometer- scale power lines for transmission without power dissipation.

For the next-generation fusion reactor, MgB_2 that is fabricated using the boron isotope ^{11}B, instead of the neutron absorbing isotope ^{10}B, has also been considered the most promising material [11]. The present design of the International Thermonuclear Experimental Reactor (ITER) involves a magnet system that is based on Nb_3Sn or Nb-Ti [12]. In the case of Nb_3Sn, it must be cooled down to 4 K and produces abundant radioactive waste [13]. On the other hand, $Mg^{11}B_2$ has lower induced radioactivity, a higher critical temperature (40 K), and reliable properties for low to mid field magnets operating at temperatures as high as 20 K [13, 15].

As mentioned above, the MgB_2 superconducting material allows us to develop advanced power transmission, magnetic resonance imaging, cooling equipment, and nuclear fusion power generators. Based on those application areas, most of my research has been focused on the fabrication and characterization of MgB_2 superconductor by using the boron isotopes ^{10}B and ^{11}B.

1.2. Superconductivity

1.2.1. Superconducting Theory

A superconductor is a material, metallic alloy, or compound that will conduct electricity or transport electrons without resistance below a critical temperature. Electrical resistance is an undesirable factor because it gives rise to losses in the energy flowing through the material.

Scientists refer to superconductivity as a macroscopic quantum phenomenon [16]. In 1911, superconductivity was first discovered in mercury by Heike Kamerlingh Onnes, a Dutch physicist. When he cooled it down to the temperature of liquid helium, 4 degrees Kelvin (-452 °F, -269 °C), its resistance disappeared. The Kelvin scale represents an "absolute" scale of temperature [17]. Thus, it was necessary for Onnes to come within 4 degrees of the coldest temperature that is theoretically attainable to witness the phenomenon of superconductivity. Later, in 1913, he won a Nobel Prize in physics for his research in this area [18].

1.2.2. The Critical Surface of Superconductor

Excluding temperature (*T*), superconductivity is also influenced by the electric current density (*J*) inside the superconductor and the surrounding magnetic field (*H*). In other words, the critical magnetic field (H_c) and the critical current density (J_c) are also two significant factors used to evaluate the performance of a superconducting material. In the superconducting material, a three-dimensional (3-D) dome-shaped surface, known as “the critical surface”, can be drawn as a function of the three parameters (*T*, *H*, *J*) on three axes. As shown in Figure 1-1, the material will have superconductivity as long as it stays within the 3-D (*T*, *J*, and *H*) volume.

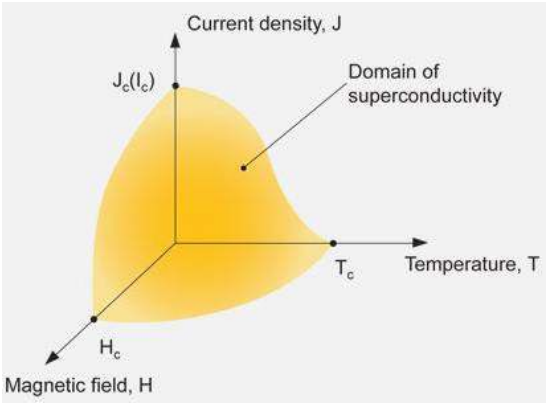

Figure 1-1. The ideal critical surface of a superconductor [19].

1.2.3. Meissner Effect

The Meissner effect is a phenomenon in which a magnetic field penetrating the inside of a superconducting material is pushed out to the outside as the material makes a transition to the superconducting state. In the superconducting state, magnetic fields cannot penetrate into the material [20]. This is related to the complete diamagnetism of a superconductor, and it is one of the distinguishing characteristics of a superconductor. Since the discovery of superconductors by the Dutch scientist Onnes in 1911, more than two decades later, in 1931, this phenomenon was discovered by the German physicist Walter Meissner [21].

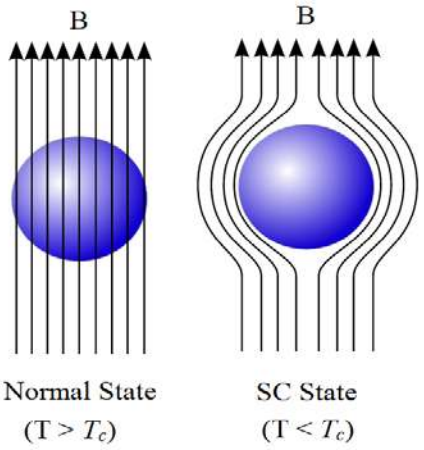

Figure 1-2. Diagram of the Meissner effect [21].

When a magnetic field is applied to a material having an electrical resistance of zero, a shielding current is induced by Lenz's law. This shielding current flows on the material surface. The magnetic field is the same size as the magnetic field that is applied, but it points in the opposite direction to cancel the applied magnetic field, so it cannot penetrate inside the original magnetic field lines, as shown in Figure 1-2 [21]. The superconductor also satisfies this phenomenon because the electric resistance is zero. That is, the magnetic flux permeating the inside of the material having electrical resistance of 0 is preserved, even if an external magnetic field is applied. However, the Meissner effect found in 1931 showed that the magnetic flux inside the superconductor was not simply conserved to a constant value, but was kept at zero [22]. When a material makes a transition to the superconducting state, any existing magnetic field lines are expelled, unlike the perfect diamagnetism case, and if any magnetic field smaller than the critical magnetic field is applied from the outside, the superconductor pushes all of it out, and there is no magnetic flux to penetrate. The difference between a state where the electric resistance is simply 0 and a superconductor having a Meissner effect appears here [23].

1.2.4. London Penetration Depth (λ_L)

Deriving the equation for magnetic flux density B by London's equation gives $\nabla^2 B = B/\lambda_L^2$ [24]. However, ∇^2 is a differential computation with respect to the position coordinates and is called the Laplacian. λ_L is an integer peculiar to the superconductor. In order to simplify the explanation, the following equation can be obtained by solving one-dimensional equations.

$$\frac{\partial^2 B}{\partial x^2} = \frac{B}{\lambda_L^2} \tag{1.1}$$

Assume that there is a superconductor at $x > 0$, where $x < 0$ is the vacuum and that a magnetic flux

density B_0 exists. In this case, the above equation can be solved simply, and $B = B_0 exp\ (-x / \lambda_L)$. This equation shows that the magnetic flux density decreases exponentially in the superconductor as shown in the figure. λ_L is called the London penetration depth. At the distance λ_L, the magnetic flux density becomes *1/e* of the value in vacuum (e = 2.718) [25]. The form of λ_L, *London Penetration Depth* was symbolized as following equation (1.2).

$$\lambda_L = \sqrt{\frac{m}{\mu_0 n q^2}} \qquad (1.2)$$

Where m, n, and q stand for the mass, number density and charge of charge carriers, respectively. It can be seen that λ_L depends on the total number of electrons in the superconductor, but is usually about 10^{-8}m (1 / 100,000th of a millimeter), and the magnetic flux density hardly penetrates into the superconductor [25]. That is, it shows the Meissner effect. Since the dimensions of a normal superconductor are much longer than both the length and the length of the penetration distance, the presence of the penetration layer is virtually negligible by design.

1.2.5. Coherence Length (ξ) with Type I & Type II superconductors

The coherence length (ξ) means both the characteristic Cooper pair size in the superconductor and the length of the fluctuation of the wave function of the electron. In addition, the term coherence is used to describe the pattern in which a group is exercising in union as a whole, even though the individual movements are slightly different in time, as in a regular wave [26]. Electrons in superconductors, superfluid helium, and laser light are all in various forms of motion of this type. There are two types of coherence length used in superconductivity. One of them is called the path of coherence of Pippard, which is often represented by the symbol ξ_0 [27]. In a superconductor, two electrons have a correlation and form a number of bound electron pairs (Cooper pairs) with the same momentum. Furthermore, each Cooper pair will spread in order to maintain the distance between the two electrons, which is called the coherence length. In short, if one electron is found at a certain point, then the other electron paired with it is highly likely to be found in a sphere of radius ξ_0 centered at this point. ξ is a measure of the spatial variation of the wave function with respect to superconducting electrons. and describes the structure of the middle portion between the superconducting region and superconducting region in contact with each other and ξ depends on the temperature T as shown in Equation (1.3).

$$\xi = 0.74\xi_0 \left\{1 - \frac{T}{T_C}\right\}^{-\frac{1}{2}} \qquad (1.3)$$

Where T_c is the critical temperature, ξ is close to ξ_0 at absolute zero, but it becomes longer as the temperature rises. A longer ξ means weaker superconductivity [28].

Superconductors can be classified into *Type I* and *Type II* depending on their properties. *Type I* superconductor has superconducting transition that occurs instantaneously, and a *Type II* superconductivity is a superconductor with a gradual transition to superconductivity. The distinction between *Type I* and *Type II* can be explained by the ratio of the penetration depth to the coherence length, with ξ and λ, which are based on the Landau theory. The penetration depth divided by the coherence length is called the Ginzburg-Landau coefficient ($\kappa = \lambda/\xi$), and it is usually used to distinguish the superconductor Type. *Type I superconductors* are those with $0 < \kappa < 2^{(-1/2)}$, and *Type II superconductors* are those with $\kappa > 2^{(-1/2)}$ [29, 30].

1.2.6. Bardeen-Cooper-Schrieffer (BCS) Theory

The Barden-Cooper-Schrieffer (BCS) theory is the theory that first explained the superconducting phenomenon as a microscopic process. The Bardeen, Cooper, and Schrieffer (1956) theory was named after John Bardeen, Leon Cooper, and John Robert Schrieffer of the University of Illinois in the United States, who devised it in 1957 [31]. The BCS theory explains the phenomenon of superconductivity, that suddenly the resistance becomes zero when a certain type of conducting material approaches zero degrees of absolute temperature. The three scientists won the 1972 Nobel Prize for Physics for their work on BCS theory [32]. In order to realize the superconducting state, the electromagnetic field must be in a coherent state. The electrons in the material are charged, however, and there is always a resistance between two electrons because they repel each other. The basis of the BCS theory is that the Cooper pairs of electrons in the superconductor are bosons and draw together to form a condensate. This phenomenon of the superconducting state is called the electron-phonon interaction because of the coupling of electrons to the vibrating crystal lattice (phonons) and occurs below the critical temperature (T_c) of the superconductor [33]. That is, when a negatively charged electron passes, a positively charged cation is attracted in the electron direction and moves in that direction. Since the mass of the cation is much heavier than that of the electron, the cation continues to move in the same direction, and the electrons are continuously attracted to the cation direction, so that one electron is apparently attracted to another electron. The BCS theory attempts to explain the mechanism of superconducting states by providing an explanation, that electrons present in a solid can overcome electron repulsion through the phonons and attract each other.

1.3. MgB_2 Superconductor

1.3.1. Crystal Structure

As an AlB_2 type crystal, MgB_2 has a hexagonal crystal structure with lattice parameters a = 3.08 Å and c = 3.51 Å (P_6/mmm space group), which is common among the diborides [34]. The crystal structure is described in Figure 1-3. The boron atoms form graphite like honeycomb network and

the Mg atoms are located at the pores of these hexagons. Each magnesium atom located at the centre of a hexagon formed by boron donates an electron to the boron planes. Thus the B-B bonding is strongly anisotropic [35]. This structure has peculiar two-dimensional (2D) honeycomb layers formed by boron atoms. Those graphite-like boron layers are sandwiched by the triangular metal layers as shown in Figure 1-3. Each magnesium atom is at the center of a hexagonal prism of boron atoms at a distance of 2.5 Å. Each boron atom is surrounded by three other boron atoms, forming an equilateral triangle at a distance of $a/\sqrt{3} \sim 1.78$ Å, and the Mg-Mg distance in the plane is same as the lattice constant a [36]. Because the lattice constants a and c in the AlB_2-type structure are in the range of 3.0–3.2 Å and 3.0–4.0 Å, MgB_2 has the middle lattice constants among this type of structure [37].

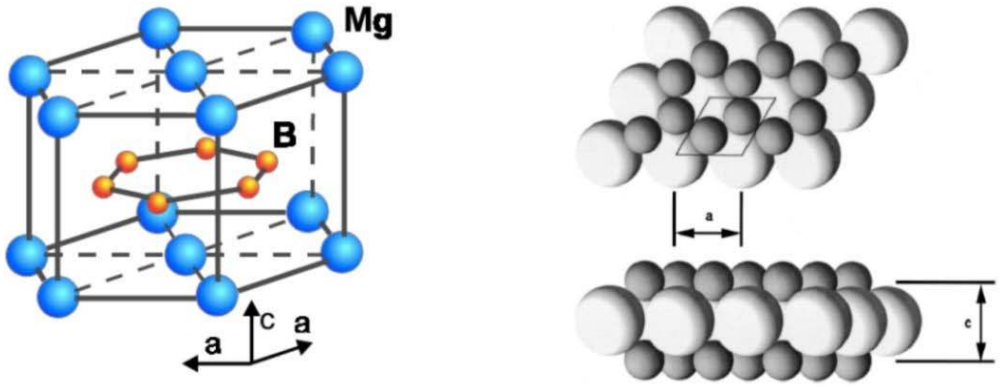

Figure 1-3. The structure of MgB_2 containing graphite-type B layers separated by hexagonal close-packed layers of Mg [38].

1.3.2. Superconducting Properties in MgB_2

Among the BCS based or intermetallic compound superconductors, MgB_2 exhibits the highest critical temperature of T_c = 39 K [39]. The high transition temperature aroused great interest in this material, and the superconductivity of MgB_2 has been extensively studied [40, 41]. MgB_2 has each of its elements aligned in two-dimensional planes, and the material is therefore expected to have two-dimensional superconductivity as a result of its crystalline structure. In conventional superconductors, the electron-phonon interaction creates Cooper pairs of approximately equal pair strength, distributed evenly over the band. The 2D σ band on the boron layer is responsible for the superconductivity [42, 43]. The high T_c value and the application temperature of MgB_2 (around 25 K) can be achieved by using various cooling methods such as refrigerators, liquid H_2, and even a novel solid N_2 cooling system [44]. Thus, the general cryogen liquid He, which is extremely expensive, can be easily replaced. Indeed, compared to the strong anisotropy, as high as 5 – 7, of a high temperature superconductor (HTS) such as $YBa_2Cu_3O_{7-y}$, the anisotropy of MgB_2, as low as 1.5 − 5 is considered to be another advantage in practical applications [45]. For example, MgB_2 enables a more simplified manufacturing procedure than in the case of HTS materials. In addition,

it has a large coherence length, so that the weak-link problem, which is considered as the foremost factor in fabrication of HTS, is no longer crucial in MgB_2 [46]. As a result of using boron and magnesium as precursors, low cost is another advantage that promotes the economic development of MgB_2 conductors. Numerous fields of applications including strong current and weak current ones are expected to utilize MgB_2 superconductors as the primary material, such as magnetic resonance imaging (MRI), transformers, generators, flywheel energy storage, and superconducting quantum interference devices (SQUIDs) [47, 48].

1.3.3. Fabrication of the MgB_2 Superconductor

1.3.3.1. Powder-In-Tube (PIT) Technique

The powder-in-tube (PIT) technique is a standard method for manufacturing superconducting wires, especially for long-length wires [48, 49]. In this method, the first step is filling a suitable tube with Mg + B powder, which is the precursor of the boron and Mg. Then the entire tube is drawn or rolled into a wire or tape with the designed size and shape. The final step is heat-treatment in order to form the MgB_2 phase from the mixed boron and Mg precursors. The PIT MgB_2 wire manufacturing method can be divided into two routes. In an in-situ method as the first sort of PIT method, stoichiometric Mg and B powders are used as precursors and filled into a metallic tube (Cu, Nb, Ag, Ti, Fe, stainless steel, Monel alloy, etc.). In the case of ex-situ method, instead of un-reacted Mg and B powder, already formed MgB_2 powder is used as the filling powder. In this work, in-situ was chosen as the type of route.

1.3.3.2. Internal-Magnesium-Diffusion (IMD) Method

The existence of unwanted high porosity caused by the PIT technique is known to be one of the most detrimental factors in J_c performance in MgB_2 superconductors. The phenomenon is almost unavoidable in fabricating MgB_2 wires by using the PIT method [50]. In order to overcome the weakness of the PIT method, an innovative method called the internal Mg diffusion (IMD) technique was invented [51]. The IMD technique is a variant of the in situ PIT technique for MgB_2 conductor fabrication. In the IMD process, an Mg rod is embedded axially in a tube filled with B, which is then followed by wire drawing and heat treatment [51]. Compared to the conventional in situ PIT process, which yields a system of randomly connected MgB_2 fibres associated with copious porosity, an IMD process can produce a dense MgB_2 layered structure with excellent longitudinal and transverse connectivity [52]. Through this process, porosity will be substantially avoided, and high transport properties can be achieved [53].

1.4. Boron Isotope Based Superconductor for Fusion Application

1.4.1. Critical Issues for use in Fusion Application

The stable boron isotopes are classified by their nuclear mass, magnetic moment, and thermal neutrons capture cross-section. The relative atomic masses of ^{10}B and ^{11}B are equal to 10.012938 and 11.009305 amu (with weighted mass of 10.811 amu for the boron natural isotope composition of approximately 19.9 % ^{10}B + 80.1 % ^{11}B) [54]. The nuclear-spin quantum numbers and nuclear magnetic moments (in nuclear magnetons) of ^{10}B and ^{11}B are equal to 3 and 3/2, and 1.8006 and 2.6886, respectively [55]. According to the data on the neutron scattering lengths and cross-sections of the elements and their isotopes, the total scattering cross-sections for ^{10}B, ^{11}B, and natural boron are equal to 3835, 3.10, and 5.77 barns, respectively [56, 57]. These meaningful differences among boron isotopes allow us to research and use boron isotope effects, such as in isotopic elemental boron structural modifications and its chemical compounds [58].

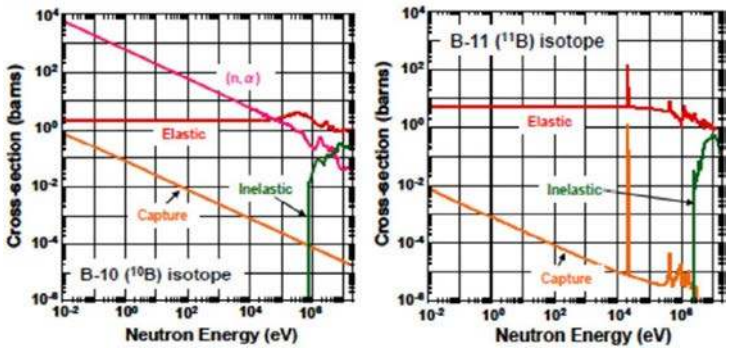

(a) (b)

Figure 1-4. Neutron cross-section of boron isotopes: (a) ^{10}B and (b) ^{11}B [59].

Commercial natural boron powder consists of two types of isotopes, boron-10 (^{10}B; 18.98 %) and boron-11 (^{11}B; 81.02 %) [60-62]. ^{10}B isotope powder (bulk) is usually used as a neutron absorber in nuclear power plants, such as for radiation shields and control rods. (^{10}B has a large neutron absorption cross-section.) The stable isotopes of boron ^{10}B and ^{11}B differ by the addition of a single neutron in the $1p^{3/2}$ shell in the nucleus. The neutron capture cross-section and ability to capture neutrons of ^{10}B strongly surpass those of ^{11}B. The classical Mayer–Jensen shell model dynamics did not offers explanation as to how the presence / absence of a single neutron in the $1p^{3/2}$ shell could result in such large difference in the neutron cross-section between these two stable isotopes [63-65]. The Brightsen nucleon cluster model, however, explained the large cross-section for ^{10}B compared with the small cross-section for ^{11}B as resulting from cluster dynamics, besides the complete balance of total spin dynamics, in particular, from the presence / absence of the ^{3}He cluster [66]. And also, ^{10}B is easy to transform to ^{7}Li and He by the (n, α) reaction. (^{10}B +

n → ^{7}Li + ^{4}He + 2.74 MeV). For these reason, ^{10}B cannot guarantee the stability of the MgB_2 superconducting magnet [67-71]. The ^{11}B is stable under neutron irradiation, being without the (n, α) reaction, and can reduce nuclear heating. (2.58 → 0.13 W/cm^3), so that ^{11}B isotope precursor is a desirable material as the boron source for low activation MgB_2 wire [72-77]. From the practical application point of view, by replacing ^{10}B with the isotope ^{11}B or ^{11}B enriched boron precursor, $Mg^{11}B_2$ superconducting wires will be much more stable in a neutron irradiation environment due to the smaller neutron capture cross-section of ^{11}B.

1.4.2. Introduction of Boron

Boron, the fifth element of the periodic table, was discovered as an element in 1808 and manufactured as a pure material from 1909 [78]. Generally, pure boron does not exist naturally because of its chemical reactivity, and it has a variety of unusual compounds [78, 79]. Overall, boron element still remains an attractive element in worldwide scientific interest due to its peculiar properties, such as its unexplained thermodynamic stability, [80-82] pressure induced metallization and superconductivity [83-87], unique chemical bonds [88-89], and other properties useful in technical applications. Boron has a great diversity of allotropes, 16 in total [90]. Among the elemental boron allotropes, only α- and β-rhombohedral (α-B_{12} and β-B_{105}), and γ-orthorhombic boron (γ-B) have been currently established as pure phases and confirmed to be thermodynamically stable [91-93], although the stability of α- rhombohedral boron and β-rhombohedral boron under ambient conditions still remains a controversial issue.

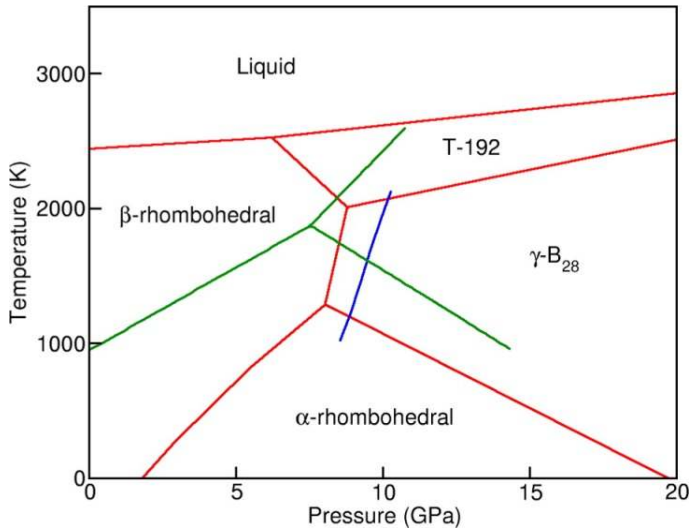

Figure 1-5. Phase diagram of elemental boron published in recent reports. These reports yield a consistent energy ordering of the different phases [94].

According to Fig. 1-5, liquid boron is transformed to the β-rhombohedral phase, while α-rhombohedral boron is solidified and crystallized from a variety of metallic solvents. Heating the

α-rhombohedral boron at ambient pressure to a temperature above 1200°C causes it to slowly transform to β-rhombohedral boron [94]. This means that β-rhombohedral boron is a stable phase at high temperature, while α-rhombohedral boron is a metastable phase under ambient conditions, even though it has a highly ordered structure [94].

Representative allotropes of solid elemental boron, α-rhombohedral boron (α-B_{12}), and β-rhombohedral boron (β-B_{105}), have unusual structures and are shown in Fig. 1-6. β-B_{105} boron has an exceptionally complex structure, with more than 300 atoms per hexagonal unit cell, which consists of B_{12} clusters (icosahedra), B_{28} clusters (three face-sharing icosahedra), a single atomic site connecting two B_{28} clusters, and a number of partially occupied interstitial sites, which can be involved in phase transitions from β- rhombohedral boron to other phases [95-99].

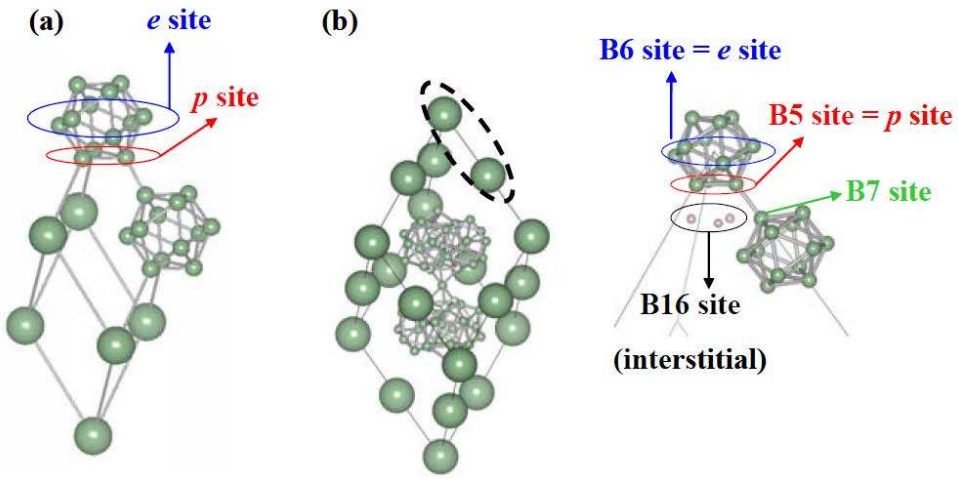

Figure 1-6. Structures of (a) α-B_{12} and (b) β-B_{105}. The largest balls represent the B_{12} icosahedra

1.5. Neutron Analysis

1.5.1. Current Issue in Fusion Reactor

1.5.1.1. Introduction of ITER (International Thermonuclear Experimental Reactor Project)

The International Thermonuclear Experimental Reactor Project (ITER) is a massive international collaborative project to verify the technological and scientific feasibility of using energy originating from the fusion reaction, which is similar to the principle of solar energy generation [100, 101]. Since the late 1980s, with the support of the International Atomic Energy Agency (IAEA), the Fusion Energy Research Project has been underway as a joint project between Korea, the United States, the European Union, Japan, Russia, China, and India, with a total project cost of

approximately €15-billion (US$21-billion) [102-104]. Participating countries share the technological results derived from the research and development, and own the relevant intellectual property rights.

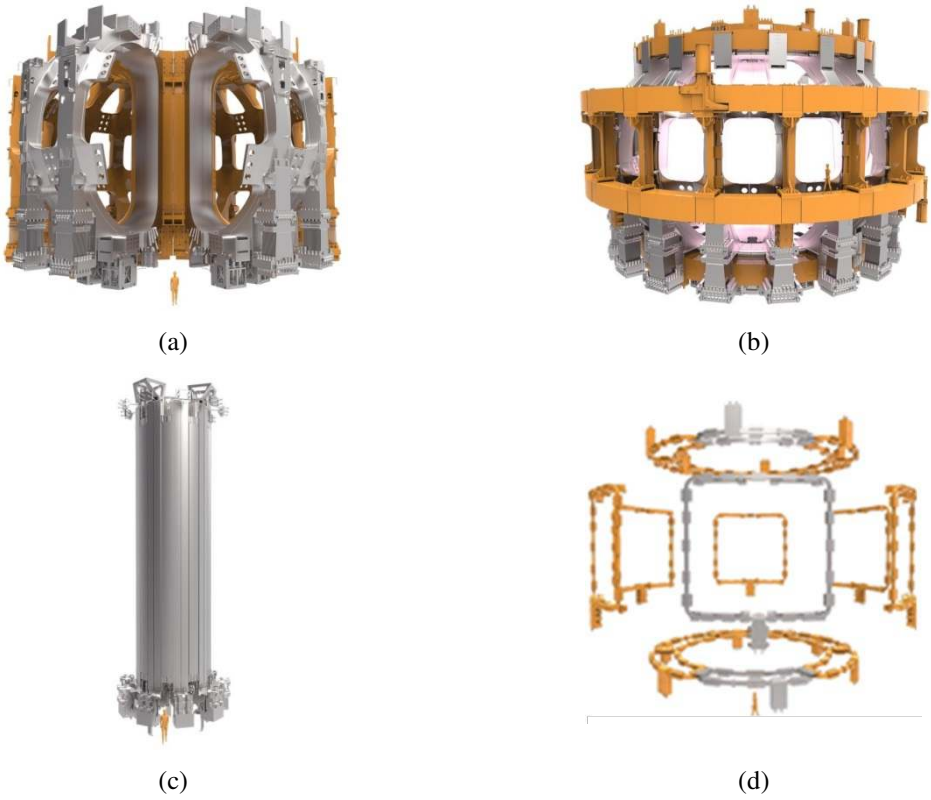

Figure 1-7. Schematic diagrams of the superconducting magnets in ITER: (a) Toroidal field (TF) coils; 18 D shaped toroidal field magnets are installed around the vacuum vessel; TF coils are designed to produce 41 gigajoules (GJ) and a maximum magnetic field of 11.8 tesla (T). (b) Poloidal field coil; Six ring-shaped poloidal field coils are placed outside of the toroidal field magnet structure to control the stability of the plasma. These are designed to produce a total magnetic energy of 4 gigajoules (GJ) and a maximum magnetic field of 6 tesla (T). (c) Central solenoid coil. (d) Correction coils; Eighteen superconducting coils are inserted between the toroidal and poloidal field coils for the correction of errors caused by geometrical deviations during the manufacturing and assembly processes [105].

The nuclear fusion experiment project, ITER, is being conducted internationally by participating scientists and engineers. In this project, they will demonstrate the process of generating energy from the fusion reaction between deuterium (D) and tritium (T) in a plasma using a nuclear fusion device called the Tokamak magnet [105, 106]. There are three conditions that should be satisfied to achieve a fusion reaction on the laboratory scale: an extremely high temperature (over 150 million K), sufficient plasma particle density, and adequate holding time for the plasma formation [107, 108]. Not only are these three essential conditions, but advanced devices are also needed to control the ultra-high-temperature plasma for the fusion reaction.

From the practical point of view, a tokamak device is considered the best instrument for controlling the plasma. (See Fig. 1-7.) The main idea of the design is to trap electrons and ions in a plasma along a magnetic force line and send them in opposite directions with spiral shaped paths. Provided that the magnetic field lines flow continuously in the device, the electrons and ions will continue to circulate in the device long enough. There are several magnetic systems to realise effective and stable plasma trapping. The primary magnetic system for plasma confinement is the toroidal field (TF) coils that are installed around the doughnut-shaped plasma chamber (vacuum vessel) and create the toroidal magnetic field [109, 110]. Since the magnetic field generated by this coil is unstable and discontinuous in the device and varies with distance, however, the electrons and ions are separated from each other and come out. To counteract this, a current, based on Faraday's law, will be flowing in the plasma in the tokamak device [111]. Thus, the solenoid is installed inside the doughnut to change the magnetic field and to make the current flow through the plasma [112]. In this manner, the electrons and ions do not escape to the outside and stay inside the device. Furthermore, poloidal field (PF) coils must be installed on the outside of the device so as to control the shape of the magnetic force lines and the position for the operation of the tokamak [113, 114].

1.5.1.2. The Critical Issue in Superconducting Cable and the Solution

The superconducting magnets in the ITER are exposed to detrimental circumstances during operation that can cause degradation of the superconducting cables. For ITER, this issue has been considered critical for the overall success of the project. As mentioned in the prior section, the ITER is the most expensive worldwide project, but this issue has threatened it.

In general, the stress in the superconducting magnets for the fusion reactor originates from several reasons: the fabrication conditions, winding tension, temperature variations, such as thermal contraction during cooldown to the critical temperature, and the magnetic field in itself [115]. For example, over the expected lifetime of the cables, they are intended to withstand 60,000 current/temperature cycles, and a specially designed facility and test programme, SULTAN [116], was developed to experimentally assess the performance of the cables and their possible degradation.

In addition, the cables (see Fig. 1-7 and Fig. 1-8) are exposed to 60,000 current pulses with a temperature of more than 150 million K when the fusion reactor is in operational mode, and it must withstand these harsh conditions without any trouble [118-120]. Thus, the superconducting cables are easily damaged during the manufacturing process and operation in the fusion reactor.

Recently, scientists and engineers have tried to the test the superconducting cables to scrutinize any significant damage and predict possible future damage. In this research, the neutron analysis technique was used to examine superconducting cables of the central solenoid coil in ITER [121]. After this research was finished, the participants insisted that this research will be continued until they get successful results in the cable tests [122].

Figure 1-8. Jacketed cable in ITER's toroidal field coil, consisting of superconducting and non-conducting strands around a central channel for helium [117].

The neutron analysis method has several merits, such as its high penetration, non-destructive character, speed, and low labour intensity compared with conventional destructive methods (hole drilling, X-ray diffraction with material removal). Not only that, this method is a direct (simple stress recalculation), non-contact method, so that it can be used to measure stress in special environments typical of those experienced in-service (high, low, or cryogenic temperatures, and phase sensitivity) [123]. Thus, the neutron analysis method is and will remain the most promising technique for the estimation of existing and possible future damage to the superconducting cables. The experience obtained in the neutron diffraction studies on the ITER Nb_3Sn-based superconducting cables and strands can be easily extended and extrapolated to the research on other superconducting strands and wires.
Not only that, the neutron analysis method has several merits because it is a high penetration, non-destructive, faster, and less labour intensive method than the conventional destructive methods (hole drilling, X-ray diffraction with material removal). As a direct (simple stress recalculation), non-contact method, it can be used to measure stress in special environments typical of those experienced in-service (high temperature), and where there is phase sensitivity [124]. Thus, the neutron analysis method is the most promising technique for the estimation of existing and possible future damage to the superconducting cable.

1.5.2. Neutron Diffraction

1.5.2.1. Introduction and History of the Neutron

The discovery of the neutron began in the 1920s and 1930s at a time when physicists were embracing an atomic model in which atomic nuclei were made up of protons and electrons. In 1920, Ernest Rutherford assumed that possibility that neutrons exist. Rutherford thought that the atomic number and atomic mass difference of an atom could be explained by neutrally charged particles located in the nucleus. He regarded neutrons as 'the simultaneous presence of electrons

and protons' [125]. At that time, physicists were embracing models in which atomic nuclei were made up of protons and electrons. Rutherford assumed that if all of the nuclei were made up only of protons then the atoms would have double the charge. This was considered as evidence for the presence of "nuclear electrons" which cancel out the charge of the proton. Nitrogen-14 was believed to be composed of 14 protons and 7 electrons, thus having a charge of +7 and an atomic weight of 14 (which turns out to be a wrong model in modern times) [126-129]. In quantum mechanics, it is said that light particles, such as electrons, cannot be located in the narrow space of an atomic nucleus with some energy. In 1930, the Soviet physicists Viktor Ambartsumian and Dmitri Ivanenko discovered that nuclei could not be made up of protons and electrons. Finally, they proved that there must be some neutral particles next to protons, even though that was contrary to common sense in those days [129, 130].

In 1931, Walter Botte and Herbert Becker made the following discoveries in Germany: When high-energy alpha (α) particles strike light materials, such as beryllium, boron, and lithium, this usually results in unusual sagittal radiation. At first, this radiation was considered to be gamma (γ) rays, but it was different from any other gamma (γ) rays, and experiments with the radiation as gamma (γ) rays could not correctly interpret the results of the experiment [131, 132]. In 1932, Irene Joliot Curie and her husband Frédéric Joliot Curie made essential contributions to this area in Paris. When radiation strikes paraffin or other hydrogen-containing compounds, protons with very high energies are emitted. In the same year, James Chadwick conducted a series of experiments demonstrating that the gamma (γ) ray assumption was wrong at Cambridge University. He found that this radiation had only a small amount of the charge and that the particles responsible had a mass about the same as that of the proton. This particle was called the neutron, and its name is the combination of neutral from Latin and the Greek suffix -on [133, 134].

A neutron is a nucleon slightly heavier than a proton, with no charge in the nucleus [133]. It consists of an upper quark and two lower quarks. Moreover, it is unstable in the free state and has a half-life of 614 seconds (10 minutes 14 seconds) [133]. It will be in a stable state, however, if it is trapped inside a nucleus. The neutron is labelled by N, the neutron number, as a subatomic hadron [133]. The neutron also has no charge, and the mass is a little bigger than that of the proton. The atomic nuclei of other atoms except for the protium isotope of hydrogen are composed of both protons and neutrons [133]. The number of protons forming the nucleus is called the atomic number, which determines the type of element. Neutrons can be tied to neutrons through nuclear forces to form atomic nuclei. If the neutrons are bound, the nuclei still have the same charge. The bound neutron is stable (depending on the nuclide), whereas free neutrons are unstable. Specifically, free neutrons experience beta decay, and the average life span is around 881.5 seconds [134]. Free neutrons are created in fission or fusion reactions. Neutron generators and research reactors are used as neutron sources for neutron generation, and fracture sources are used for irradiation and neutron scattering experiments. Even though free neutrons are not chemical elements, they are sometimes included in the nuclide table [135].

Apart from their applications in fundamental nuclear particle physics, neutron beams and neutron fluxes are used in such applications as neutron activation analysis, neutron tomography, neutron

diffraction, neutron small-angle scattering, neutron reflectometry, neutron spectroscopy, etc., to list a few. The focus of this work is neutron diffraction and, more specifically, neutron diffraction stress analysis and texture analysis.

1.5.2.2. Neutron Sources

Due to the specifics of neutron production and the properties of neutron radiation, which is highly penetrating and harmful to people, neutrons are notoriously difficult and expensive to produce. The facilities operating neutron sources must ensure radiation protection and safety procedures to prevent severe accidents during neutron production. Currently, two main types of neutron sources are widely accepted for producing thermal neutron beams: (1) nuclear fission (steady state) reactors and (2) neutron spallation (pulsed) sources. These are shown schematically in Fig. 1-9 [136] and Fig. 1-10, [137] respectively. The major neutron sources and neutron facilities are listed in Table 1-1. [138].

Neutron research reactors are very different from nuclear power reactors despite having the same fission reaction principle. Neutron research reactors have a much smaller amount of radioactive materials (kilograms vs. tons in the power reactors), much lower power (tens of MW vs. several GW), and are optimised for higher neutron flux rather than heat generation. The majority of current research reactors were built in the 1960s and 1970s for the purpose of materials testing for the nuclear industry. Fewer reactors were designed to produce neutron beams to be used for neutron scattering research. An exemplary research reactor of this type, optimized for neutron scattering research, is the High-Flux Reactor (HFR) at the Institute Laue-Langevin (ILL), built in 1972 in Grenoble, France [138]. Many other national-scale research reactors and facilities came into operation afterwards. Some of them are JRR-3 at the Japan Atomic Energy Agency (1990), HANARO at the Korea Atomic Energy Research Institute (1997), FRM-II in Munich, Germany (2004), the Open Pool Australian Lightweight (OPAL) reactor at the Australian Nuclear Science and Technology Organization (2007), and the China Advanced Research Reactor (CARR) in Beijing, China (2010) [138].

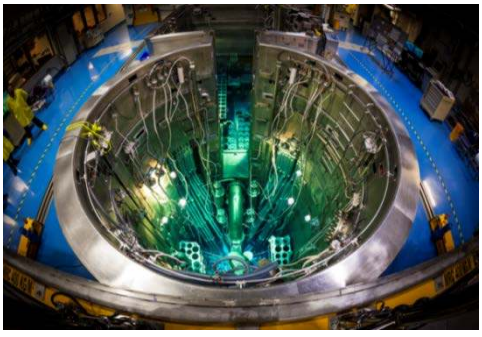

Figure 1-9. Photograph of ANSTO's Open Pool Australian Lightweight (OPAL) reactor [136].

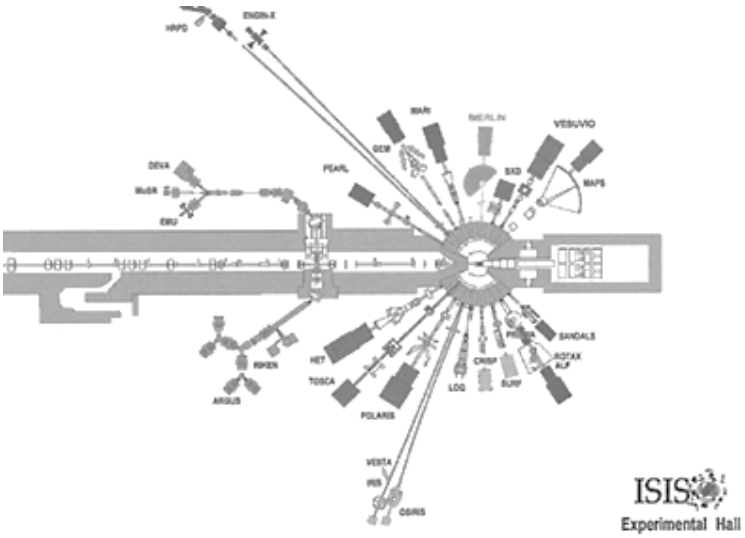

Figure 1-10. The ISIS facility (spallation source and instruments), located in Abingdon, UK [137].

Neutrons can also be produced by the spallation reaction (or so-called high-energy nuclear reaction).

Once a solid target nucleus is struck by a bombarding particle that has energy over 50 MeV, it emits and ejects many light particles such as neutrons, protons, or various composite particles. This principle is used in the pulsed proton-beam-driven neutron sources, the spallation sources, that have been recently completed or are under construction. The list of such sources/facilities includes the Spallation Neutron Source (SNS) in the United States, the Japanese Spallation Neutron Source (JSNS) of the Japan Proton Accelerator Research Complex (J-PARC) project in Japan (2008), and the China Spallation Neutron Source (CSNS) in China [139-141].

Table 1. Major thermal neutron beam sources [138].

Country	Source	Institution	Location	First operation	Power, MW	Thermal flux	Sci Instruments	Stress diffractometer
Australia	ANSTO	Lucas Heights	Lucas Heights	2007	20	4	13+	KOWARI
France	HFR	ILL	Grenoble	1972	60	12		SALSA
Germany	FRM-2	TUM	Munich	2004	20	7	25+	STRESS-SPEC
Japan	JRR-3	JAEA	Tokai	1962	20	2		RESA
Korea	HANARO	KAERI	Daejeon	1996	30	3		RSI
USA	HFIR	ORNL	Oak Ridge	1960	85	12	12+	HB-2B/NRSF2
USA	NBSR	NIST	Gaithersburg	1969	20	2	25+	BT8/RSD
China	CARR	CIAE	Beijing	2010	60	10	12+	RSD
China	CMRR	INPC	Mianyang	2000	20	2.4	8+	RSND
Japan	JSNS/J-PARC	KEK/JAEA	Tokai	2008			21	TAKUMI
Russia	IBR-2	JINR	Dubna	1984			13+	FSD
UK	ISIS	RAL	Abington	1985			21+11	ENGIN-X
USA	SNS	ORNL	Oak Ridge	2006			20+	BL-7/VULCAN
China	CSNS	IHEP, CAS	Dongguan	2017			3	project

1.5.2.3. Residual Stress Measurements

1.5.2.3.1. Definition

The residual stress is called the remnant stress in the elastic body when the force is removed from the outside. Residual stresses are generated when the plastic deformation over the entire cross-section of the deformed matrix is not uniform [142-145]. For instance, residual stresses mainly develop during manufacturing procedures, such as welding, hardening, casting, forging, and machining, and they remain in the final products as quantities of strain [146-149]. In the case where the matrix is in the equilibrium state, then the sum of all residual stresses is zero. On the other hand, compressive stress occurs in regions influenced by plastic deformation, and tensile stress appears in regions affected by elastic deformation when the cross-section of the matrix is in the equilibrium state [150, 151].

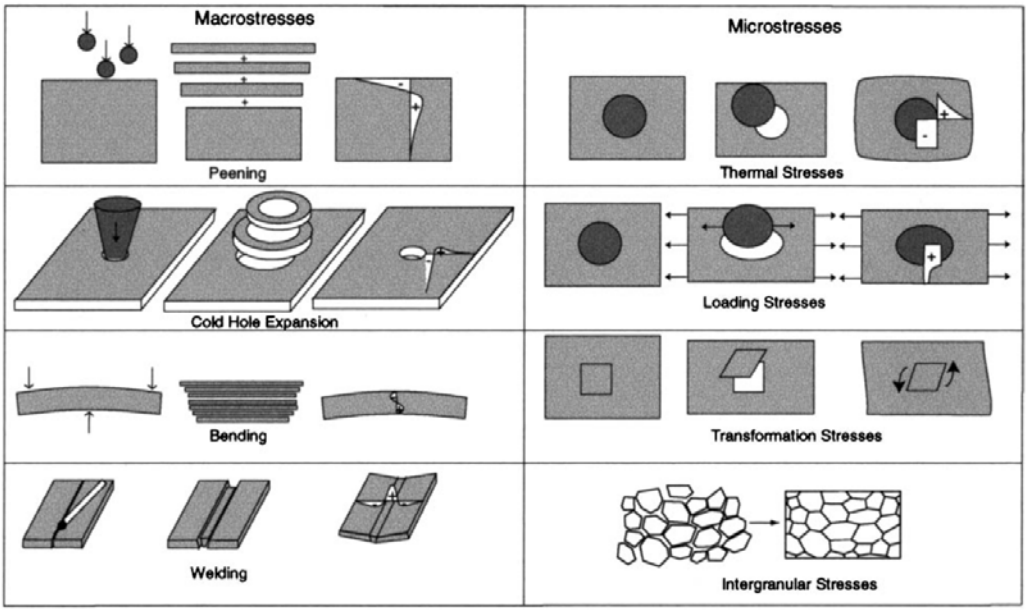

Figure 1-11. The types of residual stresses derived from misfits in the material. All illustrated stresses are classified by macrostress and microstress, including the processes indicated on the left, the misfits in the centre, and the resulting measurement stress patterns on the right [153].

Indeed, stress occurs not through differential thermomechanical treatment of the different parts, but through the differential thermomechanical impact on different phases, if the material is a composite. In this case, even though the product deformation is uniform over the cross-section, or the thermal load is uniform over volume, stress can be generated due to interaction of the matrix and reinforcements [152]. Thus, the residual stresses in the matrix are not convergent to zero. Admittedly, the origin of the residual stresses can also be explained by the shape misfit interactions between all components, which have different origins in the material, as shown in Fig.

1-11. [153].

For practical purpose, the residual stresses are classified into three types in accordance with the valid distance and length scale perspective, at which the stresses reach the equilibrium state [154]. The first type, type I, of residual stress, referred to as macroscopic residual stress, has an effective distance on the order of micrometres (μm) to centimetres (cm) across at least a plurality of crystal grains. The residual stresses generated by mechanical processing or heat treatment procedures are mostly considered macroscopic residual stresses. These stresses commonly appear in consequence of the macroscopic misfits due to changes in the structure or components in the matrix during manufacturing processes, and they are considered to be continuous stresses even over the microstructure. As shown in Fig. 1-12, there will be measurable diffraction peak shifts due to misfits between the length scale (L_0^I) and the total gauge volume (V_v) [153].

In terms of the measurement methods for these type I stresses, there are two groups of measurement methods. One group encompasses the destructive methods; they rely on measurements of the local deformations and distortions when some cuts in material are made or certain parts of material are removed.

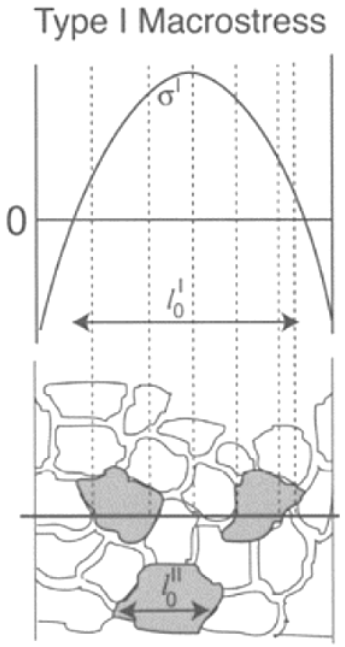

Figure 1-12. Example of Type I stress. The misfit has been introduced by quenching rapidly, and this is assumed to be a long-range misfit [155].

Such measurements are designed in such a way that, based on these deformation measurements, the original stress fields (or at least some stress components) can be reconstructed in the different parts before the destructive operations. Some of the destructive methods are hole and deep hole drilling methods, the material removal method, the slitting method, and the contour method [155]. The other group contains the non-destructive methods; usually they include X-ray diffraction

(XRD), neutron diffraction (ND), ultrasonic measurements, and magnetic measurements. Specifically in the diffraction methods, the presence of the macrostress is revealed through the measurable diffraction peak shift due to elastic effects [155].

The second type, type II, of residual stress, called structural microstress or intergranular stresses, is produced by the difference in mechanical properties of different phases (or, more generally, grain families) of the material. Microstresses are most prominent in composite materials where the Type II misfit can be caused by differences in elastic, plastic, or thermal properties of the two phases. For example, due to different thermal contraction of the matrix and reinforcement materials, average tensile stresses can be generated in the matrix, $< \sigma >_M^{II}$, and average compressive phase stresses will occur in the reinforcement, $< \sigma >_R^{II}$. Alternatively the microstress can also be generated through differences in plastic properties under plastic flow or differences in the elastic properties under the conditions of the applied load. This type of stress can also be generated in a single phase material under conditions of strong anisotropy of the material properties. The effective range of this stress variation is several micrometres (μm) which is the one-grain scale. Unlike Type I, the Type II stresses are discontinuous from grain to grain, as shown in Fig. 1-13. [155].

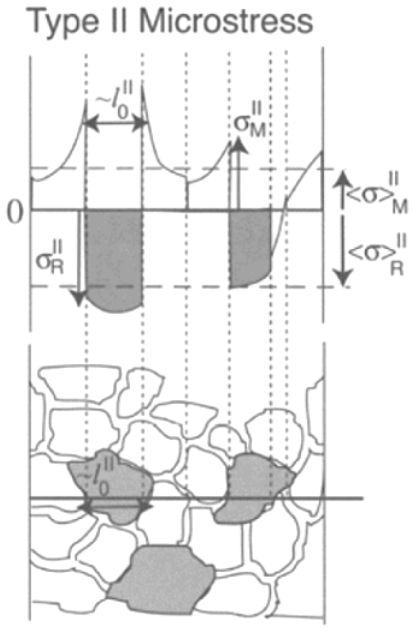

Figure 7. Example of Type II stress. The grain-to-grain and phase-to-phase misfits are shown schematically by separating the grains. M and R denote matrix and reinforcement, respectively [155].

In this case, the microstress can be derived from the combination of elastic mismatches between grains and (or) phases with macrostress. The microstress can also originate from differences in thermal expansion or plastic flow [155]. In general, there is no strict borderline between the first

and the second residual stress measurement methods. Type II stresses, however, have a discontinuous characteristic as opposed to the Type I and affect the local grains. In addition, they are not relevant to the grain boundary region [155].

Lastly, the residual stresses of type III refer to the atomic scale stresses, with effective range of 100 nm, as shown in Fig. 1-14. [155]. One example of manifestation of this stress type is work hardening, which is mainly due to interactions between the stress fields caused by each individual dislocation or by dislocation pile-ups [155].

Mechanical stress measurements cannot reach down to this atomic level, but in the diffraction methods, this stress can reveal itself through diffraction peak broadening effects.

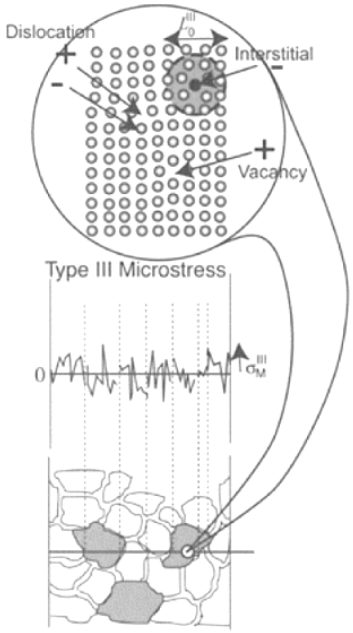

Figure 1-14. Type III stress varies on a length scale that is much shorter than the grain size. In this example, the misfits are introduced by dislocations, vacancies, and interstitials [153].

1.5.2.3.2. Measurement of Residual Stress

The principle of residual stress measurement by the neutron diffraction is analysis of the peak position shift of the Bragg peak. If crystal lattice strain is present in the area of material that is irradiated by a neutron beam, it causes a diffraction peak shift that can be measured very accurately, e.g. 100 microstrains and even better [56]. For the residual stress diffractometers based at fission reactors, the so-called angular dispersive technique is in use and is schematically shown in Fig. 1-15. [154] In this case, through use of a monochromator, the neutrons of a certain wavelength λ (more accurately a narrow band of wavelengths) are extracted from the polychromatic neutron flux, which is obtained from the reactor and delivered to the monochromator via neutron guides. The beam, formed by an incident slit (scale of mm) penetrates

into the material and scatters from the different lattice planes (*hkl*) of grains of the material to different angles With the use of the secondary slit in the front of a neutron detector, a specific spatial location (gauge volume) and particular lattice spacing can be selected. The peak position of the neutrons scattered from the gauge volume is measured as the angular peak position in the detector according to Bragg's law:

$$\lambda = 2d_{hkl}sin\left(\frac{2\theta}{2}\right) \quad (1)$$

Where λ is the monochromatic beam wavelength, d is the lattice spacing of the given (hkl) reflection and 2θ is the Bragg (scattering) angle [156, 157].

Instrumentally, two main components of the constant wavelength diffractometer are a monochromator and a detector. In modern designs, the monochromator (usually Si crystals) is optimised for maximising flux and overall accuracy of the measurements. In combination with a large position-sensitive neutron detector (PSD) designed to accurately and efficiently measure the distribution of the neutron flux, it is used to improve the overall measurement time.

The value measured by Bragg diffraction is not the stress, but the lattice spacing d_{hkl} measured in a certain direction which corresponds to specific reflecting (*hkl*) planes averaged over a gauge volume in the polycrystalline material [155].

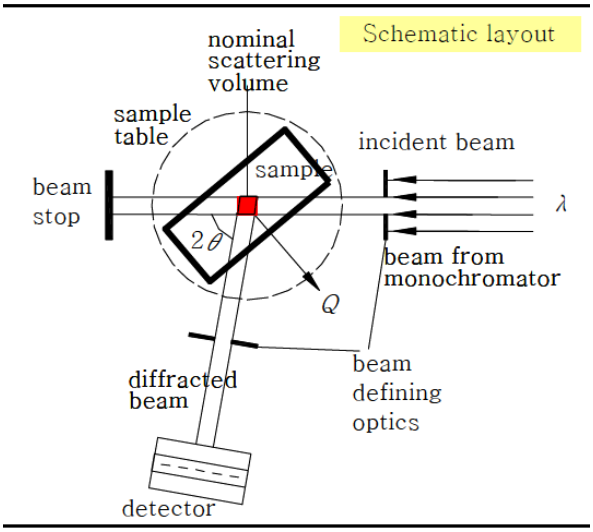

Figure 1-15. Schematic diagram of the neutron residual stress instrument [156].

In a stress-free material, the lattice strain, which is the relative change in the specific lattice spacing due to internal stress as compared to the deformation-free lattice plane value, is denoted by $d_{0,hkl}$. In a stressed specimen, a shift in each Bragg peak position occurs, and the elastic strains are then expressed by Eq. (1.4). [158].

$$\varepsilon_{hkl} = \frac{d_{hkl} - d_{0,hkl}}{d_{0,hkl}} = \frac{\Delta d_{hkl}}{d_{0,hkl}} = \frac{\sin\theta_{0,hkl}}{\sin\theta_{hkl}} - 1 \qquad (1.4)$$

In general, it is necessary to measure the strain in at least six different directions to determine the strain tensor (ε) at a given point of the specimen. It is well known, however, that knowing the principal axes makes it sufficient to measure only these directions. The relationship between deformation and the stress tensor is as follows in Eq. (1.5). [158].

$$\begin{bmatrix} \sigma_x & & \\ & \sigma_y & \\ & & \sigma_z \end{bmatrix} = \frac{E}{1+\nu} \begin{bmatrix} \varepsilon_x^D & & \\ & \varepsilon_y^D & \\ & & \varepsilon_z^D \end{bmatrix} + \frac{\nu E}{(1-2\nu)(1+\nu)} \left(\varepsilon_x^D + \varepsilon_y^D + \varepsilon_z^D\right) \qquad (1.5)$$

Where E is Young's modulus of the selected plane (*hkl*) diffraction and ν is the Poisson ratio. In order to obtain the normal stresses, the anisotropy of the constituent grains and the boundary conditions of the stress-strain in the grain boundaries must be taken into consideration, since it is an average strain measurement of the grains having a constant orientation in the polycrystalline specimen under uniaxial stress [158]. In general, researchers usually use three approximate models to solve this complex theoretical problem. The first theory is the Reuss approximation, which assumes constant stresses at the grain boundaries, the Voigt model, which approximates permanent deformation, is considered as a second assumption, and lastly, the more realistic Kröner approximation determines the average elastic modulus of the polycrystals, assuming that both stress and deformation are continuous in the grain boundary [159-163].

1.6. Outline of the Thesis

Chapter 1 provides a general overview and literature review to demonstrate the motivation of this thesis work. Also, experimental and theoretical studies are summarized to show the current status of our research field. Then, the analysis of the stress/strain behaviour in the boron-11 isotope based MgB_2 superconducting wire is summarized with respect to the neutron analysis method.

Chapter 2 includes more detailed information on experimental and neutron analysis techniques. The one principal technique used in this study is the neutron analysis method for investigation of the stress/strain behavior in the boron-11 isotope based MgB_2 superconducting wire. Additional techniques, such as accelerated X-ray diffraction, scanning electron microscopy (SEM), transmission electron microscopy (TEM), and X-ray photoelectron spectroscopy (XPS), are also introduced.

In Chapter 3, there is a basic analysis of three ^{11}B isotope rich powders by using specific analysis instruments. Accelerator mass spectrometry (AMS) and neutron transmission (NT) experiments were employed to trace the isotope composition of the ^{11}B powders. The crystallinity and morphology were determined by X-ray and electron diffraction. The chemical states of the boron isotope were investigated with near edge X-ray absorption fine structure spectroscopy (NEXAFS)

and X-ray photoemission spectroscopy (XPS). The properties of the MgB_2 products sintered from the boron powders are also characterised, in particular, their superconducting characteristics. The results of the study demonstrate the practical feasibility of the MgB_2-based superconducting products, with properties competitive with the traditional Nb-based superconductors for the fusion reactor application.

In Chapter 4, for practical application of the boron-11 isotope powder as a boron precursor, which was analysed in Chapter 3, appropriate high pressure was employed during the manufacturing process for the MgB_2 by the in-situ powder-in-tube (PIT) method. Indeed, special hot isostatic pressing (HIP) was performed for second stage densification. In this research on the effective densification of the MgB_2 superconductor, the combination of cold and hot densification methods will be a promising replacement for conventional methods for the inexpensive production of the MgB_2 and gives a guideline for using boron-11 isotope powder to synthesize $Mg^{11}B_2$ superconductor with an excellent critical current density (J_c).

In Chapter 5, the correlation between the critical current density, microstructure, and sintering temperature of the boron isotope based MgB_2 wires is studied, and all the required superconducting properties are reported. In this work, a batch of monofilament isotopic $Mg^{11}B_2$ wires with low-crystallinity ^{11}B powder as the boron precursor were fabricated using the powder-in-tube (PIT) process at different sintering temperatures, and the evolution of their microstructure and corresponding superconducting properties was systemically investigated. Indeed, the influence of both the superconducting fraction and the inter-grain connectivity on the J_c performance is discussed.

The superconductor magnet systems are the key components in a fusion energy system such as International Thermonuclear Experimental Reactor (ITER). Moreover, MgB_2 is much cheaper than NbTi superconductor, has lower induced radioactivation properties, and the boron-11 isotope based MgB_2 superconductor can replace NbTi, which has been used for poloidal and correction field coils in the ITER fusion reactor. Therefore, we fabricated boron-11 isotope MgB_2 and glycine doped $Mg^{11}B_2$ bulk superconductor in order to obtain enhanced J_c compared with the natural boron based MgB_2 in Chapter 6.

In Chapter 7, we used the neutron diffraction technique to measure the residual stress in boron-11 isotope based $Mg^{11}B_2$ superconducting wire, a promising candidate material to replace Nb-based superconductors in the next-generation fusion reactor, which is related to the work in Chapter 5. The residual stress state is given qualitative and quantitative interpretation in terms of micro- and macro-stress generation mechanisms, based on the isotropic model confirmed by the results on neutron texture measurements. The relationship between the stress/strain state in the wire and the transport critical current density is also discussed.

1.7. References

1. HeikoThomas, Adela Marian, Alexander Chervykov, Stefan Stückrad, Carlo Rubbia, Efficiency of superconducting transmission lines: An analysis with respect to the load factor and capacity rating, Electric Power Systems Research, 141, 381-391, 2016.

2. M. S. Dresselhaus & I. L. Thomas, Alternative energy technologies, Nature 414, 332–337, 2001.

3. T. Yamada, S. Yamamoto, T. Matsuda, M. Morita, M. Takechi, and Y. Shimada, Superconducting Magnets for Magnetic Resonance Imaging, Advances in Superconductivity, 55-58, Springer, 1989.

4. Matthias Klauda, Tobias Kässer, Bernd Mayer, Christian Neumann, Frank Schnell, Bachitor Aminov, Arno Baumfalk, Heinz Chaloupka, Member, IEEE, Serguei Kolesov, Helmut Piel, Norbert Klein, Stefan Schornstein, & Martin Bareiss, Superconductors and cryogenics for future communication systems, IEEE Trans. on Microwave theory and Tech., 48, 7, 2000.

5. J. Kortus, I. I. Mazin, K. D. Belashchenko, V. P. Antropov, and L. L. Boyer, Superconductivity of Metallic Boron in MgB_2, Phys. Rev. Lett. 86, 4656, 2001.

6. C. Terzioglu, A.Varilci, & I, Belenli, Investigation of effect of annealing temperature on mechanical properties of MgB_2, Journal of Alloys and Compounds, Volume 478, Issues 1–2, 10 June 2009, Pages 836-841.

7. Larbalestier, D., Gurevich, A., Feldmann, D. M. & Polyanskii, A. High-T_c superconducting materials for electric power applications. Nature 414, 368–377 (2001).

8. A Gurevich, S Patnaik, V Braccini, K H Kim, C Mielke, X Song, L D Cooley, S D Bu, D M Kim, J H Choi, L J Belenky, J Giencke, M K Lee, W Tian, X Q Pan, A Siri, E E Hellstrom, C B Eom and D C Larbalestier, Very high upper critical fields in MgB_2 produced by selective tuning of impurity scattering, Supercond. Sci. Technol. 17, 278–286 (2004).

9. A. Ballarino, R. Flükiger, Status of MgB_2 wire and cable applications in Europe, IOP Conf. Series: Journal of Physics: Conf. Series 871 (2017)

10. David A. Cardwell,David S. Ginley, Handbook of Superconducting Materials Vol. 1. CRC press, ISBN 9780750304320 - CAT# IP816, 2002.

11. Fang Cheng, Yongchang Liu, Zongqing Ma, M. Shahriar Al Hossain and M. Somerc, The isotope effect of boron on the carbon doping and critical current density of $Mg^{11}B_2$ superconductors, J. Mater. Chem. C, 5, 663-668, 2017.

12. J. D. Galambos, Y-K. M. Peng, R. L. Reid, M. S. Lubell, L. Dresner & J. R. Miller, Comparison of Nb_3Sn and NbTi Superconductor Magnet ITER Devices, , Fusion Technology, 15, 1046-1050, 1989.

13. T. Noda et al., J. Nuclear Materials 329–333 (2004) 1590–1593

14. https://en.wikipedia.org/wiki/Magnesium_diboride

15. Sonja I., Properties of MgB_2 superconductors with regard to space applications, Cryogenics, 46, 201-207, 2006.

16. Onnes, H. K. The resistance of pure mercury at helium temperatures, Comm. Phys. Lab. Univ. Leiden; No. 120b, 1911.

17. Onnes, H. K. Comm. Phys. Lab. Univ. Leiden. Suppl. 29, 1911.
18. https://www.nobelprize.org/nobel_prizes/physics/laureates/1913/onnes-bio.html
19. www.see.ed.ac.uk
20. Meissner, W. & Ochsenfeld, R. Naturwissenschaften 21 (44), 787-788, 1933.
21. http://en.wikipedia.org/wiki/Meissner_effect
22. http://hyperphysics.phy-astr.gsu.edu/hbase/Solids/meis.html
23. Brechna, H. Superconducting magnet systems. Springer, Germany, 1973.
24. London, F. & London, H. The electromagnetic equations of the supraconductor, Proc. R. Soc. Lond. A 149, 71-88, 1957.
25. Kittel, C., Introduction to Solid State Physics. John Wiley & Sons. pp. 273–278. ISBN 978-0-471-41526-8, 2004.
26. https://en.wikipedia.org/wiki/Coherence_length
27. Pippard, A. B. Proc. R. Soc. London Ser. A 216 (1127), 547-568, 1953.
28. https://en.wikipedia.org/wiki/Ginzburg%E2%80%93Landau_theory
29. Tinkham, M. Introduction to Superconductivity, Second Edition. New York, NY: McGraw-Hill. ISBN 0486435032, 1996
30. Abrikosov, A. A. Type II superconductors and the vortex lattice, Nobel Lecture, 2003.
31. Bardeen, J., Cooper, L. N. & Schrieffer, J. R. Phys. Rev. 106 (1), 162-164, 1957.
32. https://www.nobelprize.org/nobel_prizes/physics/laureates/1972/
33. Bardeen, J., Cooper, L. N. & Schrieffer, J. R. Phys. Rev. 108 (5), 1175-1204, 1957.
34. Buzea, C. & Yamashita, T. Review of the superconducting properties of MgB_2. Supercond. Sci. Technol. 14 115-46, 2001.
35. Pablo, D., Moraa, Miguel Castrob & Tavizón, G. Comparative study of the electronic structure of alkaline-earth borides (MeB_2; Me=Mg, Al, Zr, Nb, and Ta) and their normal-state conductivity, J. Solid State Chem. 169, 168-175, 2002.
36. R. Horst & H. Peter, 100 Years of Superconductivity, CRC Press, 2011.
37. Narlikar, A. V., Frontiers in Superconducting Materials, springer, ISBN 978-3-540-27294-6.
38. http://www.qm.phy.cam.ac.uk/
39. Nagamatsu, J. et al. Superconductivity at 39 K in m magnesium diboride, Nature 410, 63–64, 2001.
40. M. Mahdi Davari Esfahani, et al. Novel magnesium borides and their superconductivity, Phys. Chem. Phys. Chem., 19, 14486-14494, 2017.
41. Flukiger Rene, MgB_2 Superconducting Wires: Basics And Applications, World Scientific, ISBN: 978-981-4725-58-3, 2016.
42. Ravindran, P., Vajeeston, P., Vidya, R., Kjekshus, A. & Fjellvåg, H. Detailed electronic structure studies on superconducting MgB_2 and related compounds, Phys. Rev. B 64 224509, 2001.
43. Jin, S., Mavoori, H., Bower, C. & Dover, R. B. High critical currents in iron-clad superconducting MgB_2 wires, Nature 411 563-5, 2001.
44. Patel, H. Md Shahriar Al, S. Khay Wai, W. Qiu, H. Kobayashi, M. Zongqing, K. Seong Jun, J. Hong, P. Jin Yong, S. Choi, M. Maeda, M. Shahabuddin, M. Rindfleisch, M. Tomsic, S. X. Dou &

J. H. Kim, Supercond. Sci. Technol. 29 (4), 4LT02-09, 2016.

45. de Lima, O., Ribeiro, R., Avila, M., Cardoso, C. & Coelho, A. Phys. Rev. Lett. 86 (26), 5974-5977, 2001.

46. Scanlan, R. M., Malozemoff, A. P. & Larbalestier, D. C. Proc. IEEE 92 (10), 1639-1654, 2004.

47. Braccini, V., Nardelli, D., Penco, R. & Grasso, G. Physica C: Supercond. 456 (1-2), 209-217, 2007.

48. Mijatovic, D., Brinkman, A., Veldhuis, D., Hilgenkamp, H., Rogalla, H., Rijnders, G., Blank, D. H. A., Pogrebnyakov, A. V., Redwing, J. M., Xu, S. Y., Li, Q. & Xi, X. X. Appl. Phys. Lett. 87 (19), 192505, 2005.

49. Jin, S., Mavoori, H., Bower, C. & van Dover, R. B. Nature 411 (6837), 563-565, 2001.

50. Kumakura, H., Matsumoto, A., Nakane, T. & Kitaguchi, H. Physica C: Supercond. 456 (1-2), 196-202, 2007.

51. Giunchi, G., Ceresara, S., Ripamonti, G., Di Zenobio, A., Rossi, S., Chiarelli, S., Spadoni, M., Wesche, R. & Bruzzone, P. L. Supercond. Sci. Technol. 16 (2), 285-291, 2003.

37. Giunchi, G., Ripamonti, G., Perini, E., Cavallin, T. & Bassani, E. IEEE Trans. Appl. Supercond. 17 (2), 2761-2765 2007.

52 Li, G. Z., Yang, Y., Susner, M. A., Sumption, M. D. & Collings, E. W. Supercond. Sci. Technol. 25 (2), 025001, 2012.

53. Kumakura, H., Hur, J., Togano, K., Matsumoto, A., Wada, H. & Kimura, K. IEEE Trans. Appl. Supercond. 21 (3), 2643-2648,2011.

54. Radtsig, A. A., and Smirnov, B. M. 1986, Parameters of Atoms and Atomic Ions (Reference Book), Energoatomizdat, Moscow

55. Karl Heinrich Lieser, Nuclear and Radiochemistry: Fundamentals and Applications, John Wiley & Sons, 2008.

56. K. Shibata, T. Kawano, T. Nakagawa, et al., Japanese evaluated nuclear data library version 3 revision-3: JENDL-3.3, J. Nucl. Sci. Technol. 39 (2002), pp. 1125– 1136.

57. D. E. Mahagin and R.E. Dahl, Boron and Refractory Boride, Springer-Verlag, Berlin, 1977.

58. Sears, V. F. 1992, Neut. News, 3, 26.

59. E. P. Mooring , J. E. Monahan & C. M. Huddleston , Neutron Cross Sections of The Boron Isotopes For Energies Between 10 and 500 keV, Nuclear Physics 82, 16-32, 1966.

60. Viola, V. E. 1991, AIP Conf. Proc., 231, 1.

61. Keim, C. P. 1953, J. Appl. Phys., 24, 1255.

62. Sevryugova, N. N., Uvarov, O. V., and Zhavoronkov, N. M. 1960, At. Ener., 9, 110.

63. R. Velusamy, Mayer-Jensen shell model and magic numbers, Resonance, 12, 12–24, 2007.

64. K Heyde, The Nuclear Shell Model, Springer, Bristol, 1991.

65. Nuclear Shell Model (http://www.halexandria.org/dward472.htm)

66. Brightsen, R.A. Nucleon cluster structures in beta-stable nuclides. Infinite Energy, 1995, v.1, no. 4, 55.

67. Abzianidze, T., Karumidze, G., Kekelidze, L., Tabatadze, E., Shengelia, L., Bokuchava, G., and Shirikov, B., Proc. 16th Int. Conf. Phys. Rad. Phen. & Rad. Mat. Sci., 88, 2004.

68. Bokuchava, G., Karumidze, G., and Shirokov, B., Georg. Int. J. Sci., Technol. & Med., 1, 21, 2008.

69. Eisterer, M. et al. Neutron irradiation of MgB_2 bulk superconductors. Supercond. Sci. Technol. 15, L9-L12, 2002.

70. Wilke, R. H. T., Bud'ko, S. L. & Canfield, P. C. Systematic study of the superconducting and normal-state properties of neutron-irradiated MgB_2. Phys. Rev. B 73, 134512, 2006.

71. Putti, M. et al. Neutron irradiation of $Mg^{11}B_2$: From the enhancement to the suppression of superconducting properties. Appl. Phys. Lett. 86, 112503, 2005.

72. Mooring, F.P., Monahan, J. E. & Huddleston, C. M. Neutron cross sections of the boron isotopes for energies between 10 and 500 keV. Nucl. Phys. 82, 16–32, 1966.

73. Cheng, F. et al. Improved Superconducting properties in the $Mg^{11}B_2$ low activation superconductor prepared by low-temperature sintering. Sci. Rep. 6, 25498, 2016.

74. Hinks, D.G. & Jorgensen, J. D. The isotope effect and phonons in MgB_2. Physica C 385, 98–104, 2003.

75. Hishinuma, Y. et al. Microstructure and Superconducting Properties of Cu Addition MgB_2 Multifilamentary Wires Using Boron Isotope Powder as the Boron Source Material. Phys. Proc. 36, 1486–1491, 2012.

76. Tarantini, C. et al. Effects of neutron irradiation on polycrystalline $Mg^{11}B_2$. Phys. Rev. B 73, 134518, 2006.

77. Periodic table, http://www.rsc.org/periodic-table/element/5/boron

78. Acarkan, N. 2002, Proc. 1st Int. Boron Symp., K. Erarslan (Ed.), DU, Kütahya, 1.

79. Çelen, M. E., and Özmen, L. 2008, Abs. 16th Int. Symp. Boron, Borides & Rel. Mat., KM, Matsue, 36.

80. Oganov, A. R.; Chen, J. H.; Gatti, C.; Ma, Y. Z.; Ma, Y. M.; Glass, C. W.; Liu, Z. X.; Yu, T.; Kurakevych, O. O.; Solozhenko, V. L. Nature, 457, 863, 2009.

81. Horn, F. H. J. Appl. Phys., 30, 1612, 1959.

82. Tavadze, F. N., Bairamashvili, I. A., Tsagareishvili, G. V., Tsomaya, K. P., Zoidze, N. A. Sov. Phys. Crystallogr. 9, 768, 1965.

83. Shirai, K., Dekura, H., Mori, Y., Fujii, Y., Hyodo, H., Kimura, K. J. Phys. Soc. Jpn., 80, 084601, 2011.

84. Shirai, K. Dekura, H., Yanase, A. J. Phys. Soc. Jpn., 78, 084714, 2009.

85. Ma, Y. M.; Tse, J. S.; Klug, D. D., Ahuja, R. Phys. Rev., B, 70, 214107, 2004.

86. Bardeen, J.; Cooper, L. N.; Schrieffer, J. R. Phys. Rev., 108, 1175, 1957

87. Ashcroft, N. W. Phys. Rev. Lett., 21, 1748, 1968.

88. Papaconstantopoulos, D. A.; Boyer, L. L.; Klein, B. M.; Williams, A. R.; Morruzzi, V. L.; Janak, J. F. Phys. Rev. B, 15, 4221, 1977.

89. Longuet-Higgins, H. C.; Roberts, M. D. Proc. R. Soc. London Ser. A 1955, 230, 110.

90. Everhardt, W. H.; Crawford, B., Jr; Lipscomb, W. N. J. Chem. Phys., 22, 989, 1954.

91. Oganov, A. R.; Chen, J. H.; Gatti, C.; Ma, Y. Z.; Ma, Y. M.; Glass, C. W.; Liu, Z. X.; Yu, T.; Kurakevych, O. O.; Solozhenko, V. L. Nature, 457, 863, 2009.

92. Zarechnaya, E. Y.; Dubrovinsky, L.; Dubrovinskaia, N.; Filinchuk, Y.; Chernyshov, D.; Dmitriev, V.; Miyajima, N.; El Goresy, A.; Braun, H. F.; Van Smaalen, S.; Kantor, I.; Kantor, A.; Prakapenka, V.; Hanfland, M.; Mikhaylushkin, A. S.; Abrikosov, I. A.; Simak, S. I. Phys. Rev. Lett., 102, 185501, 2009.

93. Parakhonskiy, G.; Dubrovinskaia, N.; Bykova, E.; Wirth, R.; Dubrovinsky, L. Sci. Rep., 1, 96, 2011.

94. Oganov, A. R.;Solozhenko, V. L.; Gatti, C.; Kurakevych, O. O.; Le Godec, Y. J. Superhard Mater., 33, 363, 2011.

95.Tadashi Ogitsu, Eric Schwegler, and Giulia Galli, β-Rhombohedral Boron: At the Crossroads of the Chemistry of Boron and the Physics of Frustration, Chem. Rev. 113, 3425−3449, 2013.

96. Donohue, J. In The Structures of the Elements; John Wiley & Sons: New York, 1974.

97. Young, D. A. Phase Diagrams of the Elements; University of California Press: Berkeley, 1991.

98. Chase, M. Chemical Reviews Review 3445 dx.doi.org/10.1021/cr300356t | Chem. Rev. 2013, 113, 3425−3449 W. J. Phys. Chem. Ref. Data 1998.

99. Douglas, B. Structure and Chemistry of Crystalline Solid; Springer Science + Business Media, Inc.: Berlin, 2006.

100. Baker, C.C. & Stewart, P.A., International Thermonuclear Experimental Reactor, Energy Conversion Eng. Conf. 1996. IECEC 96. Proceed. vol. 2, 820-823, 1996.

101. Sedor, J., International Partnerships in Large Science Projects, DIANE Publishing, 1998

102. Clery, D., ITER fusion project to take at least 6 years longer than planned, Sci. Mag. Nov. 19, 2015.

103. Fountain, H., A Dream of Clean Energy at a Very High Price, The New York Times, MARCH 27, 2017.

104. https://www.iter.org/proj/inafewlines#5

105. https://www.iter.org/proj/inafewlines#3

106. Woods, L. C., Theory of Tokamak Transport, Wiley-VCH, 2006.

107. Freidberg, J. P., Plasma Physics and Fusion Energy, Cambridge University Press, 2008.

108. Gill, R. D., Plasma Physics and Nuclear Fusion Research, Academic Press, 2013.

109. Mitchell, N., et al., The ITER Magnet System, IEEE Trans. App. Supercond., 18, 2, 2008.

110. Sborchia, C., et al., Design and Specifications of the ITER TF Coils, IEEE Trans. App. Supercond, 18, 2, 2008.

111. Ambrosino, G & Albanese, R., Magnetic control of plasma current, position, and shape in Tokamaks: a survey or modeling and control approaches, IEEE Control Systems, 25, 5, 2005.

112. https://www.iter.org/mach/magnets

113. Mitchell, N., et al., The ITER Magnets: Design and Construction status, IEEE/CSC & ESAS European Superconductivity NEWS Forum, No. 19, January 2012.

114. Lim, B., et al., Design of the ITER PF Coils, IEEE Trans. App. Supercond., 21, 3, 2011.

16. Arp, V., Stresses in superconducting solenoids, J. App. Phys., 48, 2026, 1977.

115. D. Bessette, Design of a Nb_3Sn Cable-in-Conduit Conductor to Withstand the 60 000 Electromagnetic Cycles of the ITER Central Solenoid, IEEE Trans. App. Supercond., 24, 2, 2014.

116. http://www.ansto.gov.au/AboutANSTO/MediaCentre/News/ACS125707

117. Rolando, G., Devred, A & Nijhuis, A., Temperature and current margin of ITER central solenoid conductor designs during a 15 MA plasma scenario, Supercond. Sci. Technol., 27, 025010, 2014.

118. A. C. C. Sips, for the Steady State Operation, and the Transport Physics topical groups of the International Tokamak Physics Activity, Advanced scenarios for ITER operation, Plasma Phys. Control. Fusion, 47, A19–A40, 2005.

119. https://www.iter.org/mach

120. https://www.iter.org/newsline/159/554

121. Brumfiel, G., Cable test raises fears at fusion project, Nature 471, 150, 2011.

122. Tomone, S., Hemmi, T., Suwa, T., Takahashi, Y., Koizumi, N., Luzin, V., Suzuki, H and Harjo, S. Evaluation of thermal strain induced in components of Nb_3Sn strand during cooling, IEEE Trans. App. Supercond., 28, 3, 2018.

123. Hutchings, M. T., Withers, P. J., Holden, T. M. & Lorentzen, T., Introduction to the Characterization of Residual Stress by Neutron Diffraction, Taylor & Francis, 2005.

124. Rutherford, E., Bakerian Lecture: Nuclear constitution of atoms, Proc. R. Soc. Lond. A 1920 97, 374-400

125. Friedlander, G., Kennedy, J. W. & Miller, J. M., Nuclear and Radiochemistry (2nd edition), Wiley, 1964.

126. Stuewer, R. H., The Nuclear Electron Hypothesis, Otto Hahn and the Rise of Nuclear Physics 19-67.

127. Brown, L. M., The idea of the neutrino, Physics Today 31, 9, 23 (1978)

128. Fernandez, B. & Ripka, G., Unravelling the Mystery of the Atomic Nucleus: A Sixty Year Journey 1896 — 1956, Springer Science & Business Media, 2012.

129. Bothe, W. & Becker, H. Z. Physik (1930) 66: 289. https://doi.org/10.1007/BF01390908

130. Becker, H. & Bothe, W. Z. Physik (1932) 76: 421. https://doi.org/10.1007/BF01336726

131. J. Chadwick, F. R. S., Bakerian lecture.—The neutron, Proc. R. Soc. Lond. A 1933 142, 1-25.

132. J. Chadwick, Possible Existence of a Neutron, Nature, 129, P 312, 1932.

133. Thomas, A. W. & Weise, W., The Structure of the Nucleon, Wiley-WCH, Berlin, 2001.

134. Nakamura, K. "Review of Particle Physics". Journal of Physics G: Nuclear and Particle Physics 37 (7A): 075021. 2010.

135. Zhiliang Cao, Henry Gu Cao. Unified Field Theory and the Configuration of Particles. International Journal of Physics., 1(6),151-161, 2013.

136. http://www.ansto.gov.au/ResearchHub/OurInfrastructure/ACNS/Facilities/OPALReactor

137. R. Eccleston and C.C. Wilson, A guided tour of ISIS: 2004 update, Neutron News, 15, 15–18, 2004.

138. Anderson, Ian S., McGreevy, Robert L., Bilheux, Hassina Z, Neutron Imaging and Applications: A Reference for the Imaging Community (Neutron Scattering Applications and Techniques), Springer; 2009.

139. M.N.H. Comsan, Spallation Neutron Sources For Science and Technology, Proceedings of

the 8th Conference on Nuclear and Particle Physics, 20-24, 2011.
140. Alan Chodos, Spallation Neutron Source Features Superconducting Linac, APS NEWS, 9, No. 5, 2000.
141. Weiren Chous, Spallation neutron source and other high intensity froton sources, FERMILAB-Conf-03/012, 2003.
142. T Lorentzen, Characterization of residual stresses generated during inhomogeneous plastic deformation, J. Strain Analysis, 33, 243, 1988.
143. T. Nakamura and S. Suresh, Effects of thermal residual stresses and fiber packing on deformation of metal-matrix composites, Acta metall, mater. 41, 1665-1681, 1993.
144. S. F. Corbin and D. S. Wilkinson, Low strain plasticity in a particulate metal matrix composite, Acta metall, mater. 42, 1319-1327, 1994.
145. S. Ho A. Saigal, Thermal residual stresses and mechanical behavior of cast SiC/Al composite, Materials Science and Engineering, A183, 39-47, 1994.
146. Helmut Wohlfahrt, Residual stresses as a consequence of welding, Residual Stresses (Technology, Applications, Effects), Elsevier, 39–58, 1987.
147. Berthold Scholtes, Residual stresses introduced by machining, Residual Stresses (Technology, Applications, Effects), Elsevier, 59–71, 1987.
148. H.O. Fuchs and J.J. Daly, Residual stresses production of self-stresses, Residual Stresses (Technology, Applications, Effects), Elsevier, 73–86, 1987.
148. T. Ericsson, Residual stresses caused by thermal and thermomechanical surface treatments, Residual Stresses (Technology, Applications, Effects), Elsevier, 87–113, 1987.
149. P. J. Withers and H. K. D. H. Bhadeshia, Residual stress. Part 2 – Nature and origins, J. Materials Science and Technology, 17, 366, 2001.
150. Eckard Macherauch, Residual Stresses (Technology, Applications, Effects), Elsevier, 1-36, 1987.
151. T.W. Clyne, P.J. Withers, An Introduction to Metal Matrix Composites, Cambridge University Press, 1995.
152. P. J. Withers and H. K. D. H. Bhadeshia, Residual stress. Part 1 – Measurement techniques, J. Materials Science and Technology, 17, 355, 2001.
153. P. J. Withers, M. Preuss, A. Steuwer and J. W. L. Pang, Methods for obtaining the strain-free lattice parameter when using diffraction to determine residual stress, J. Appl. Cryst. 40, 891-904, 2007.
154. Hutchings, M. T., Withers, P. J., Holden, T. M. & Lorentzen, T. Introduction to the Characterization of Residual Stress by Neutron Diffraction, 1-272 (Taylor & Francis, 2005).
155. Wanchuck Woo, Dong-Kyu Kim & Gyu-Baek An, Residual stress measurements using neutron diffraction, Journal of Welding and Joining, 33, 30-34, 2015.
156. Kittel, C. Introduction to Solid State Physics, New York: John Wiley & Sons, 1976.
157. B. D. Cullity, S. R. Stock & Prentice Hall, Elements of x-ray diffraction, Prentice Hall, 2001.
158. A. J. Allen, M. T. Hutchings & C. G. Windsor, Neutron diffraction methods for the study of residual stress fields, Advances in Physics, 34, 445-473, 1985.

159. D. H. Chung & W. R. Buessem, The VoigtReussHill Approximation and Elastic Moduli of Polycrystalline MgO, CaF_2, βZnS, ZnSe, and CdTe, J. Appl. Phys. 38, 2535, 1967.
160. W. Voigt, Lehrbuch der Kristallphysik (Teubner, Leipzig, 1928).
161. A. Reuss, Z. Angew. Math. Mech. 9, 49, 1929.
162. R. Hill, Proc. Phys. Soc. London A 65, 349, 1952.
163. E. Kröner, J. Mech. Phys. Solids 15, 319, 1967.

Chapter 2

Experimental Procedures and Instruments

2.1. Boron-11 Isotope based MgB_2 Superconductor Preparation

In this thesis work, boron-11 isotope based Monofilament MgB_2 wire was fabricated by the conventional powder-in-tube (PIT) technique using the in-situ method [1]. In this process, a Nb barrier and Monel sheath consisting of of Nb tube inside and Monel (Ni-Cu alloy) tube outside were used, and low crystalline boron-11 isotope powder (from Pavezyum Kimya, Turkey, Moissan method [2], 840 nm, 95.5%) and magnesium powder (100-200 mesh, 99%) were used for forming boron-11 isotope based MgB_2 phase with the stoichiometric composition of Mg: B = 1: 2 [3, 4]. More explanation and analysis of the three types of boron-11 isotope powders are presented in Chapter 3.

2.2. Residual Stress and Texture Measurement using Neutron Diffraction

For neutron experiments, the individual $Mg^{11}B_2$ wires were cut into pieces ~5 mm long and bunched together to form bulk samples with approximate dimensions of 4×4×4 mm^3. The measurements of residual stress on $Mg^{11}B_2$ wires were carried out using the KOWARI neutron diffractometer (shown in Figure 2-1) [5] at the Open Pool Australian Lightwater (OPAL) research reactor at the Australian Nuclear Science and Technology Organization (ANSTO).

Figure 2-1. KOWARI neutron diffractometer in a general stress setup and texture setup.

The $Mg^{11}B_2$ phase was measured at 90° geometry using wavelength λ = 1.5 Å and Bragg angle (2θ) = 102° for the $Mg^{11}B_2$ (211) reflection. Two principal directions, transverse and axial, were measured. A pure $Mg^{11}B_2$ pellet sample was used to determine the unstressed lattice spacing, d_0. The stress (σ) was calculated for the measured transverse and axial strains of the $Mg^{11}B_2$ (211)

reflection using the (*hkl*)-dependent Young's modulus (E) and Poisson's ratio (ν) calculated from the single crystal elastic constants, $E(211)$ = 316.2 GPa, and $\nu(211)$ = 0.17 according to the following relationship [6, 7].

$$\sigma_{a,t} = \frac{E}{1+\nu}\left\{\varepsilon_{a,t} + \frac{\nu}{1-2\nu}(\varepsilon_a + 2\varepsilon_t)\right\} \quad (1)$$

To further study aspects of anisotropic stress state, neutron texture measurements were performed on the wires, including on the three phases, $Mg^{11}B_2$ and Monel-Nb sheath (only for the sample sintered at 700°C, since the other samples were essentially identical). A few representative pole figures were collected to judge the crystallographic isotropy/anisotropy using the same KOWARI diffractometer.

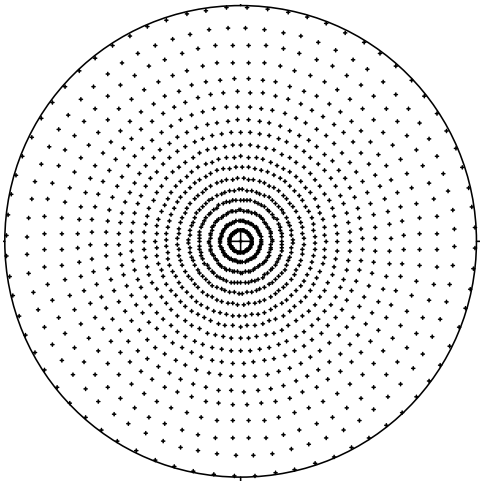

Figure 2-2. Example of the pole figure measurement mesh used in texture measurements.

The texture measurements of the wires were carried out on the same KOWARI neutron diffractometer (ANSTO) using the measurement mesh shown in Figure 2-2. Three phases, $Mg^{11}B_2$, Nb, and Monel, were measured using wavelength λ = 1.67 Å, 5°×5° mesh (see Figure 2-2), and several pole figures for every phase, which were sufficient to judge the preferred orientation of each phase. In particular, (100) and (110) pole figures were measured for $Mg^{11}B_2$, (110) and (200) planes for Nb, and (111) and (200) planes for Monel. Some of the pole figures were measured simultaneously due to diffraction pattern overlap.

2.3. X-ray Diffraction

The X-ray diffraction technique used for the identifying and classifying each phase, such as Mg, MgO, boron rich MgB_2, and MgB_2 in the boron-11 isotope based MgB_2 superconductor, including grain size, unit cell dimensions, volume fraction, etc. In this thesis work, two different types of X-

ray diffraction techniques were used. The MgB_2 phase formation and fundamental crystallographic information on the wire was investigated using a conventional X-ray diffractometer. The XRD device (Mini-materials Analyser, GBC Scientific Equipment, USA) was used with Cu Kα (λ = 1.54056 Å) radiation for the XRD analysis [8]. The XRD data for the samples were collected from angles of 20° to 80°, using a 1° per min scan rate and 0.02° step size. And high resolution (HR)-XRD (ATX-G) was used for analysis of the impurities in the boron 11 isotope powders.

2.4. Electron Microscopy

Scanning electron microscopy (SEM) and transmission electron microscopy (TEM) were used in this thesis work [9, 10]. SEM is a fundamental analytical method for the evaluating morphological characteristics of materials, such as porosity, contrast differences, particle size, etc. An energy dispersive spectrometer (EDS or EDAX) is attached to an electron microscope. The high energy electron beam reacts with the specimen, making it possible to determine the structure and chemical composition of the specimen. The components of the specimen can be identified using characteristic X-rays. The X-ray spectrum is a graph in which the intensity (Y-axis) of the X-ray is an energy function (X-axis). The channel number of the energy is the maximum value of the peak, which is the energy of the X-ray. The computer of the EDS system stores the location of all the characteristic X-rays, and the K, L, and M X-rays appear on the screen when the peak position of the spectrum is within about 10 eV. It is very easy to find out the element from the peak. When the positions of the X-rays are nearer than the resolution (128 eV), the peaks are superimposed. If there is no possibility of overlapping by adjusting the acceleration voltage of the microscope, review the other X-ray. This allows accurate qualitative analysis [11]. Electron energy loss spectroscopy (EELS) in the part of the TEM can be used to determine the energy loss of inelastic scattering electrons that occur when accelerated electrons react with sufficiently thin specimens to obtain the desired information such as the element, composition, and chemical bonding state of the reactive site [12]. By combining SEM with TEM techniques, we can investigate how the doping element works in the MgB_2 phase during the wire production procedure, and details are presented in Chapter 4.

2.5. Superconducting Properties

The electromagnetic properties of the boron 11 based MgB_2 wires such as the critical temperature (T_c) and critical transport current (I_c) were measured using an American Magnetics re-condensing 15 T Superconducting (AMS) magnet [13]. The critical current density J_c was calculated by dividing I_c by the cross-section of the boron 11 based MgB_2 core. For the measurement of T_c, current up to 1 A was passed through the specimen at around 50 K temperature, and the voltages across the specimen were acquired by a Keithley Nanovoltmeter model 2182A via the LabVIEW program until the superconducting transition occurred [14]. The measured voltages were converted into resistance using Ohm's law.

2.6. Other Characterization Techniques

The particle size distributions of the three sorts of ^{11}B powders were measured by a Mastersizer S (Malvern Panalytical, UK). The isotope ratio of ^{10}B to ^{11}B was judged using a HVEE 846 Cs sputtering negative ion source and injector magnet of the Australian National Tandem for Applied Research (ANTARES) at ANSTO. Near edge X-ray absorption fine structure (NEXAFS) measurements at the 10D X-ray Absorption Spectroscopy (XAS) facility at the Pohang Accelerator Laboratory (PAL) and X-ray photoelectron spectroscopy (XPS, PHI 5000 Versa Probe, ULVAC PHI) were introduced for the purpose of the analysing the chemical state of the ^{11}B.

2.7. References

1. Patel D, Hossain M S A, See K W, Xu X, Barua S, Ma Z, Choi S, Tomsic M and Kim J H, MgB_2 superconducting joints for persistent current operation Supercond. Sci. Technol. 28 065017, 2015.

2. Markovskii, L. Y. Chemistry of magnesiothermal preparation of boron. Electron. Technol. 3, 95–102, 1970.

3. www.pavezyum.com.tr

4. www.copaltite.com

5. Kirstein, O., Luzin, V. & Garbe, U. The Strain-Scanning Diffractometer Kowari, Neutron News 20 (4), 34-36, 2009.

6. Kröner, E. Elastic moduli of perfectly disordered composite materials. J. Mech. Phys. Solids. 15, 319-329, 1967.

7. Hutchings, M. T., Withers, P. J., Holden, T. M. & Lorentzen, T. Introduction to the Characterization of Residual Stress by Neutron Diffraction (Taylor & Francis, 2005) pp. 213-273.

8. www.gbcsci.com

9. M. Yeadon, Scanning electron microscopy, Handbook of superconducting materials, vol. 2 (Institute of Physics publishing, Bristol and Philadelphia), 2003.

10. M. Hervieu and B. Raveay, Transmission electron microscopy, Handbook of superconducting materials, vol. 2 (Institute of Physics publishing, Bristol and Philadelphia), 2003.

11. https://en.wikipedia.org/wiki/Energy-dispersive_X-ray_spectroscopy

12. https://en.wikipedia.org/wiki/Electron_energy_loss_spectroscopy

13. www.americanmagnetics.com

14. www.tek.co

Chapter 3

Assessment of Isotopic Boron Powders for the fabrication of low activation $Mg^{11}B_2$ superconductor for fusion magnets

3.1. Introduction

Within the scope of the International Thermonuclear Experimental Reactor (ITER) project, Nb_3Sn and NbTi superconducting wires and cables are used as essential constituents of the toroidal field (TF) and poloidal field (PF) coils to contain the deuterium-tritium (D-T) fusion plasma [1-3]. Nb-based low temperature superconductors have significant drawbacks. For long-term and steady-state operation of the D-T plasma fusion reactors, it is desirable that the superconducting magnet elements have low activation [4, 5]. The Nb-based superconductors, however, require a very long period for the radioactivity to decay and to cool down after neutron irradiation [6]. Thus, this creates an additional problem for the maintenance and treatment of the radioactive wastes [6]. On the other hand, MgB_2-based superconductors have a short decay time and are known as one of the most low activation superconducting materials [7]. Furthermore, MgB_2 superconductors have a higher operating temperature compared to the Nb-based superconductors [8].

For the purpose of using MgB_2-based superconducting magnets in the fusion reactor, it is necessary to consider the properties carefully, especially the nuclear properties, of the boron precursor. Natural boron is a mixture of two isotopes, boron-10 (^{10}B; 20 %) and boron-11 (^{11}B; 80 %) [9, 10]. ^{10}B has a very large neutron absorption (capture) cross-section and is usually used as a neutron absorber in nuclear power plants in the radiation shield or control rods [11, 12]. In the neutron flux, ^{10}B is transformed to ^{7}Li and He by a neutron reaction ($^{10}B + n, \alpha \rightarrow {}^{7}Li + {}^{4}He$) [13-15]. In contrast, the ^{11}B isotope is stable with respect to neutron irradiation, lacking the (n, α) reaction, and can reduce nuclear heating [16-18]. Thus, from the practical point of view, the application of ^{11}B based $Mg^{11}B_2$ superconductors is crucial in the neutron irradiation environment, there is a definite requirement of ^{11}B to fully replace ^{10}B [18]. If the problem of ^{11}B enrichment is solved to a practically acceptable degree, we believe that $Mg^{11}B_2$ superconductor is a promising candidate to replace the NbTi superconductors in the low field fusion magnets.

A significant enhancement in the current carrying capacity and upper critical field of MgB_2 has been realized through chemical doping with carbon (C) containing compounds, such as SiC, B_4C, C and carbon nanotubes (CNT). Chemical doping is a simple and readily scalable technique. However, doping effects have been limited by the agglomeration of nanosized dopants and poor reactivity between boron (B) and C [19-24]. In order to overcome these problems, one of the co-authors proposed the carbohydrate through solution route [25]. To further improve the superconductivity, the properties of the starting B powders, such as purity, size distribution, particle size, etc., need to be considered as they play an important role in determining the fundamental properties of MgB_2.

In this study, we have analysed the ^{11}B powder and manufactured $Mg^{11}B_2$ bulk superconductor using ^{11}B-rich precursors to estimate properties which are important for application in superconducting magnets for fusion reactors. Apart from the control of the isotope composition, in the case of the powder precursors, we studied properties that are important for the reaction formation of $Mg^{11}B_2$, such as the chemical/crystal state, powder particle morphology, etc. For the fabrication of $Mg^{11}B_2$ bulks, the major focus of this study is to control the phase purity and superconducting properties of the resultant product.

3.2. Experimental Details

Three commercially available ^{11}B powders, American Elements (A) 99%, Cambridge (C) 99%, and Pavezyum (P) >95.5% (where the numbers refer to the nominal atomic fraction of ^{11}B), were obtained from each company and used as boron sources.

The phase compositions of the ^{11}B-rich powders were examined by high-resolution X-ray diffractometry (HR-XRD; ATX-G) using Cu Kα radiation. The morphology of the powder particles was characterized by scanning electron microscopy (SEM; MERLIN, Carl Zeiss). The size distribution of the ^{11}B powders was analysed using a Mastersizer S (Malvern Instruments, UK). The isotope ratio of ^{10}B to ^{11}B was examined using accelerator mass spectrometry (AMS) available at the Australian Nuclear Science and Technology Organization (ANSTO) on the basis of the AMS complex ANTARES (Australian National Tandem for Applied Research) equipped with the HVEE 846 Cs sputtering negative ion source and injector magnet [26]. The same isotope ratio was also determined through measurements of the neutron beam absorption in the powders using the KOWARI diffractometer in the neutron transmission (NT) mode [27]. Near edge X-ray absorption fine structure (NEXAFS) measurements at the 10D X-ray absorption spectrometer (XAS) B/L at the Pohang Accelerator Laboratory (PAL) and X-ray photoelectron spectroscopy (XPS; PHI 5000 Versa Probe (ULVAC PHI)) were introduced in order to investigate the chemical state of the ^{11}B.

For the production of bulk $Mg^{11}B_2$ superconductors, the ^{11}B-rich powder was mixed with Mg powder (100–200 mesh, 99%) in a molar ratio of Mg + 2B. After grinding properly in an agate mortar, the mixtures were pressed into cylindrical pellets (5 mm diameter and 2 mm thickness) under a pressure of 5 MPa. The obtained pellets were sintered at 700 °C and 800 °C under high purity Ar flow (ramp rate: 5°C/min and dwell time of 1 hour).

The phase composition and superconducting properties of the thus-produced $Mg^{11}B_2$ superconductors were measured by X-ray diffraction (XRD, GBC-MMA) and on a 9T physical properties measurement system (PPMS, Quantum Design).

3.3. Results and Discussion

The most critical property for nuclear applications, the isotope content of ^{10}B for the three ^{11}B

powders, is shown in Table 3-1. The two methods used for determining the amount of ^{10}B impurity are in general agreement, although the NT method has larger uncertainties related to the finite accuracy of the compaction density determination. The Cambridge ^{11}B (C) powder contains the largest amount of ^{10}B, and the American Elements ^{11}B (A) powder has the lowest ^{10}B content, while the Pavezyum ^{11}B (P) powder is in the middle, with content between the C powder and the A powder.

Table 3-1. Isotope ratio and size distributions of American Elements ^{11}B powder (A), Cambridge ^{11}B powder (C), and Pavezyum ^{11}B powder (B).

Materials	**Isotope composition, at % of ^{10}B (AMS, NT)**	**Mean size**	
		D [3, 2] [a] (μm)	**D [4, 3] [b] (μm)**
American Elements	0.57±0.02 0.40 ± 0.10	57.2±0.07	115.21±0.14
Cambridge	1.04±0.04 0.90 ± 0.10	21.74±0.27	67.74±0.84
Pavezyum	0.74±0.04 0.75 ± 0.10	2.68±0.03	23.47±0.29

[a] D [3,2]= The volume/surface mean (also called the Sauter mean) diameter [31].

[b] D [4,3]= The mean diameter over volume (also called the DeBroukere mean) [32].

AMS: Accelerator Mass Spectrometry, NT: Neutron Transmission mode

Fig. 3-1 presents the XRD patterns of the three different ^{11}B powders. All major diffraction peaks can be defined as β-rhombohedral boron (JCPDS: 31-0207) [28].

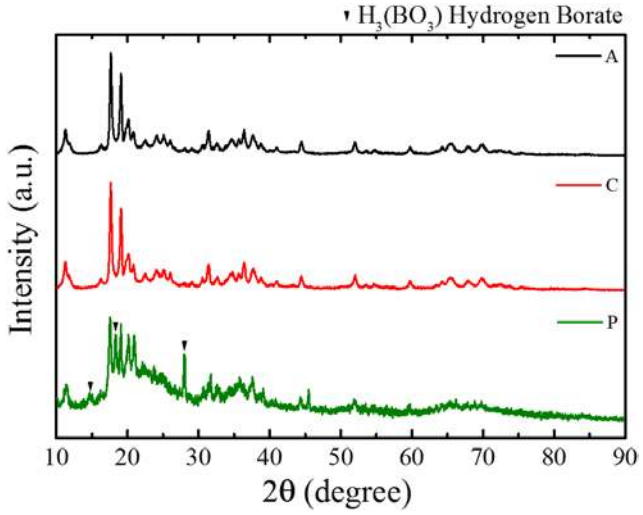

Figure 3-1. HR-XRD patterns of American Elements (A), Cambridge (C), and Pavezyum (P) 11B-

rich powders.

In the case of P, there is a significant peak broadening compared with A and C, and it has an impurity identified as $H_3(BO_3)$. Peak broadening indicates that the P powder has the lowest crystallinity and the smallest crystallite domain size among three different ^{11}B powders [29, 30]. The microstructure of the ^{11}B powders is shown in Fig. 3.2.

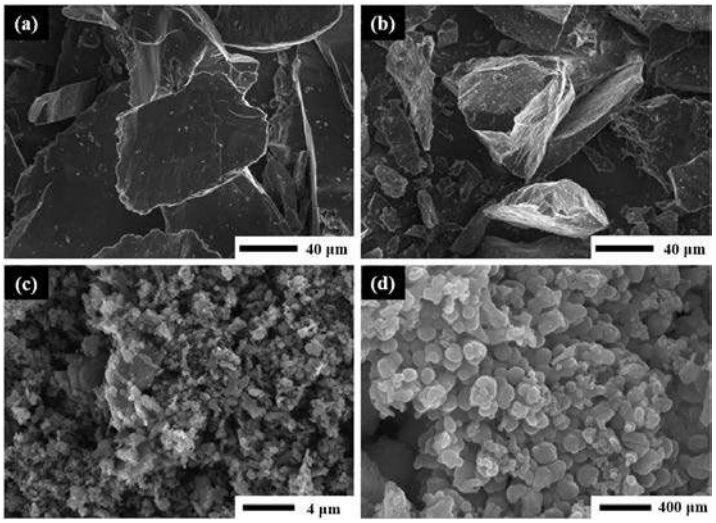

Figure 3-2. SEM images of three different ^{11}B powders: (a) American Elements ^{11}B, (b) Cambridge ^{11}B, and (c and d) Pavezyum ^{11}B-rich powders.

As seen in the SEM images, the A and C powders are micrometer-sized powders with plate-shaped particles, while P powder has spherical shaped particles of sub-micrometer-size. The mean sizes for the three ^{11}B-rich powders are shown in Table 3-1.The D [3, 2] and D [4, 3] results (explained in Table 3-1) indicate that the A powder has the largest particle size, followed by the C powder, and the P powder has the smallest particle size. The particle size analysis results are consistent between the XRD results and the SEM observations.

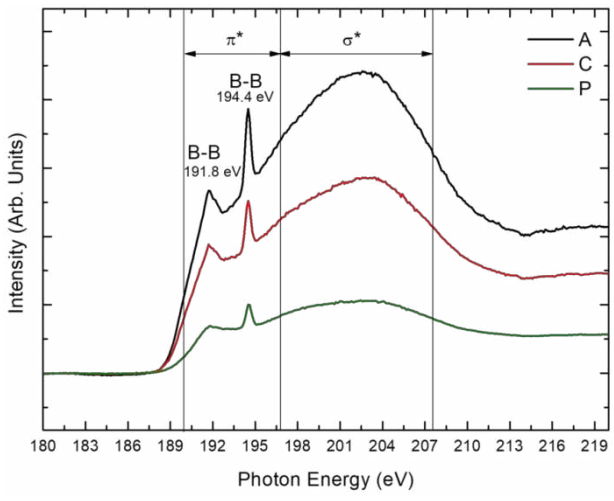

Figure 3-3. Boron 1s core level XPS spectra of ^{11}B powders: (a) American Elements ^{11}B, (b) Cambridge ^{11}B, and (c) Pavezyum ^{11}B-rich powders.

The accurate chemical bonding and structure of the ^{11}B powders were determined by NEXAFS and XPS. The B K-edge NEXAFS spectra of the ^{11}B powders can be explained by $s + p_z$ (π^* transitions) and $p_x + p_y$ (σ^* transitions) [33, 34].

The results for the individual powders are mainly very close, as shown in Figure 3-3. The peak at 191.8 eV in the NEXAFS spectra is derived from the typical B-B bonding of the elemental boron, and the sharp peak correlated with the bonding of metallic boron at 194.4 eV in the π^* resonance region is indexed as the transition of B 1s electrons to the unoccupied B $2p_z$ orbital [35, 36]. For the σ^* resonance region, there is significantly broad peak from 196 eV to 200 eV. Although ^{11}B powders do not have significant structure in the σ^* resonance region, it is suggested that ^{11}B powders have an amorphous structure or low crystallite structure [37, 38].

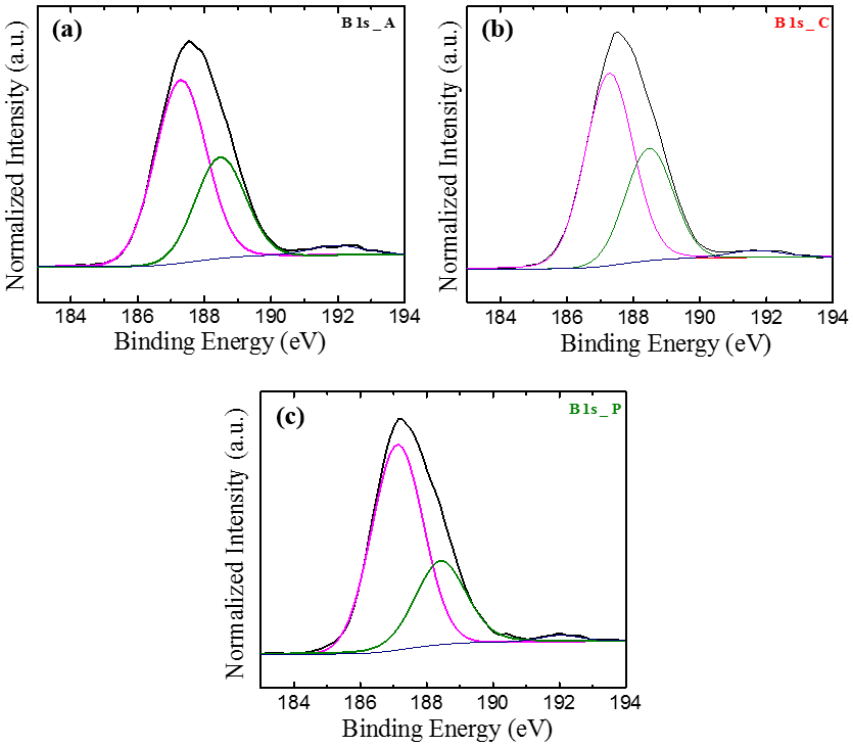

Figure 3-4. Boron 1s core level XPS spectra of ^{11}B powders: (a) American Elements ^{11}B, (b) Cambridge ^{11}B, and (c) Pavezyum ^{11}B-rich powders.

Supplementary information on the chemical bonding of these samples can be derived from core level X-ray photoemission spectroscopy. Figure 3-4 presents the core level photoemission spectra for the three sorts of ^{11}B powders. Three peaks are observed in all boron 1s signals, as shown in Figure 3-4 (a), (b), and (c), which have peak positions of 187.1−187.2 eV, 188.4 eV, and 191−192 eV [31]. The two low binding energy groups, around 187 eV and 188 eV, are most likely from B-B bonds in the ^{11}B powders [39, 40]. The weak signal peak (191−192 eV) is involved with the oxidation of ^{11}B or associated with the oxidized ^{11}B in the higher energy region [41].

It has been reported that the properties of the starting precursors (boron powders), such as crystallinity, purity, and particle size distribution, significantly influence and determine the fundamental electromagnetic and superconducting properties of the reacted MgB_2 products [42-45]. In particular, the crystalline phase, which is strongly evidenced in powders C and A, is believed to require high temperature for a full reaction between Mg and B, which decreases the superconducting current paths. Therefore, the powder with the smallest particle size and lower crystallinity was selected for the fabrication in order to improve the reaction rate and reduce the sintering temperature required to form $Mg^{11}B_2$ [46]. Consequently, the products from this powder were used for characterization of the superconducting properties of $Mg^{11}B_2$ samples, which were sintered at two temperatures, 700°C and 800°C.

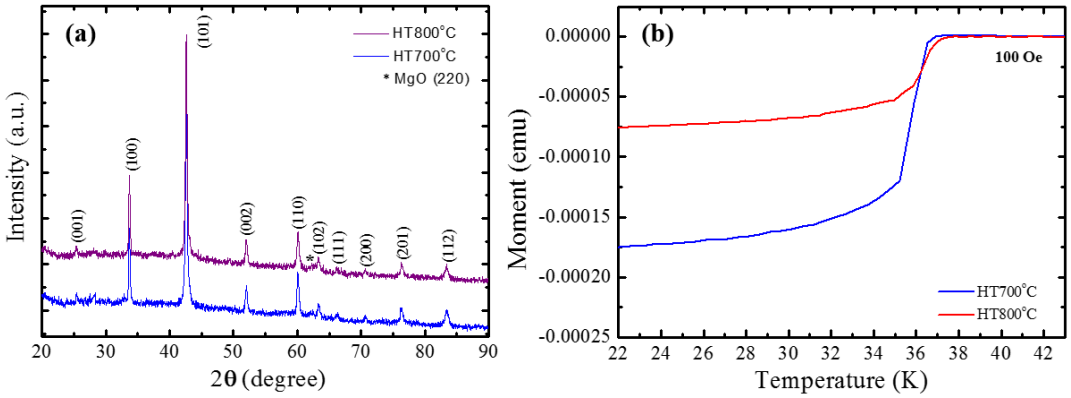

Figure 3-5. Characteristics of $Mg^{11}B_2$ bulk superconductor sintered at 700°C and 800°C: (a) XRD results for HT700°C and HT800°C. The (*hkl*) labels show $Mg^{11}B_2$ reflections. (b) Temperature dependence of the zero-field-cooled (ZFC) and field-cooled (FC) demagnetizations at 100 Oe.

The XRD analysis in Figure 3-5(a) shows that the main phase was $Mg^{11}B_2$, while MgO was also present as a second phase impurity in both bulk samples sintered at 700°C and 800°C. Figure 3-5 (b) shows the zero-field-cooled (ZFC) and field-cooled (FC) demagnetization results measured at 100 Oe for the $Mg^{11}B_2$ samples as functions of the sintering temperature, with clear normal-superconducting transitions observed in all samples with critical temperature (T_c) values of 36.5 K (HT700 °C sample) and 36.9 K (HT800 °C sample).It was shown earlier for samples made of this powder in bulk and wire form. In our previous study [47], we synthesized $Mg^{11}B_2$ using the ^{11}B (P) and systematically studied the sintering process and critical current density of low activation $Mg^{11}B_2$ superconductors. The highest J_c value (2.20 ×105 A cm^{-2} at 20 K, self-field) was obtained in the $Mg^{11}B_2$ sample sintered at 850 °C for 45 min. The high-temperature sintered samples have higher J_c at low fields compared to low-temperature sintered samples, mainly owing to their better crystallinity and grain connectivity [46-49]. Therefore, the ^{11}B (P) powder proved its potential in terms of cost and performance, and thus, it can potentially be used in the next generation superconducting fusion magnets to replace the more expensive, higher neutron activation, and lower temperature NbTi superconductors.

3.4. Conclusions

Our analysis has demonstrated that all three of the ^{11}B powders that we studied have the β-rhombohedral crystalline phase but slightly different ^{10}B isotope content as an impurity. The boron powder from Pavezyum seems to have the most optimal combination of properties amongst the three suppliers for production of $Mg^{11}B_2$ bulk superconductors: smallest particle size, the lowest crystallinity among the three ^{11}B powders, and an acceptable ^{11}B purity of 99.25%. Thus, $Mg^{11}B_2$ bulk superconductors have been successfully fabricated using this powder, and in tests, they demonstrated typical superconducting properties, which satisfy the requirements for critical temperature and current carrying capability. When considered in connection with practical manufacturing of superconducting wires and cables for potential use in future fusion reactors, the current study provides the first real demonstration and sets a reference point for $Mg^{11}B_2$-based superconducting wires.

3.5. References

1. Devred, A. et al. Challenges and status of ITER conductor production. Supercond. Sci. Technol. 27, 044001, 2014.

2. Boutboul, T. et al. Status of the Procurement of the European Superconductors for the ITER Magnets. IEEE Trans. Appl. Supercond. 24, 6001004, 2014.

3. Mitchell, N. & Devred, A. The ITER magnet system: Configuration and construction status. Fus. Eng. Des. 123, 17-25, 2017.

4. Hishinuma, Y., Kikuchi, A., Shimada, Y., Kashiwai, T., Hata, S., Yamada, S., Muroga, T., Sagara, A., Development of MgB_2 superconducting wire for the low activation superconducting magnet system operated around core D-T plasma. Fus. Eng. Des. 98-99, 1076, 2015.

5. S. Sato, H. Iida, T. Nishitani, Evaluation of shutdown gamma ray dose rates around the duct penetration by three-dimensional Monte Carlo decay gamma ray transport calculation with variance reduction method, J. Nucl. Sci. Technol. 39, 1237–1246, 2002.

6. Noda, T., Takeuchi, T. & Fujita, M. Induced activity of several candidate superconductor materials in a tokamak-type fusion reactor. J. Nucl. Mater. 329–333, 1590–1593, 2004.

7. Hishinuma, Y., Yamada, S., Sagara, A., Kikuchi, A., Takeuchi, T. Development of low activation superconducting material for the feedback coil operated around core D-T plasma, IAEA Fus. Eng. Conf. 43 FT/P1-8, 2010.

8. Paul Seidel, Applied Superconductivity: Handbook on Devices and Applications, Vol. 2 (John Wiley & Sons, London, 2015).

9. Tsiskarishvili, G. P., Lundström, T., Tegenfelt, T. J., Dolidze, V., Tsagareishvili, G. V., Isotope effect in β−rhombohedral boron, AIP Conf. Proc. 231, 280, 1991.

10. Chkhartishvili, L. Isotopic effects of boron (Review). Trends Inorg. Chem., 11, 105–167, 2009 .

11. Varley F. Sears, Neutron scattering lengths and cross sections. Neutron News 3(3), 29,1992.

12. Nikolić, R. J., Conway, A. M., Reinhardt, C. E., Graff, R. T., Wang, T. F., Deo, N., Cheung, C. L., 6:1 aspect ratio silicon pillar based thermal neutron detector filled with ^{10}B, Appl. Phys. Lett. 93, 133502, 2008.

13. Eisterer, M. et al. Neutron irradiation of MgB_2 bulk superconductors. Supercond. Sci. Technol. 15, L9-L12, 2002.

14. Wilke, R. H. T., Bud'ko, S. L. & Canfield, P. C. Systematic study of the superconducting and normal-state properties of neutron-irradiated MgB_2. Phys. Rev. B 73, 134512, 2006.

15. Putti, M. et al. Neutron irradiation of $Mg^{11}B_2$: From the enhancement to the suppression of superconducting properties. Appl. Phys. Lett. 86, 112503, 2005.

16. Mooring, F. P., Monahan, J. E. & Huddleston, C. M. Neutron cross sections of the boron isotopes for energies between 10 and 500 keV. Nucl. Phys. 82, 16–32, 1966.

17. Hinks, D.G. & Jorgensen, J. D. The isotope effect and phonons in MgB_2. Physica C 385, 98–104, 2003.

18. Tarantini, C. et al. Effects of neutron irradiation on polycrystalline $Mg^{11}B_2$. Phys. Rev. B 73,

134518, 2006.

19. S. X. Dou et al., Enhancement of the critical current density and flux pinning of MgB_2 superconductor by nanoparticle SiC doping, Appl. Phys. Lett., 81, 3419–3421, 2002.

20. J. H. Kim, W. K. Yeoh, M. J. Qin, X. Xu, and S. X. Dou, Enhancement of in-field J_c in MgB_2 /Fe wire using single- and multiwalled carbon nanotubes, Appl. Phys. Lett., 89, 122510-1–122510-3, 2002.

21. W. K. Yeoh et al., Control of nano carbon substitution for enhancing the critical current density in MgB_2, Supercond. Sci. Technol., 19, 596–599, 2006.

22. A. Ribeiro, S. L. Bud'ko, C. Petrovic, and P. C. Canfield, Carbon doping of superconducting magnesium diboride, Physica C, 384, 227–236, 2003.

23. W. Mickelson, J. Cummings, W. Q. Han, and A. Zettl, Effects of carbon doping on superconductivity in magnesium diboride, Phys. Rev. B, 65, 052505-1–052505-3, 2002.

24. A. Yamamoto et al., Effects of B_4C doping on critical current properties of MgB_2 superconductor, Supercond. Sci. Technol., 18, 1323–1328, 2005.

25. J. H. Kim, S. Zhou, M. S. A. Hossain, A. V. Pan, and S. X. Dou, Carbohydrate doping to enhance electromagnetic properties of MgB_2 superconductors, Appl. Phys. Lett., 89, 142505-1–1142505-3, 2006.

26. Tuniz, C.et al. The Antares AMS Centre: A Status Report. Radiocarbon 37(2), 663-673, 1995.

27. O. Kirstein, V. Luzin, U. Garbe, The Strain-Scanning Diffractometer Kowari, Neutron News 20, 34-36, 2009.

28. Liu, G., Yin, L., Niu, P., Jiao, W., Cheng. H., Visible-Light-Responsive β-Rhombohedral Boron Photocatalysts, Angew. Chem. Int. Ed. 52, 6242 –6245, 2013.

29. Ungár, T., Microstructural parameters from X-ray diffraction peak broadening, Script. Mater. 51, 777–781, 2004.

30. Cullity, B. D. and Stock, S. R., Elements of X-Ray Diffraction (3rded.), USA, Prentice Hall PTR, 2001.

31. Wang, D., and Fan, L.S., Fluidized Bed Technologies for Near-Zero Emission Combustion and Gasification, A volume in Woodhead Publishing Series in Energy 42–76, 2013.

32. Horiba Scientific, A guidebook to particle size analysis (2016), http://www.horiba.com/us/en/scientific/products/particle-characterization/

33. Li, D., Bancroft, G. M., Fleet, M. E., B K-edge XANES of crystalline and amorphous inorganic materials, J. Electron Spectroscopy and Related Phenomena, 79, 71-73, 1996.

34. Peter, R., Bozanic, A., Petravic, M., Chen, Y., Fan, L. J., and Yang, Y. W., Formation of defects in boron nitride by low energy ion bombardment, J. Appl. Phys. 106, 083523, 2009.

35. Petravic, M., Peter, R., Kavre, I., Li, L. H., Chen, Y., Fan, L., and Yang, Y., Decoration of nitrogen vacancies by oxygen atoms in boron nitride nanotubes, Phys. Chem. Chem. Phys. 12, 15349–15353, 2010.

36. A. F. Jankowski, I. Jimenez, J. P. Hayes, D. K. Shuh, W. M. Tong, D. G. J. Sutherland, J. A. Carlisle, L. J. Terminello, F. J. Himpsel, Near-Edge X-Ray Absorption Fine Structure Examination of Chemical Bonding in Sputter Deposited Boron and Boron-Nitride Films, Mat. Res.

Soc. Symp. Proc. 437, 207-210, 1996.

37. Zhang, D., Davalle, D.M., O'Brien, W.L., McIlroy, D.N., The chemical composition of as-grown and surface treated amorphous boron carbon thin films by means of NEXAFS and XPS, Surface Science 461, 16–22, 2000.

38. Fleet, M. E., Liu, X. Boron K-edge XANES of boron oxides: Tetrahedral B–O distances and near-surface alteration, Phys. Chem. Min. 28, 421-427, 2001.

39. Li, L., Li, L. H., Chen, Y., Dai, X. J., Xing, T., Petravic, M., Liu, X., Mechanically activated catalyst mixing for high-yield boron nitride nanotube growth, Nano. Res. Lett., 7, 417, 2012.

40. Moudler, J. F., Stickle, W. F., Sobol, P. E. and Bomben, K. D., Handbook of X-ray Photoelectron Spectroscopy (Perkin-Elmer, 1992).

41. Feng, B., Zhang, J., Zhong, Q., Li, W., Li, S., Li, H., Cheng, P., Meng, S., Chen, L., Wu, K., Experimental realization of two-dimensional boron sheets, Nat. Chem. 8, 563-568, 2016.

42. Xu, X., Yeoh, W. K., Zhang, Y., and Dou, S. X, Improved J_c of MgB_2 superconductor by ball milling using different media, Supercond. Sci. Technol. 19, L47–L50, 2006.

43. Kim, J. H., Heo, Y., Matsumoto, A., Kumakura, H., Rindfleisch, M., Tomsic, M., and Dou, S. X., Comparative study of mono- and multi-filament MgB_2 wires with different boron powders and malic acid addition, Supercond. Sci. Technol. 23, 075014, 2010.

44. Xu, X., Qin, M. J., Konstantinov, K., Santos, D.I.,Yeoh, W. K., Kim, J. H., and Dou, S. X., Effect of boron powder purity on superconducting properties of MgB_2, Supercond. Sci. Technol. 19, 466–469, 2006.

45. Chen, S. K., Yates, K. A., Blamire, M. G., and MacManus-Driscoll, J. L., Strong influence of boron precursor powder on the critical current density of MgB_2, Supercond. Sci. Technol. 18, 1473–1477, 2005.

46. Cai, Q., et al. Doping-Induced Isotopic $Mg^{11}B_2$ Bulk Superconductor for Fusion Application, Energies 10, 409, 2017.

47. Cheng, Fang; Liu, Yongchang; Ma, Zongqing; et al. Sintering process and critical current density of low activation (MgB_2)-B-11 superconductors from low temperature to high temperature. Physica C, 527, 9–13, 2016.

48. Qiu, W. et al. Improvement in the transport critical current density and microstructure of isotopic $Mg^{11}B_2$ monofilament wires by optimizing the sintering temperature. Sci. Rep. 6 36660, 2016.

49. Cheng, F., Improved Superconducting properties in the $Mg^{11}B_2$ low activation superconductor prepared by low-temperature sintering, Sci. Rep. 6, 25498, 2016.

Chapter 4

Superior Transport J_c Obtained in in-situ MgB_2 Wires by Tailoring the Starting Materials and using a Combined Cold High Pressure Densification and Hot Isostatic Pressure Treatment MgB_2 Superconductor

4.1. Introduction

The superconductivity at 39 K that was discovered in MgB_2 with its simple binary chemical composition has attracted much interest in its fabrication techniques and practical applications due to its low density, good compositional tolerance, and easy fabrication methods [1]. Its electrical applications are largely determined by its current carrying capability, i.e. the critical current density (J_c) of the superconductor at the service temperature. Therefore, many researchers have been trying to improve the J_c of MgB_2 since its discovery in 2001. Although considerable progress has been made towards improving the fabrication and performance of MgB_2 during this period [2-4], the critical current density in MgB_2 is still not satisfactory compared to the expectations for its large-scale application.

Strong pinning strength and connections between grains are the critical factors determining the performance of the upper critical field (B_{c2}) and in-field J_c in the Type II superconductors. Flux pinning strength in MgB_2 is closely associated with its elementary pinning force and grain size [5,6]. On the other hand, grain connectivity is generally suppressed by voids, an insulating oxide phase, and imperfect connections between grains [6]. Yamamotoet al. [7] investigated this issue by designing a percolation model and showed that the grain connectivity could be defined as a function of the packing factor. Accordingly, significant improvement might be achieved by increasing the in-field J_c if it were possible to enhance both the flux pinning strength and the grain connectivity at the same time. It is actually difficult in practice, however, to balance the connectivity and flux pinning strength of MgB_2 during the preparation process. A variety of processing techniques have been investigated to improve J_c in MgB_2 superconductors in the last 15 years, including irradiation [8,9], chemical doping [10–16], and ball milling [17–20]. Among them, carbon doping has been proved to be the currently most effective way of improving J_c, especially at high fields [11,13]. Nevertheless, all these techniques have focused on enhancing flux pinning by engineering grain boundaries or introducing nano-impurities and lattice defects, but they have tended to neglect and even worsen the associated issues of connectivity.

In particular, the corresponding issue of connectivity plays a more vital role in determining the J_c performance in the low field region in MgB_2 wires because the low density that currently exists within the filament cores has been a serious obstacle in reaching high J_c values for in-situ MgB_2 wires. In addition, the reaction between magnesium and boron to form MgB_2 involves a volume contraction that produces a final density limited to about 50% of the theoretical density (2.36 g/

cm^3) [6]. Consequently, the typical effective cross-sectional superconducting area in MgB_2 wire is only about 10% [21]. According to Rowell [21], the porosity of the wires strongly affects the grain connectivity of the grains in the finished wires, thus resulting in decreased wire performance. Several attempts have been undertaken to enhance the mass density of in-situ filaments by applying high pressure during the reaction heat treatment, by methods such as hot isostatic pressure (HIP) and other forms of hot pressing [22–27]. Cold densification was also applied as an alternative to the application of pressure at high temperature [28–30]. None of these high pressure processes, however, has the potential to be applied on long wire lengths. Very high mass densities in MgB_2 wires (up to 100%) can be produced without external pressure by using the infiltration method, originally proposed by Giunchi et al. [31]. Hur et al. [32] and Togano et al. [33] applied this technique to a wire configuration and found very high critical current densities in ring shaped MgB_2 filaments. The hollow centre of these filaments, however, introduces new homogeneity problems and a small superconducting filling factor, both of which require further development.

The application of cold high pressure densification (CHPD) on long wires, leading to significant enhancement of J_c, was undertaken at the University of Geneva by Flükiger et al. [34] and Hossain et al. [35], on binary and alloyed MgB_2 wires, respectively. Since no degradation of J_c was observed at the overlapping pressure zones between two pressed regions when compared to short wire lengths, these authors extended the CHPD method to lengths exceeding 10m, a first step towards industrial lengths [36].

In the previous sections, it was mentioned that HIP is not suitable for the production of wires with industrial length due to several reasons: a) the possibility of Ar gas being trapped inside the filament, b) the limitation of applied gas pressure to 0.2 GPa, and c) the size of the pressure chamber being too small for reacting wires in km lengths. In order to avoid these difficulties, a new type of HIP device was recently constructed at the Institute of High Pressure Physics in Poland, and HIP was successfully applied on long lengths of wires [37]. This new toroid-type isostatic hot press enables the production of very long lengths of MgB_2 wire. Second stage densification using the toroidal HIP chamber after CHPD has been applied on optimized CHPD treated wires under the collaboration between the University of Wollongong, Australia and the Institute for High Pressure Physics, Unipress, Poland.

In the present work, both the CHPD and the HIP techniques were applied to in-situ PIT MgB_2 wires to increase mass density and further promote grain connectivity. In combination with the usage of optimized carbon-encapsulated boron as precursor, the highest J_c has been obtained for our in-situ CHPD + HIP PIT wires, and this result is very comparable to the performance of second generation MgB_2 wires produced by the Advanced Internal Magnesium Infiltration (AIMI) technique [38].

4.2. Experimental Details

C-encapsulated amorphous boron powder (with a C percentage of about 2.30 wt.%) was obtained from Pavezyum Advanced Chemicals (PAVEZYUM) as the boron precursor. They produce

carbon encapsulated amorphous boron powder through pyrolysis of a mixed gas consisting of diborane gas (B_2H_6), hydrogen, and hydrocarbon (C_xH_y) under inert conditions [39]. Then, the boron precursor was mixed with magnesium coarse powder (99.9%, 150 μm) in a molar ratio of Mg + 2B. MgB_2 wires were fabricated by the in-situ powder in-tube (PIT) process. The mixed Mg + 2B powder was firstly packed into metal tubes with an Nb barrier and a Monel outer sheath. Then, the tube was drawn to wire with 0.83 mm outer diameter (OD). After that, pressure (about 1.8 GPa) was applied to the MgB_2 wires using the CHPD device (Figure 4-1(a)) at room temperature after drawing, just before the final reaction heat treatment. It is clear from Figure 4-1(a) that high pressure on the wire is uniformly applied from four sides via hard metal anvils at room temperature. After CHPD treatment, it was found that the cylindrical wires had been deformed into cuboid wires with a significant reduction of volume [34,35]. Consequently, a sizable enhancement of the mass density in MgB_2 wires can be obtained by CHPD, as reported in our previous studies [34,35]. After CHPD treatment, HIP (about 1.4 GPa in pressure) was applied to MgB_2 wires at 700 °C for 20 min. The CHPD-treated carbon-encapsulated MgB_2 wires were placed in the toroidal molten-salt-based HIP chamber (designed and built at IHPP, Poland) for further densification during the reaction [37]. In this device (Figure 4-1(b)), the pressing medium consists of molten salt (specific eutectic mixtures of salts (i.e. NaCl and KCl) along with boron nitride (BN)) instead of gas. BN is used for its high chemical stability and plasticity. In this process, a long wire sample is kept inside the salt bed in a sealed high pressure chamber. At the desired temperature the solid salt mixture melts in the high pressure chamber, which is tightly closed. External forces on the upper cover are directly transmitted to the pressure chamber before it reaches the reaction temperature of 700 °C. This new toroid type isostatic hot press enables the production of very long lengths of MgB_2 wire. A schematic illustration of the first prototype of the liquid-salt-based HIP machine is shown in Figure 4-1(b). The morphology of the carbon-encapsulated boron precursor and the as-prepared MgB_2 wire samples was observed by scanning electron microscopy (SEM) on a JEOL JSM-7500FA, as well as by transmission electron microscopy (TEM) on a TEM with electron energy loss spectroscopy (EELS). The transport J_c values were measured as a function of applied magnetic field in a 15 T magnet at 4.2 K in a He flow cryostat using the four-probe technique, with currents up to 200 A.

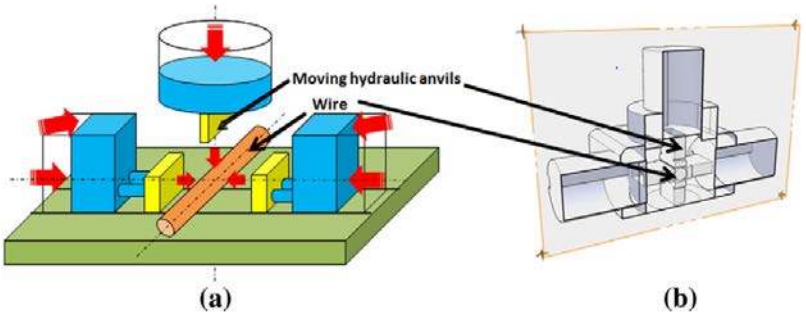

Figure 4-1. Schematic illustrations and photographs of (a) CHPD [31,32] and (b) HIP [37] devices.

4.3. Results and Discussion

Figure 4-2 presents schematic diagrams of the process for preparing MgB_2 wires and the corresponding microstructures of boron or magnesium within the wires at different stages. As shown in the TEM image of the C encapsulated boron precursor in Figure 4-2(a), the boron particles are very small (about 150–200 nm in size) and in the amorphous state. Observing more carefully, it can be found that these boron particles are homogeneously coated by some kind of thin layer. In combination with the EELS results, it is clear that the coating layer is carbon-rich, which indicates that the carbon is indeed mainly concentrated at the surfaces of the B particles and encapsulates them uniformly during the pyrolysis process, as we reported in our previous study [39]. Compared to other techniques for introducing carbon doping, such as solid state mixing and the chemical solution route [11–13], the significant advantages of using this C-encapsulated B as a precursor are that an appropriate level of carbon substitution can be achieved more homogeneously in the finally sintered MgB_2 wires at low cost and that the whole process is precisely controlled [39]. SEM images of the elongated fibrous Mg in the PIT MgB_2 wires after drawing and after CHPD treatment are presented in Figure 4-2(b) and (c), respectively. Obviously, the coarse Mg original particles in the PIT wires are gradually deformed into Mg fibres as the size of the wires is decreased to the final diameter by drawing. Uchiyama et al. [40] reported that such behaviour of Mg in the PIT wires exists because magnesium is more ductile than boron, and during cold-working, the magnesium powder can be easily elongated along the wire direction, resulting in such fibrous structure within the wire core. During the process of Mg elongation, it is very important how well the nano-boron is uniformly and homogeneously distributed and diffused on the surfaces of the elongated Mg grains with minimum energy. Therefore, the application of CHPD prior to heat treatment is very crucial, not only for the uniform distribution of nano-boron particles, but also for minimizing the voids and empty spaces after drawing. After the CHPD process, this deformation of Mg is further enhanced, and the Mg fibres are elongated (see the element map of Mg within the wires after CHPD in Figure 4-2(c)). Finally, the diameter of these Mg fibres can be reduced down to approximately 40 μm. Elongated voids with reduced size can still exist in the original positions of the elongated Mg fibres after the heat treatment due to the volume shrinkage as a result of the chemical reaction between Mg and B, and may be further minimized during the HIP process. In this way the shape and direction of the void can be effectively controlled and aligned along the wire direction using the coarse Mg as starting material, as discussed in our previous work [41]. Consequently, the electrical current can percolate easily with less obstruction in this kind of microstructure and thus improve the grain connectivity as well as the current carrying capacity.

Figure 4-3 shows the microstructure of the superconducting core within the MgB_2 wire after HIP treatment and after traditional sintering for comparison. It is clear that the amount and size of the voids are reduced, and the density during sintering has been further increased in the HIP treated MgB_2 wire compared to traditional sintered wire (see Figure 4-3(a) and (b)).

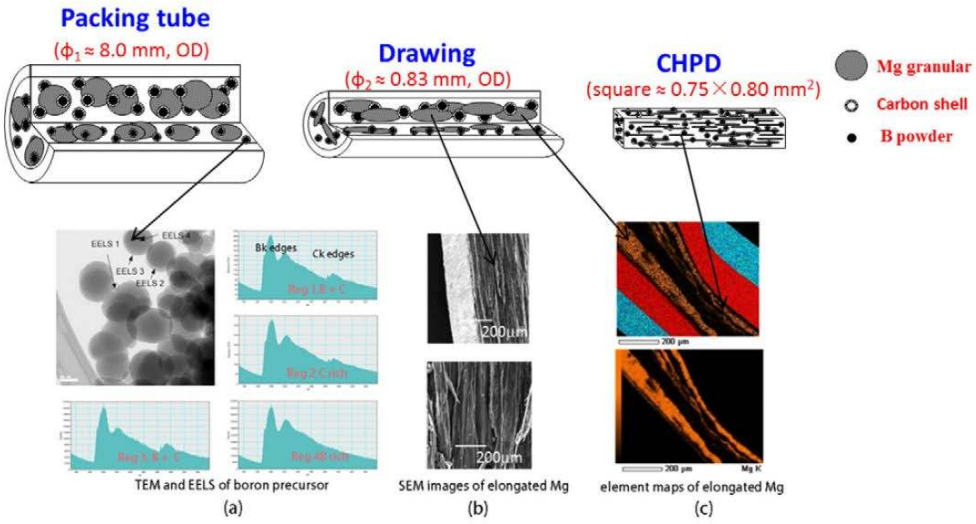

Figure 4-2. Schematic diagrams of the process for preparing MgB_2 wires and the corresponding microstructures of the boron or magnesium within the wires at different stages.

It should be understood that the isostatic pressure is employed synchronously during the reaction process between Mg and B, which can further compact the superconducting core and compensate for the whole volume shrinkage. HIP without the CHPD stage is not very effective because high energy may be needed for the diffusion between the starting materials, which can destroy the linear fibrous structure and cause a mismatch of the boron distribution among the Mg grains. So, the application of HIP on the densified filament is obviously more beneficial, because minimum diffusion energy is needed to form homogeneous grains.

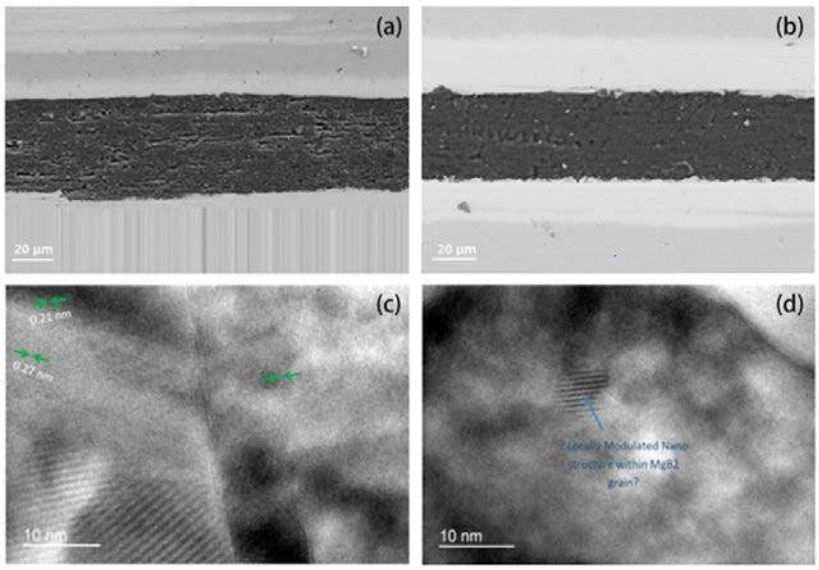

Figure 4-3. (a, b) SEM and (c, d) TEM images of the microstructure of the superconducting core within the MgB_2 wire after HIP treatment.

In addition, comparing Figure 4-3(c) with (d), clear and regular lattices are observed throughout

whole MgB_2 grains in the traditional heat-treated wire, while some locally modulated nanostructure exists within the MgB_2 grains in the wire treated by HIP. The presence of this modulated nanostructure could be attributed to the microstrain resulting from HIP treatment. Based on the above results, usage of coarse Mg particles as precursor, together with CHPD and HIP treatment, is capable of dramatically increasing the mass density and decreasing the amount and size of voids, as well as controlling their shape and alignment. All these factors are beneficial for the connections between grains. Moreover, carbon-encapsulated amorphous boron precursor can introduce sufficient homogeneous carbon substitution into the boron, and the combination of CHPD and HIP treatment can significantly improve the grain connectivity, increase the uniformity in the MgB_2 filament, and increase the number of dislocations (Figure 4-3). Gajda et al. [42] demonstrated considerable enhancement of J_c in both the high and low field regions after HIP treatment, which was due to the contribution of point and surface pinning centres, respectively, as well as the considerable reduction of voids.

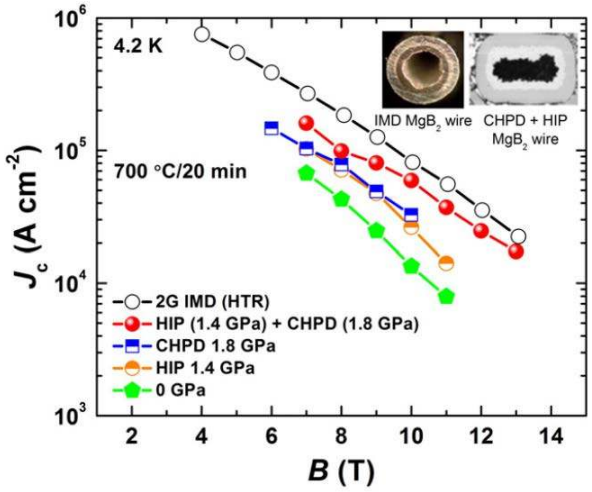

Figure 4-4. Magnetic field dependence of the transport critical current density (J_c) at 4.2 K for the CHPD and HIP co-treated MgB_2 wires with carbon encapsulated amorphous boron precursor and course Mg powder. For comparison, the magnetic field dependence of the transport critical current density (J_c) for a traditional PIT MgB_2 wire, an internal Mg diffusion (IMD) MgB_2 wire [38], a solely CHPD treated PIT MgB_2 wire, and a solely HIP treated PIT MgB_2 wire is also presented here. The insets are photographs of cross sections of (left) the IMD MgB_2 wire and (right) the MgB_2 wire prepared in this work.

To confirm this, the transport critical current density (J_c) was measured, and the corresponding magnetic field dependence of the transport critical current density at 4.2 K for the CHPD and HIP co-treated MgB_2 wires with carbon encapsulated amorphous boron precursor is presented in Figure 4-4. As references, the magnetic field dependence of the transport critical current density (J_c) for a traditional PIT MgB_2 wire, an internal Mg diffusion (IMD) MgB_2 wire, a solely CHPD treated PIT MgB_2 wire, and a solely HIP treated PIT MgB_2 wire is also presented in Fig. 4.4.

Obviously, the values of J_c for the CHPD and HIP co-treated MgB_2 wire are four times higher than for the traditional PIT MgB_2 wire without any treatment. The J_c performance of the solely CHPD treated wire and the solely HIP treated wire are also both higher than for the traditional PIT MgB_2 wire, whereas they are inferior compared to the CHPD and HIP co-treated wire. Neither CHPD nor HIP treatment alone is sufficient to increase the mass density. Only a collaborative effort using both CHPD and HIP treatment can effectively enhance the mass density, minimize the voids, and enhance the J_c overall in both the high and low magnetic field regions due to the uniform carbon substitution (Figure 4-3 and 4-4). Generally, CHPD treatment alone compacts the original particles in the PIT MgB_2 wire, deforms these particles, and reduces the space between them, leading to an increase in the original packing density and filling factor. It has little effect, however, on the formation of voids as a result of the reaction between Mg and B during heat-treatment. On the other hand, HIP treatment can make up for this limitation of CHPD treatment and reduce such voids.

It is worth noting that the J_c performance of the CHPD and HIP cotreated PIT MgB_2 wires in our work is close to that of IMD MgB_2 wires reported in previous studies [38]. Although the IMD MgB_2 wires exhibit the highest J_c values among all the MgB_2 wires reported to date [38], there are still serious shortcomings in the process for scaling-up these IMD second generation (2G) MgB_2 wires for applications. During the IMD process, the Mg diffuses into the B layer, forming a hollow wire, and there is only a thin layer of MgB_2 in the interior of the sheath tube (see its cross-section in the left inset of Figure 4-4). As a result, the filling factor is very low (generally approximately 18%), and thus, the corresponding engineering critical current density (J_e) performance is not as remarkable as their J_c performance. Moreover, their mechanical performance is inferior due to this hollow structure, especially when the wire is twisted into coils, which is essential to fabricate various practical superconducting devices. On the contrary, the cores of the CHPD and HIP co-treated PIT MgB_2 wires in our work are full of solid superconducting MgB_2, and thus, the filling factor is very high (see the cross-section of this wire in the right inset of Figure 4-4). One can imagine that this structure in our as-prepared wires leads to higher J_e as well as better mechanical properties than in IMD MgB_2 wires.

4.4. Conclusions

In summary, various techniques, including CHPD, HIP, and the usage of coarse Mg particles and carbon-encapsulated amorphous boron precursor were collaboratively employed to improve the J_c performance of PIT MgB_2 wires in the present work. Consequently, the best J_c performance was obtained among all the PIT MgB_2 wires reported so far, due to their improved grain connectivity and enhanced flux pinning strength. Our work suggests that the economical starting precursors and the combination of cold and hot densification techniques could represent a promising alternative for industrial and economical production of practical MgB_2 wires with excellent J_c. The techniques achieved from this work will be applied in low activation $Mg^{11}B_2$ superconductors for improving the connectivity in the filament in the future work.

4.5. References

1. J. Nagamatsu, N. Nakagawa, T. Muranaka, Y. Zentani, J. Akimitsu, Superconductivity at 39 K in magnesium diboride, Nature 410, 63–64, 2001.

2. Z.Q. Ma, Y.C. Liu, Low-temperature synthesis of MgB_2 superconductors, Int. Mater. Rev. 56, 267–286, 2011.

3. D. Patel, M.S.A. Hossain, A.Motaman, S. Barua, M. Shahabuddin, J.H. Kim, Rational design of MgB_2 conductors toward practical applications, Cryogenics 63, 160–165, 2014.

4. M. Tomsic, M. Rindfleisch, et al., Development of magnesium diboride (MgB_2) wires and magnets using in situ strand fabrication method, Physica C 456, 203, 2007.

5. G. Zerweck, On pinning of superconducting flux lines by grain boundaries, J. Low Temp. Phys. 42, 1–9, 1981.

6. E.W. Collings, M.D. Sumption, M. Bhatia, M.A. Susner, S.D. Bohnenstiehl, Prospects for improving the intrinsic and extrinsic properties of magnesium diboride superconducting strands, Supercond. Sci. Technol. 21, 103001, 2008.

7. A. Yamamoto, J. Shimoyama, K. Kishio, T. Matsushita, Limiting factors of normal-state conductivity in superconducting MgB_2: an application of mean-field theory for a site percolation problem, Supercond. Sci. Technol. 20, 658–666, 2007.

8. Y. Bugoslavsky, L.F. Cohen, G.K. Perkins, M. Polichetti, T.J. Tate, R. Gwilliam, A.D. Caplin, Enhancement of the high-magnetic-field critical current density of superconducting MgB_2 by proton irradiation, Nature 411, 561–563, 2001.

9. M. Eisterer, M. Zehetmayer, S. Tonies, H.W. Weber, M. Kambara, N.H. Babu, D.A. Cardwell, L.R. Greenwood, Neutron irradiation of MgB_2 bulk superconductors, Supercond. Sci. Technol. 15, L9–L12, 2002.

10. J.S. Slusky, N. Rogado, K.A. Regan, Loss of superconductivity with the addition of Al to MgB_2 and a structural transition in $Mg_{1-x}Al_xB_2$, Nature 410, 343–345, 2001.

11. S.X. Dou, S. Soltanian, J. Horvat, X.L. Wang, S.H. Zhou,M. Ionescu, H.K. Liu, Enhancement of the critical current density and flux pinning of MgB_2 superconductor by nanoparticle SiC doping, Appl. Phys. Lett. 81, 3419–3421, 2002.

12. S. Zhou, A.V. Pan, D. Wexler, S.X. Dou, Sugar Coating of Boron Powder for Efficient Carbon Doping of MgB_2 with Enhanced Current-Carrying Performance, Adv. Mater. 19, 1373–1376, 2007.

13. J.H. Kim, S. Zhou, M.S.A. Hossain, A.V. Pan, S.X. Dou, Carbohydrate doping to enhance electromagnetic properties of MgB_2 superconductors, Appl. Phys. Lett. 89 (14), 142505, 2006.

14. Z.Q. Ma, Y.C. Liu, Q.Z. Shi, Q. Zhao, Z.M. Gao, The improved superconductive properties of MgB_2 bulks with minor Cu addition through reducing the MgO impurity, Physica C 468, 2250–2253, 2008.

15. W.K. Yeoh, J.H. Kim, J. Horvat, S.X. Dou, P. Munroe, Improving flux pinning of MgB_2 by carbon nanotube doping and ultrasonication, Supercond. Sci. Technol. 19, L5–L8, 2006.

16. C. Shekhar, R. Giri, R.S. Tiwari, O.N. Srivastava, S.K. Malik, High critical current density and

improved flux pinning in bulk MgB_2 synthesized by Ag addition, J. Appl. Phys. 101, 043906, 2007.

17. A. Gumbel, J. Eckert, G. Fuchs, K. Nenkov, K.-H. Muller, L. Schultz, Improved superconducting properties in nanocrystalline bulk MgB_2, Appl. Phys. Lett. 80, 2725–2727, 2002.

18. M. Herrmann, W. Haessler, C. Rodig, W. Gruner, B. Holzapfel, L. Schultz, Touching the properties of NbTi by carbon doped tapes with mechanically alloyed MgB_2, Appl. Phys. Lett. 91, 082507, 2007.

19. Z.Q. Ma, Y.C. Liu, J. Huo, Z.M. Gao, MgB_2 superconductors with abnormally improved J_c sintered after autoxidation of milled original powders, J. Appl. Phys. 106, 113911, 2009.

20. X. Xu, J.H. Kim, M.S.A. Hossain, J.S. Park, Y. Zhao, S.X. Dou, W.K. Yeoh, M. Rindfleisch, M. Tomsic, Phase transformation and superconducting properties of MgB_2 using ball-milled low purity boron, J. Appl. Phys. 103, 023912, 2008.

21. J.M. Rowell, The widely variable resistivity of MgB_2 samples, Supercond. Sci. Technol. 16, R17, 2003.

22. M.S.A. Hossain, C. Senatore, R. Flukiger, M.A. Rindfleisch, M.J. Tomsic, J.H. Kim, S.X. Dou, Supercond. The enhanced J_c and Birr of in situ MgB_2 wires and tapes alloyed with $C_4H_6O_5$ (malic acid) after cold high pressure densification, Sci. Technol. 22, 095004, 2009.

23. A. Sequis, L. Civale, et al., Hot isostatic pressing of powder in tube MgB_2 wires. Appl. Phys. Lett. 82, 2847, 2003.

24. K. Adamczyk, A. Morawski, et al., Superconducting Properties Comparison of SiC Doped Multifilamentary MgB_2 Wires of Various Sheaths (Cu, Monel, Glidcop) After High Pressure HIP Treatment, IEEE Trans. Appl. Supercond. 22, 6200204, 2012.

25. T.A. Prikhna, W. Gawalek, Y.A. Savchuk, V.E. Moshchil, M. Wendt, S.N. Dub, T. Habisreuther, V.S. Melnikov, A.V. Kozyrev, S. Ch, J. Dellith, D. Litzkendorf, P.A. Nagorny, U. Dittrich, V.B. Sverdun, L.K. Kovalev, V. Penkin, W. Goldacker, O.A. Rozenberg, J. Noudem, Peculiarities of high-pressure and hot-pressing manufacture of MgB_2-based blocks with high critical currents for electrical machines, J. Phys. Conf. Ser. 97, 012022, 2008.

26. H. Yamada, M. Igarashi, Y. Nemoto, Y. Yamada, K. Tachikawa, H. Kitaguchi, A. Matsumoto, H. Kumakura, Improvement of the critical current properties of in situ powder-in-tube-processed MgB_2 tapes by hot pressing, Supercond. Sci. Technol. 23, 045030, 2010.

27. D. Gajda, A. Morawski, A. Zaleski, T. Cetner, The Influence of Ex Situ MgB_2 Barrier and HIP on the I_c Anisotropy in Double Core MgB_2/Cu Wires, Acta Phys. Pol. A 118, 1059, 2010.

28. T. Matsushita, M. Kikuchi, A. Yamamoto, J.I. Shimoyama, K. Kishio, Supercond. Essential factors for the critical current density in superconducting MgB_2: connectivity and flux pinning by grain boundaries, Sci. Technol. 21, 015008, 2008.

29. W. Pachla, P. Kovac, R. Diduszko, A. Mazur, I. Husek, A. Morawski, A. Presz, Effects of the high-pressure treatment of ex situ MgB_2 superconductors, Supercond. Sci. Technol. 16, 7, 2003.

30. P. Kovac, I. Husek, W. Pachla, M. Kulczyk, Properties of seven-filament in situ MgB_2/Fe composite deformed by hydrostatic extrusion, drawing and rolling, Supercond. Sci. Technol. 20 (7), 607–610, 2010.

31. R. Flükiger, M.S.A. Hossain, C. Senatore, Supercond. Strong enhancement of J_c and Birr in binary in situ MgB_2 wires after cold high pressure densification, Sci. Technol. 22, 08500, 2009.
32. M.S.A. Hossain, C. Senatore, R. Flukiger, M.A. Rindfleisch, M. Tomsic, J.H. Kim, S.X. Dou, The enhanced J_c and Birr of in situ MgB_2 wires and tapes alloyed with $C_4H_6O_5$ (malic acid) after cold high pressure densification, Supercond. Sci. Technol. 22, 09504, 2009.
33. G. Giunchi, S. Raineri, R. Wesche, P.L. Bruzzone, The voltage–current relations for MgB_2 obtained by reactive liquid infiltration, Physica C 401, 310, 2004.
34. J.M. Hur, K. Togano, A. Matsumoto, H. Kumakura, H. Wada, K. Kimura, Fabrication of high-performance MgB_2 wires by an internal Mg diffusion process, Supercond. Sci. Technol. 21, 032001, 2008.
35. K. Togano, J.M. Hur, A.Matsumoto, H. Kumakura, Supercond. Fabrication of seven-core multi-filamentary MgB_2 wires with high critical current density by an internal Mg diffusion process, Sci. Technol. 22, 015003, 2009.
36. R. Flükiger, M.S.A. Hossain, M. Kulich, C. Senatore, Technical aspects of cold high pressure densification (CHPD) on long lengths of In Situ MgB_2 wires with enhanced J_c values, Adv. Cryog. Eng. 58, 353–362, 2012.
37. T. Cetner, A. Morawski, et al., Hot isostatic pressing of multifilamentary MgB_2 wires in solid state media for large scale application, Supercond. Sci. Technol. 28 (4), 045009, 2015.
38. G.Z. Li, M.D. Sumption, J.B. Zwayer, M.A. Susner, C.J.M. Tomsic, E.W. Collings, Effects of carbon concentration and filament number on advanced internal Mg infiltration-processed MgB_2 strands, Supercond. Sci. Technol. 26 (9), 095007, 2013.
39. S. Barua, M.S.A. Hossain, Z.Q.Ma, D. Patel, M. Mustapic, J.H. Kim, M. Somer, S. Acar, I. Kokal, A. Morawski, T. Cetner, D. Gazda, Superior critical current density obtained in MgB_2 bulks through low-cost carbon-encapsulated boron powder, Scr. Mater. 104, 37–40, 2015.
40. D. Uchiyama, K. Mizuno, T. Akao,M. Maeda, T. Kawakami, H. Kobayashi, Y. Kubota, K. Yasohama, Fibrous structure and critical current density of MgB_2 superconducting wire, Cryogenics 47, 282–286, 2007.
41. J.H. Kim, S.J. Oh, H. Kumakura, A. Matsumoto, Y.U. Heo, K.S. Song, Y.M. Kang, M. Maeda, M. Rindfleisch, M. Tomsic, S.Y. Choi, S.X. Dou, Tailored Materials for High-Performance MgB_2 Wire, Adv. Mater. 23, 4942–4946, 2011.
42. D. Gajda, A. Zaleski, A. Morawski, T. Cetner, C.J. Thong, M.A. Rindfleisch, Point pinning centers in SiC doped MgB_2 wires after HIP, Supercond. Sci. Technol. 29, 085010, 2016.

Chapter 5

Doping-Induced Isotopic $Mg^{11}B_2$ Bulk Superconductor for Fusion Application

5.1. Introduction

Fusion power is one of the most promising energy source candidates to solve global energy problems, considering its safety and green merits compared with conventional mineral energy sources. In the world-class International Thermonuclear Experimental Reactor (ITER) fusion energy project, the superconducting magnet system serves as a key determinant (Figure 5-1). A high and steady magnetic field needs to be produced to confine the deuterium (D)–tritium (T) burning plasma inside the ITER Tokamak nuclear fusion reactor. According to the previous ITER plan, hundreds of tons of superconducting cables made from NbTi and Nb_3Sn strands have been fabricated to assemble 18 Nb_3Sn toroidal field (TF) coils, a 6-module Nb_3Sn central solenoid (CS) coil, six Nb-Ti poloidal field (PF) coils, and nine pairs of Nb-Ti correction coils (CC) [1,2,3]. ITER is aimed at demonstrating the feasibility of fusion energy, but for the next step, the development of a commercial fusion reactor there is a concern that, after irradiation, ^{93}Nb be transformed into the long-lived nuclide ^{94}Nb with a half-life of about 20,000 years [4,5]. Hence, coil maintenance and repairs may become more cumbersome and the recycling of irradiated Nb-based alloys may call for tens of thousands of years of waiting for them to "cool down". Meanwhile, thicker shielding will be necessary for long-term operation. For the convenience of radioactive waste treatment and environmental protection, the radioactivation properties of superconducting components within the fusion reactor should be taken into account. The superconductivity of MgB_2 was discovered in 2001 [6]. It is well-known for its simple binary chemical composition and much higher critical transition temperature (T_c) of 39 K than that of NbTi at 9.3 K. In order to operate Nb-based low-temperature superconductors, the core of the magnet needs to be cooled down to 4 K. The only eligible cryogen is liquid helium, which is extremely expensive, not always available, and very difficult to handle. In the case of MgB_2, a working temperature as high as 20 K is low enough to achieve acceptable performance. Remarkably, the operating cost is expected to be cut by over 50% by substituting cryocooler-cooled MgB_2 materials at 20 K for liquid-helium-cooled Nb-based superconductors. Therefore, due to the advantages of cost-effectiveness, lower radioactivation, and the shorter decay time of isotopic $Mg^{11}B_2$, fundamental research on $Mg^{11}B_2$ superconducting wires will be valuable for improving the efficiency of practical application in high-irradiation environments such as fusion reactors. Nevertheless, the application of the un-doped MgB_2 remains limited by the sensitivity of the critical current density (J_c) to the increasing applied magnetic field [7]. By yielding an enhancement of J_c especially at high field, chemical doping enabled MgB_2 to meet higher demand in practical application, and carbon-containing compounds definitely attracted the most attention

within the dopant's family.

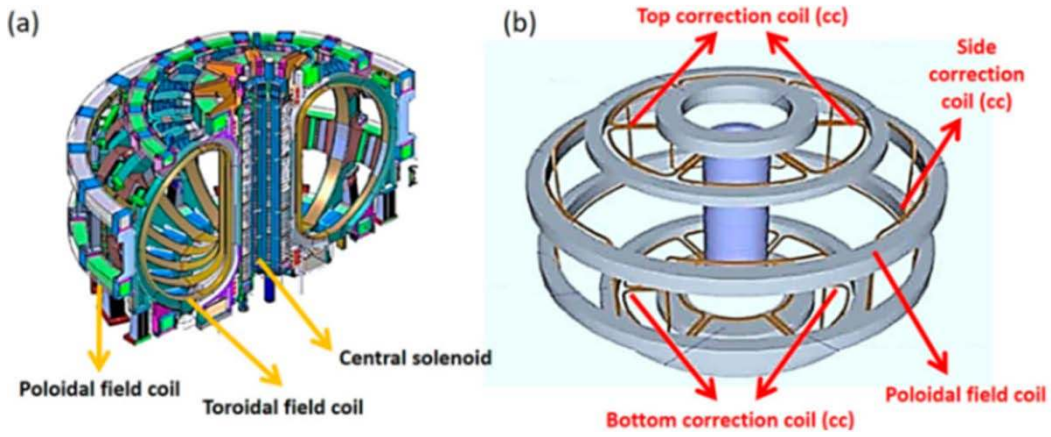

Figure 5-1. (a) 3D illustration of superconducting magnet consisting of poloidal field (PF), toroidal field (TF), and central solenoid (CS) coils; and (b) replaceable parts with MgB_2 [1,2].

MgB_2 bulks and wires with carbon addition, for instance, malic acid [8], graphene, coronene, or glucose [9,10,11], have been under investigation, motivated by the potential response of carbon atoms (compared to boron) to donate their additional valence electrons to the σ conduction band. Glycine ($C_2H_5NO_2$, Glycine) was doped into MgB_2 bulks by a series of techniques in our previous study [12,13]. The dominating mechanism for the enhancement of the J_c lied in the MgO formation in advance of the Mg-B solid-solid reaction, and the simultaneously released carbon atoms provided a certain contribution as well, by substitution the B sites in the MgB_2 lattice. Apart from the carbon doping method, a new trial related to the state of the boron precursor has been carried out as well. The MgB_2 wires prepared from laboratory made nano-sized boron achieved the J_c of 105 $A \cdot cm^{-2}$ at 5 K and 4 T [14]. Bovone et al. [15] produced boron powder by magnesiothermic reduction of boron oxide in the lab, which proved to be an excellent precursor for MgB_2 wire manufacture independent of the applied technique. Furthermore, commercial carbon-coated amorphous boron powder brought along carbon doping and benefited the J_c of the synthesized MgB_2 bulks with or without Cu doping [16,17].

Considering the type of the original boron powder, isotopic boron has been adopted to determine the effect on the superconductivity and physical properties of MgB_2. The studies of both Bud'ko et al. [18] and Hinks et al. [19] indicated a difference of 1 K in transition temperature (T_c) for the un-doped MgB_2 made of ^{10}B and ^{11}B. Simonelli et al. [20] investigated the isotope effect on phonon spectra of MgB_2 with Al doping and suggested a difference in Raman shift for the two isotopic forms of MgB_2. Recently, Alarco et al. [21] extended the study to the effect of ^{10}B, ^{11}B and natural B (mixture of ^{10}B and ^{11}B) on the phonon frequencies, which exhibited a pronounced isotopic effect for the phonon modes. Compared with conventional Nb-based superconductors, MgB_2 features "low activation" and a much shorter decay time. Within 1 year, the dose rate of MgB_2 materials will be reduced to the hands-on maintenance level, which is desirable for a fusion reactor magnet system [4]. Additionally, because of the reaction $^{10}B + n \rightarrow {}^{7}Li + He$ (gas) under the heavy

irradiation condition, ^{10}B can no longer guarantee the stability of the MgB_2 superconducting magnet. ^{10}B isotope is transformed to ^{7}Li and He by the neutron irradiation, while ^{11}B isotope is stable against the neutron irradiation without nuclear transformation and can reduce nuclear heating from 2.58 to 0.13 W/cm3 [22].

By replacing ^{10}B with the isotope ^{11}B, $Mg^{11}B_2$ superconducting wires will be much more stable in a neutron irradiation environment due to the smaller neutron capture cross-section of ^{11}B [23]. Considering the abundant reserves of ^{11}B on Earth (20 wt % for 10B, 80 wt % for ^{11}B), the anticipated cost for extracting the isotope from natural boron is expected to be reduced during the chemical synthesis. $Mg^{11}B_2$ would be a promising candidate material as a lower field poloidal field and correction coil superconducting magnets in a fusion reactor (Fig. 5.1). In view of this, glycine-doped MgB_2 bulks are prepared from natural B (written as $^{10.8}B$) and ^{11}B in this study to improve the critical current density at high field region.

5.2. Experimental Details

Amorphous $^{10.8}B$ (93%–94% purity, 0.6–0.7 μm in size) or ^{11}B powder (amorphous, 99.2% in purity, about 5 μm in size, from Pavezyum Kimya, Istanbul, Turkey), Mg powder (99.5% purity, 100 μm in size), and glycine powder (99% purity) were mixed in the ratio of MgB_2 + 3 wt % Gly. After ground thoroughly in an agate mortar, the mixture was pressed into cylindrical pellets (5 mm diameter and 1.5 mm thickness) under a pressure of 5 MPa. The obtained pellets were then sintered in the differential thermal analysis apparatus (DSC 404C, Netzsch, Boston, MA, USA) at 800 °C for 0.5 h with a heating rate of 10 °C·min^{-1} and a cooling rate of 40 °C·min^{-1}. The whole process was accomplished under the protection of flowing high-purity Ar gas. The superconducting properties were measured on a superconducting quantum interference device (SQUID–VSM, Quantum Design, San Diego, CA, USA) after the sample was cut into a slab (4 × 2 × 1 mm^3). The corresponding J_c values were calculated from the width of magnetization hysteresis loops based on the Bean model $J_c = 20\Delta M/[a/(1 - a/3b)]$ [24], where M is the volume magnetization, ΔM is the difference in volume magnetization between the arms of the M–H loop, and a and b are the sample dimensions (a < b).

5.3. Results and Discussion

Analogous to the un-doped and the Gly-doped $Mg^{10.8}B_2$, the Gly-doped $Mg^{11}B_2$ is composed of MgB_2 as the main phase and MgO as the only impurity phase (Figure 5-2). Generally, doping from carbon sources results in the substitution of carbon for boron in the MgB_2 lattice. Substituted carbon atoms normally donate their additional valence electrons (compared to boron) to the σ conduction band, resulting in decreased carrier concentration by filling the holes and decreasing the superconducting gaps.

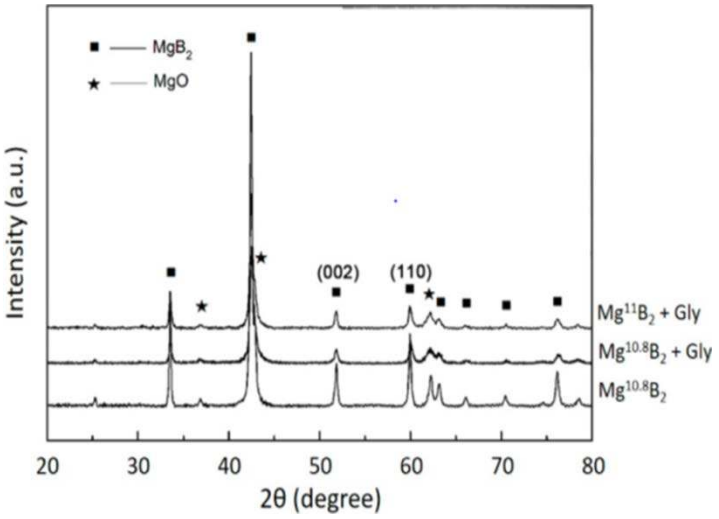

Figure 5-2. X–ray diffraction patterns for the un-doped $Mg^{10.8}B_2$, the Gly-doped $Mg^{10.8}B_2$, and the Gly-doped $Mg^{11}B_2$ samples.

This will reduce the number of holes at the top of the σ bands together with a reduction of the electronic density of states [25], and consequently the transition temperature T_c was supposed to decrease. Previous studies have stated that the MgB_2 samples showed a strong boron isotope effect, as the T_c for $Mg^{11}B_2$ decreased almost 1 K in contrast with the $Mg^{10}B_2$ sample [18,19]. However, the T_c for the Gly-doped $Mg^{11}B_2$ sample remained at the same level as the doped $Mg^{10.8}B_2$ sample shown in Figure 5-3.

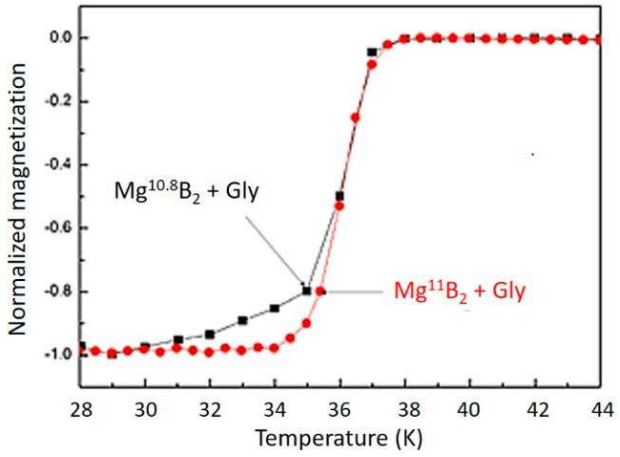

Figure 5-3. Temperature dependence of normalized magnetization for the Gly-doped $Mg^{10.8}B_2$ and the Gly-doped $Mg^{11}B_2$ samples.

From the viewpoint of the isotope effect, the increase of the phonon frequency is conductive to improve T_c, and the approach of the phonon and coulomb energies will lead to a decrease of T_c. As summarized by Knigavko [26], the T_c would remain stable when the two effects reached a balance in the Gly-doped $Mg^{11}B_2$ sample. The replaced carbon atoms likely originated from the reaction of

Mg and the decomposition product of glycine, $2Mg + CO_2 \rightarrow C + 2MgO$, with the impurity phase MgO generated. Contrary to the common position that the dielectric MgO occupied in most doping systems, i.e., at the grain boundary [27], the MgO particles in the Gly-doped $Mg^{11}B_2$ sample might be embedded within the MgB_2 grains in the nano-scale dimension. Besides, element mappings for Mg and O on an area with holes are shown in Figure 5-4(a)–(c). Combined with the distribution of Mg element, the MgO phase was believed to be dispersed homogeneously on the matrix rather than gathered in the hole, which implied good MgB_2 grain connectivity. A thermodynamic calculation has demonstrated that the MgO phase was formed prior to MgB_2, and the study on undoped $Mg^{11}B_2$ suggested that the ^{11}B accelerated the Mg-B solid-solid reaction below 650 °C [28]. Hence, the MgO particles were mostly included in the growing MgB_2 grains instead of aggregating at the boundary. The size and distribution of MgO allowed them to become effective pinning centers, and as a result, the Gly-doped sample had a significantly improved J_c performance at least twice larger than those of pure MgB_2 over the entire field at 20 K. The measured J_c -H characteristics of the un-doped and the Gly-doped samples at 20 K are illustrated in Figure 4d. A further improvement in J_c was observed in the Gly-doped $Mg^{11}B_2$ sample, even at the low field. The enhanced J_c should be attributed to the use of high-purity ^{11}B powder as well, in view that Gly-doped sample prepared from high-purity boron shows two times higher J_c than that from low-purity boron powder [29].

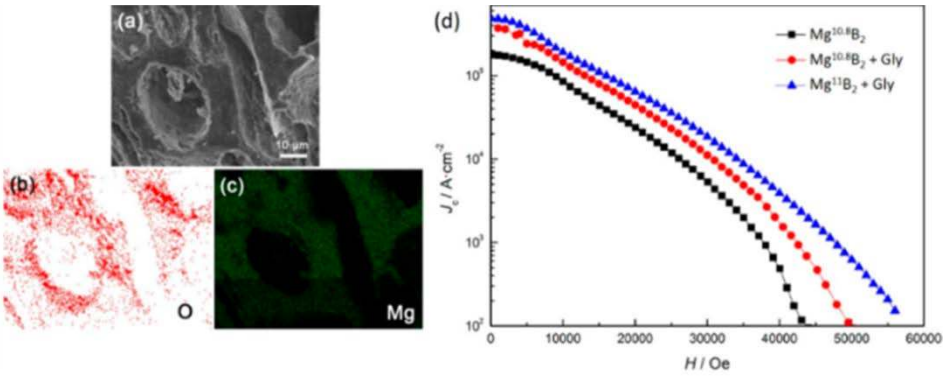

Figure 5-4. (a) Scanning electron microscopy (SEM) image; (b,c) corresponding element mappings of O and Mg for the Gly-doped $Mg^{11}B_2$ sample; and (d) Measured J_c-H characteristics at 20 K for the un-doped $Mg^{10.8}B_2$, the Gly-doped $Mg^{10.8}B_2$, and the Gly-doped $Mg^{11}B_2$ samples.

5.4. Conclusions

A glycine-doped $Mg^{11}B_2$ sample with layered grains was synthesized from isotopic ^{11}B powder. The glycine-doped $Mg^{11}B_2$ gives comparable critical current density and could be used for fusion reactors because of endurance against neutron irradiation. The results obtained in this work could guide the fabrication of $Mg^{11}B_2$ wires to be used as magnet coils in fusion reactor systems such as ITER-type tokamak magnets.

5.5. References

1. Mitchell, N.; Bessette, D.; Gallix, R.; Jong, C.; Knaster, J.; Libeyre, P.; Sborchia, C.; Simon, F. The ITER Magnet System. IEEE Trans. Appl. Supercond. 18, 435–440, 2008.

2. Salpietro, E. Status of the ITER magnets. Supercond. Sci. Technol. 19, S84., 2006.

3. Devred, A.; Backbier, I.; Bessette, D.; Bevillard, G.; Gardner, M.; Jong, C.; Lillaz, F.; Mitchell, N.; Romano, G.; Vostner, A. Challenges and status of ITER conductor production. Supercond. Sci. Technol. 27, 044001, 2014.

4. Noda, T.; Takeuchi, T.; Fujita, M. Induced activity of several candidate superconductor materials in a tokamak-type fusion reactor. J. Nucl. Mater. 329–333, 1590–1593, 2004.

5. Noda, T.; Maki, K.; Takeuchi, T.; Suzuki, H.; Araki, H.; Yang, W. Induced activity and damage of superconducting materials for a fusion reactor. Fusion Eng. Des. 81, 1033–1037, 2006.

6. Nagamatsu, J.; Nakagawa, N.; Muranak, T.; Zenitani, Y.; Akimitsu, J. Superconductivity at 39K in magnesium diboride. Nature 410, 63–64, 2001.

7. Finnemore, D.K.; Ostenson, J.E.; Bud'ko, S.L.; Lapertot, G.; Canfield, P.C. Thermodynamic and transport properties of superconducting (MgB_2)-B-10. Phys. Rev. Lett. 86, 2420, 2001.

8. Hossain, M.S.A.; Senatore, C.; Flukiger, R.; Rindfleisch, M.A.; Tomsic, M.J.; Kim, J.H.; Dou, S.X. The enhancement of *Jc* and Birr of in-situ MgB_2 wires and tapes alloyed with $C_4H_6O_5$ (malic acid) after cold high pressure densification. Supercond. Sci. Technol. 22, 095004, 2009.

9. De Silva, K.S.B.; Xu, X.; Gambir, S.; Wong, D.C.; Li, W.; Hu, Q.Y. Effect of sintering temperature on the superconducting properties of graphene doped MgB_2. IEEE Trans. Appl. Supercond. 23, 7100604, 2013.

10. Ye, S.J.; Matsumoto, A.; Zhang, Y.C.; Kumakura, H. Strong enhancement of high-field critical current properties and irreversibility field of MgB_2 superconducting wires by coronene active carbon source addition via the new B powder carbon-coating method. Supercond. Sci. Technol. 27, 085012, 2014.

11. Hossain, M.S.A.; Kim, J.H.; Wang, X.L.; Xu, X.; Peleckis, G.; Dou, S.X. Enhancement of flux pinning in a MgB_2 superconductor doped with tartaric acid. Supercond. Sci. Technol. 20, 112, 2007.

12. Cai, Q.; Ma, Z.; Liu, Y.; Yu, L. Enhancement of critical current density in glycine-doped MgB_2 bulks. Mater. Chem. Phys.136, 778, 2012.

13. Cai, Q.; Liu, Y.; Ma, Z.; Yu, L. Significant enhancement of critical current density in Gly-doped MgB_2 bulk by tailoring the formation of MgO. Scr. Mater. 67, 92, 2012.

14. Vignolo, M.; Bovone, G.; Matera, D.; Nardelli, D.; Bernini, C.; Siri, A.S. Nano-sized boron synthesis process towards the large scale production. Chem. Eng. J. 256, 32, 2014.

15. Bovone, G.; Matera, D.; Bernini, C.; Magi, E.; Vignolo, M. Manufacturing process influence on superconducting properties of MgB_2 wires prepared using laboratory made boron. Supercond. Sci. Technol. 28, 065006, 2015.

16. Barua, S.; Hossain, A.; Shahriar, M.; Ma, Z. Superior critical current density obtained in MgB_2 bulks through low-cost carbon-encapsulated boron powder. Scr. Mater. 104, 37, 2015.

17. Liu, Y.; Lan, F.; Ma, Z.; Chen, N.; Li, H.; Barua, S.; Patel, D.; Shahriar, M.; Hossain, A.; Acar, S. Significantly enhanced critical current density in nano- MgB_2 grains rapidly formed at low temperature with homogeneous carbon doping. Supercond. Sci. Technol. 28, 55005, 2015.

18. Bud'ko, S.L.; Lapertot, G.; Petrovic, C.; Cunningham, C.E.; Anderson, N.; Canfield, P.C. Boron isotope effect in superconducting MgB_2. Phys. Rev. Lett. 86, 1877, 2001.

19. Hinks, D.; Claus, H.; Jorgensen, J. The complex nature of superconductivity in MgB_2 as revealed by the reduced total isotope effect. Nature 411, 457, 2001.

20. Simonelli, L.; Palmisano, V.; Fratini, M.; Filippi, M.; Parisiad es, P.; Lampakis, D.; Liarokapis, E.; Bianconi, A. Isotope effect on the E-2g phonon and mesoscopic phase seperation near the electronic topological transition in $Mg_{1-x}Al_xB_2$. Phys. Rev. B 80, 014520, 2009.

21. Alarco, J.A.; Talbot, P.C.; Mackinnon, I.D. Coherent phonon decay and the boron isotope effect for MgB_2. Phys. Chem. Chem. Phys. 16, 25386, 2014.

22. Hishinuma, Y.; Kikuchi, A.; Shimada, Y.; Kashiwai, T.; Hata, S.; Yamada, S.; Muroga, T.; Sagara, A. Development of MgB_2 superconducting wires for the low activation superconducting magnet system operated around core D-T plasma. Fusion Eng. Des. 98–99, 1076, 2015.

23. Mooring, F.P.; Monahan, J.E.; Huddleston, C.M. Neutron cross sections of boron isotopes for energies between 10 and 100 KeV. Nucl. Phys. 82, 16–32, 1966.

24. Bean, C.P. Magnetization of hard superconductors. Phys. Rev. Lett. 8, 250, 1962.

25. Kortus, J.; Dolgov, O.V.; Kremer, R.K.; Golubov, A.A. Band filling and interband scattering effects in MgB_2: Carbon versus aluminium doping. Phys. Rev. Lett. 94, 027002, 2005.

26. Knigavko, A.; Marsiglio, F. Constraints from T_c and the isotope effect in MgB_2. Phys. Rev. B 64, 172513, 2001.

27. Ma, Z.Q.; Liu, Y.C.; Gao, Z.M. The synthesis and grain connectivity of lamellar MgB_2 grains by Cu-activated sintering at low temperature. Scr. Mater. 63, 399–402, 2010.

28. Cheng, F.; Liu, Y.; Ma, Z.; Li, H.; Hossain, M.S.A. Superior Critical current density obtained in $Mg^{11}B_2$ low activation superconductor by using reactive amorphous ^{11}B and optimizing sintering temperature. J. Alloys Compd.650, 508, 2015.

29. Wu, F.; Cai, Q. Comparison of critical current density in undoped, glycine doped and Cu-and-glycine- co-doped MgB_2 synthesized from nm-Boron and μm-Boron. J. Supercond. Nov. Magn. 27, 2023–2027, 2014.

Chapter 6

Improvement in the Transport J_c and Microstructure of the Isotopic $Mg^{11}B_2$ Monofilament Wires by Optimizing Sintering Temperature

6.1. Introduction

Fusion power is one of the most promising candidate energy sources that may solve global energy problems, considering its safer and greener merits compared with the conventional mineral energy sources. In the world-class International Thermonuclear Experimental Reactor (ITER) fusion energy project, the superconducting magnet system serves as a key determinant. A high and steady magnetic field needs to be produced to confine the deuterium (D)–tritium (T) burning plasma inside the ITER tokamak nuclear fusion reactor. According to the previous ITER plan, hundreds of tons of superconducting magnets made from NbTi and Nb_3Sn will be fabricated to assemble 18 Nb_3Sn toroidal field (TF) coils, a 6-module Nb_3Sn central solenoid (CS) coil, 6 Nb-Ti poloidal field (PF) coils, and 9 pairs of Nb-Ti correction coils (CC) [1, 2]. There is one major drawback, however, for the application of Nb-based superconductors in this project. After irradiation, ^{93}Nb will be transformed into the long-lived nuclide ^{94}Nb with a half-life of about 20,000 years [3, 4]. Hence, before irradiated Nb-based alloys are safe to be recycled, tens of thousands of years are required for them to "cool down", and meanwhile, thicker shielding is necessary for long-term operation. For the convenience of radioactive waste treatment and environmental protection, the radioactivation properties of superconducting components within the fusion reactor should be taken into account. Compared with conventional Nb-based superconductors, MgB_2 features "low activation" and a much shorter decay time. Within 1 year, the dose rate of MgB_2 materials will be reduced to the hands-on maintenance level, which is considered as desirable for a fusion reactor magnet system [3]. Additionally, because of the reaction $^{10}B + n \rightarrow {}^{7}Li + He$ (gas) under the heavy irradiation condition, ^{10}B can no longer guarantee the stability of the MgB_2 superconducting magnet. By replacing ^{10}B with the isotope ^{11}B, $Mg^{11}B_2$ superconducting wires will be much more stable in a neutron irradiation environment due to the smaller neutron capture cross-section of ^{11}B [5]. Considering the abundant reserves of ^{11}B on Earth (20 wt% for ^{10}B, 80 wt% for ^{11}B), the anticipated cost for extracting the isotope from natural boron is expected to be decreased during the chemical synthesis.

The superconductivity of MgB_2 was discovered in 2001 [6]. It is well-known for its simple binary chemical composition and much higher critical transition temperature (T_c) of 39 K than that of NbTi at 9.3 K. In order to operate Nb-based low-temperature superconductors, the core of the magnet needs to be cooled down to 4 K. The only eligible cryogen is liquid helium, which is extremely expensive, not always available on hand, and very difficult to handle. In the case of MgB_2, a working temperature as high as 20 K is low enough to achieve acceptable performance.

Remarkably, the operating cost is expected to be cut by over 50% by substituting cryocooler-cooled MgB_2 materials for liquid-helium-cooled Nb-based superconductors. Furthermore, the fabrication cost of MgB_2 superconducting wire itself ($2.64/kA·m) is less than 1/3 of that of Nb_3Sn wire ($9/kA·m). Therefore, due to the advantages of cost-effectiveness, lower radioactivation, and the shorter decay time of isotopic $Mg^{11}B_2$, fundamental research on $Mg^{11}B_2$ superconducting wires will be valuable for improving the efficiency of practical application in high-irradiation environments such as fusion reactors.

$Mg^{11}B_2$ wires using isotopically pure ^{11}B powder always show lower critical current density (J_c) values, however, than the wires fabricated with natural boron powder. According to previous work [7, 8], this lower J_c is a result of the increased amount of non-reactive precursor, which decreases the superconducting fraction. On the other hand, inter-grain connectivity is considered another crucial factor in the current-carrying capability of $Mg^{11}B_2$ superconducting wires [9–11]. In this work, with the aim of further improving J_c in $Mg^{11}B_2$ wires, the evolution of the microstructure and superconducting performance in $Mg^{11}B_2$ wires sintered at different temperatures was investigated in detail. The influence of both the superconducting fraction and the inter-grain connectivity on the J_c performance is discussed. We optimized the temperature of the heat-treatment at which the best transport performance can be obtained. Surprisingly, in the case of $Mg^{11}B_2$ wire sintered at high temperature, the transport J_c vanished, although magnetic J_c was still detected. According to detailed microstructure observations, this could be ascribed to the formation of a unique microstructure that was only obtained in the sample sintered at excessively high temperature. This kind of microstructure leads to significant deterioration in inter-grain connectivity and ultimately, poor transport current performance.

6.2. Experimental Details

The standard in-situ powder-in-tube (PIT) procedure was applied to all the samples. The starting materials for the $Mg^{11}B_2$ wire consisted of ^{11}B amorphous powder (from Pavezyum Kimya, Turkey, Moissan method [12], 95.5%) and magnesium powder (100–200 mesh, 99%). The isotopic purity and particle size with respect to the ^{11}B enriched boron powder was > 99.5% and 840 nm, respectively. After mixing the precursor powders, the mixture was tightly packed into Nb/Monel tubes with 10 mm outer diameter and 6 mm inner diameter. The composite wire was swaged and drawn to a final outer diameter of 1.08 mm. Then, the fabricated $Mg^{11}B_2$ wires were sintered at different temperatures ranging from 700 °C, 750 °C, 770 °C, and 800 °C for 60 min (ramp rate: 5 °C/min) under high purity flowing argon gas. Finally, the samples were furnace-cooled to room temperature. The transport critical current (I_c) measurements were carried out by using an American Magnetics superconducting magnet with DC current (with the upper limit of the current source 200 A) under possible magnetic field up to 15 T, with the standard four-probe method and the criterion of 1 μ V/cm. The critical current density J_c was calculated by dividing I_c by the cross-section of the $Mg^{11}B_2$ core, which was examined with an optical microscope (Leica M205A). Scanning electron microscopy (SEM, JEOL JSM-6490LV & JEOL JSM-7500) was

employed to observe the microstructure under different magnifications. X-ray diffraction (XRD) θ–2θ scans (GBC-MMA) were used to identify the phase composition. Measurements of electrical resistivity and magnetic moment were conducted in a 9 T Physical Properties Measurement System (PPMS, Quantum Design). In case of XRD, SEM, and PPMS measurements, the outer sheaths of the $Mg^{11}B_2$/Nb/Monel wires were removed for better data accuracy.

6.3. Results and Discussion

Typical transport J_c - B performances of all four wires sintered at different temperatures are shown in Figure 6-1. For reference purposes, transport J_c data of for the multi-filament $Mg^{11}B_2$/Ta/Cu wire reported by Hishinuma [7] is also plotted in the figure. It should be noted that our best monofilament $Mg^{11}B_2$ wire shows comparable transport J_c performance to the multifilament wire fabricated by the National Institute for Fusion Science (NIFS) [7]. This result is considered as a big breakthrough, and it strongly supports the feasibility of replacing commercial NbTi by high-performance $Mg^{11}B_2$ wires in highly radioactive fusion reactors. In our $Mg^{11}B_2$ wires, 750 °C is the optimized temperature for heat treatment. The corresponding wire possesses a J_c value near 2 × 10^4 A/cm^2 at 4.2 K and 5 T. Slight J_c degradation is observed in the wire treated at temperatures deviating from 750 °C. Surprisingly, no transport current was detected in the wire treated at 800 °C. For verification, five attempts at measurement were carried out on three batches of wires produced under the same sintering conditions. Ultimately, none of them gave detectable transport current data. It is speculated that some unexpected qualitative change inside the wire might occur once the heating temperature reaches a certain level. This should probably be attributed to a unique property of the ^{11}B starting powder. It is believed that investigations of the phase composition, microstructure, and inter-grain connectivity will give an explanation for this abnormal phenomenon.

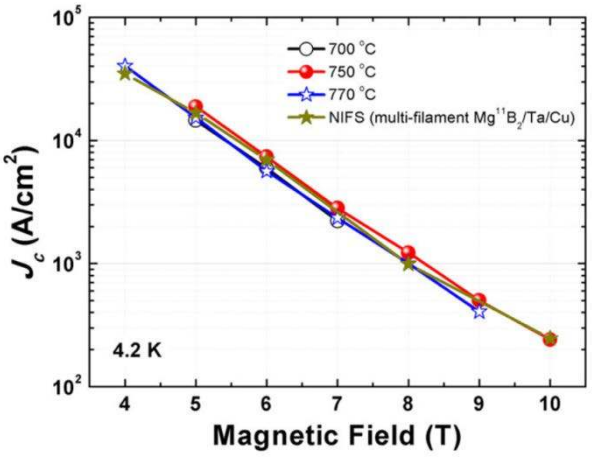

Figure 6-1. Transport J_c - B performance at 4.2 K of $Mg^{11}B_2$ wires using amorphous ^{11}B isotope as the boron source. Results from NIFS are also plotted for reference. No transport I_c was detected in the wire treated at 800 °C.

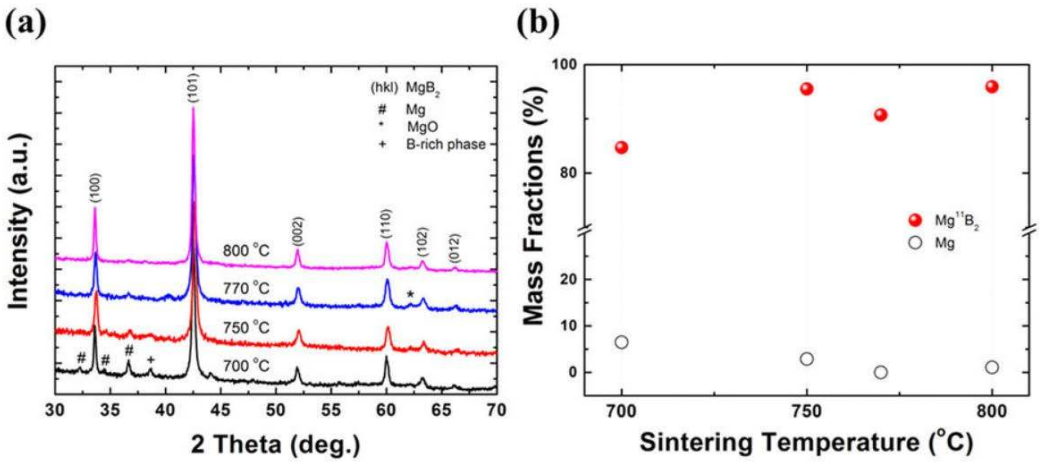

Figure 6-2. (a) XRD θ–2θ patterns of all $Mg^{11}B_2$ wires sintered at different temperatures. The numbered labels (*hkl*) represent $Mg^{11}B_2$ reflections. The pound sign (hashtag) stands for unreacted Mg. A small amount of B-rich phase (with its peak marked by the plus sign) is detected only in samples sintered at 700 °C. (b) Mass fractions, obtained from Rietveld refinement, of $Mg^{11}B_2$ and Mg as functions of the different sintering temperatures.

To confirm the phase composition, $Mg^{11}B_2$ cores were removed from their outer sheaths and finely ground as XRD specimens. In Figure 6-2(a), the main peaks indexed as $Mg^{11}B_2$ can be observed in all spectra, indicating that the temperature is high enough to permit the formation of $Mg^{11}B_2$ phase. Very little oxidation was detected, according to the negligible MgO peak. Un-reacted Mg and ^{11}B-rich phase are found in the wire sintered at relatively low temperature. Apparently, it is very hard for Mg to completely diffuse into boron particles, if the sintering temperature is not high enough. A diminishing gradient of Mg concentration exists along the radial direction of the boron particle. As a result, $Mg^{11}B_2$ phase can only be formed on the outer layers of boron particles. The rest of the Mg will either stay in the elemental state (un-reacted Mg) or participate in other secondary reactions. Hence, ^{11}B-rich phase is prone to form in this case, which can be deduced from the Mg-B phase diagram [13]. The presence of those impurities (un-reacted Mg and ^{11}B-rich phase) will reduce the fraction of superconducting phase, which is crucial for the final performance of superconductors. It has to be pointed out that the chemical activity of ^{11}B is lower in comparison with natural B due to the isotope kinetic effect [14]. This might explain why 700 °C is not high enough for the complete reaction in this work. Figure 6-2(b) shows the mass fractions of $Mg^{11}B_2$ phase in the wires as a function of sintering temperature. The mass fractions were calculated by using Rietveld refinement. The smallest $Mg^{11}B_2$ fraction, as low as 84.7%, is found in the wire treated at 700 °C. This is mainly due to the presence of impurities, as reflected by the XRD results. Furthermore, the degradation in transport J_c performance also confirms its relatively poor superconductivity (see Figure 6-1). With increasing sintering temperature, un-reacted Mg peaks become smaller and almost disappear. Correspondingly, the mass fractions of $Mg^{11}B_2$ phase in the rest of the wires all remain at a high level (> 90%). Since

the crystallization of $Mg^{11}B_2$ phase is confirmed to be good in the $Mg^{11}B_2$ wire sintered at 800 °C, while its mass fraction of superconducting phase is also satisfactory, the observed abrupt disappearance of transport current in the wire sintered at 800 °C is related to neither the phase composition nor a low superconducting fraction.

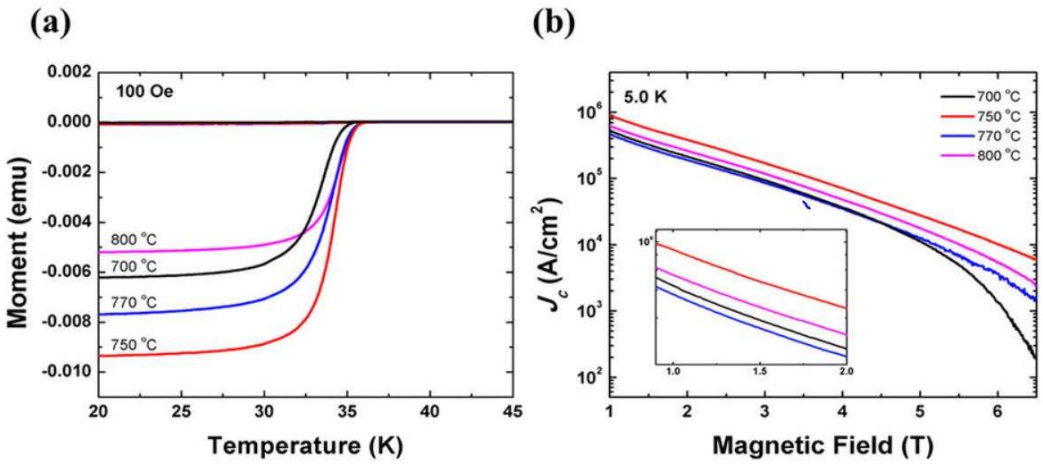

Figure 6-3. (a) Temperature dependence of the ZFC and FC dc magnetization measured in a field of 100 Oe. (b) Field dependence of the magnetic J_c at 5.0 K on the logarithmic scale (with the inset showing an enlargement of the J_c (H) at low fields) for all samples.

Figure 6-3(a) shows the zero-field-cooled (ZFC) and field-cooled (FC) demagnetization results as functions of the sintering temperature for all four samples. H = 100 Oe was applied in this measurement. A clear normal-superconducting transition was observed in all samples, including the wire sintered at 800 °C, which did not show any current value in the transport measurements. The magnetic J_c (H) of the samples was estimated at 5 K based on the magnetization hysteresis loops and the Bean critical state model. Generally, the formula for a rectangular shaped sample is: $J_c = 20(\Delta M/V)/[a(1- a/3b)]$, where $\Delta M = [M(+) - M(-)]$ is the difference between the upper and lower branches of the M(H) loop, V is the volume, and a and b (a < b) are the length and width of the cross-section which is perpendicular to the direction of the applied magnetic field [15]. In our case, the $Mg^{11}B_2$ cores are cylindrical in shape. So, the formula can be simplified to $J_c = 30(\Delta M/V)/d$, where d is the diameter of the circular cross-sectional area [16, 17]. According to the calculations, the magnetic J_c (H) results at 5.0 K are shown in Figure 6-3(b). The wire sintered at 750 °C shows the best magnetic J_c (H) performance throughout the entire range of fields, which is consistent with the transport J_c results shown in Figure 6-1. Some differences can be found between the values of magnetic J_c and transport J_c. Other than measurement deviation, the intrinsic distinction between the magnetic J_c signal and the transport J_c signal also needs to be taken into consideration. Generally, due to the existence of negative structures such as porosity and cracks, not all the MgB_2 in a sample is capable of passing transport current. Inter- or intra-grain connectivity should always be considered when dealing with transport performance. On the contrary, as long as they possess superconductivity, all the MgB_2 fragments will contribute to the

magnetic J_c. It should be noted that the magnetic J_c was detected and showed good performance in the wire sintered at 800 °C. This means that the $Mg^{11}B_2$ superconducting phase in the wire was not badly damaged by the high sintering temperature. Hence, after ruling out the effects of inferior superconducting phase, it can be speculated that the transport current in the wire sintered at 800 °C disappeared as a result of a problem with inter-grain connectivity. A high sintering temperature might introduce some defects and significantly destroy the connection between $Mg^{11}B_2$ superconducting grains.

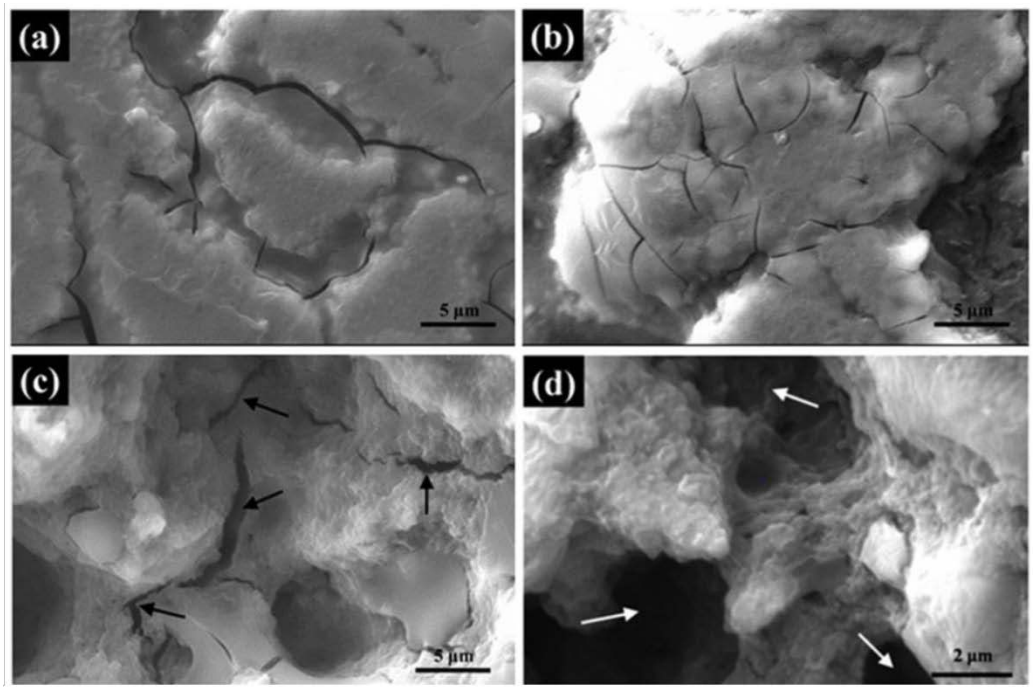

Figure 6-4. SEM micrographs of cross-sections of $Mg^{11}B_2$ wires sintered at (a) 700 °C, (b) 750 °C, and (c) 800 °C. Evolution of the surface morphology is clearly shown. Black arrows indicate big cracks. (d) SEM image of the wire sintered at 800 °C under higher magnification. White arrows indicate porous structure in the sample sintered at 800 °C.

It is estimated that the vanishing of transport current in the $Mg^{11}B_2$ wire is caused by the severe deterioration of inter-grain connectivity, which can be visually confirmed by SEM micrographs. The low-magnification SEM images of the cross-sections of $Mg^{11}B_2$ wires sintered at 700 °C, 750 °C and 800 °C are presented in Figure 6-4(a–c). Obvious evolution of the surface morphology is exhibited with increasing temperature. In the wire treated at 700 °C, it was already proved by the XRD results that the Mg had partially reacted with the boron. As the particle size of the Mg powder is much bigger than for the boron powder, un-reacted Mg melted and smoothly covered the $Mg^{11}B_2$ grains. Therefore, the morphology of this sample was fairly plain and incompact. A dense surface is observed in Figure 6-4(b) on the optimal sample sintered at 750 °C, indicating complete reaction and good inter-grain connectivity. This is consistent with the J_c - B and XRD results discussed above. Once the sintering temperature reached 800 °C, big cracks (marked by

black arrows) were observed, as shown in Figure 6-4(c). They are much bigger than the normal microcracks in other samples. Note that most of the big cracks are connected with each other. This feature is considered to be highly detrimental to the inter-grain connectivity. The resultant superconducting fragments are isolated from each other, and eventually, very little current can pass through the entire wire, which will significantly reduce the transport performance. On further increasing the magnification, porous structure is found in the same sample (marked by white arrows in Figure 6-4(d)). When the wire was heat-treated at 800 °C, both the grain size and the mobility of the $Mg^{11}B_2$ grains were increased. The separate grains are prone to aggregate with each other, leaving plenty of voids in the morphology. Consequently, the effective current capacity is sharply reduced with the emergence of the porous structure. This is considered to be another barrier to obtaining high transport current in $Mg^{11}B_2$ wires.

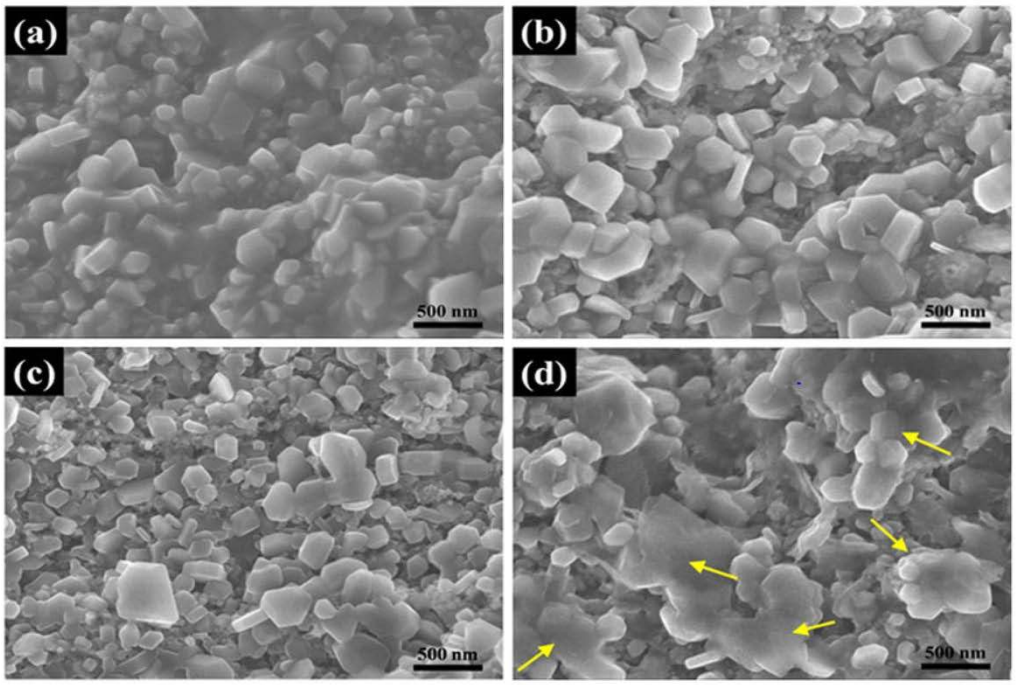

Figure 6-5. High-resolution SEM micrographs of longitudinal sections of $Mg^{11}B_2$ wires sintered at (a) 700 °C, (b) 750 °C, (c) 770 °C, and (d) 800 °C. The shapes of grains can be easily distinguished. The yellow arrows in (d) indicate clusters composed of multiple $Mg^{11}B_2$ grains.

In addition, this kind of microstructure with abundant voids can be more brittle and thus be more prone to fracture and form big microcracks (see Figure 6-4(c)) resulting from heat stress during the furnace-cooling process from high temperature to room temperature. High-resolution SEM was employed to investigate the details of the crystalline structure in the four $Mg^{11}B_2$, wires, and the results are presented in Figure 6-5. In the sample with the lowest sintering temperature, the crystalline grains have a wide range of sizes, and all of them are dispersed in a melted matrix, as shown in Figure 6-5(a). Referring to the XRD results above, the melted matrix is un-reacted Mg, which cannot be fully reacted with B at a relatively low temperature. This is strong evidence for

the smaller mass fraction of $Mg^{11}B_2$ phase and lower transport performance in this sample. In the wires sintered at higher temperature, the amount of un-reacted Mg is greatly reduced, and the $Mg^{11}B_2$ crystalline grains keep growing and form typical hexagonal shapes, which can be observed in Figure 6-5(b,c). Figure 6-5(d) shows the morphology of the wire sintered at 800 °C, in which some grains abnormally grow, and abundant big clusters are found. These clusters are formed by the localized aggregation of $Mg^{11}B_2$ grains at the relatively high heat-treatment temperature. This phenomenon further increases the porosity on the macroscale and significantly reduces the effective superconducting fraction for transporting current. As a result, the inter-grain connectivity is badly degraded. Combining these results with the low-magnification SEM images, it is thus concluded that the vanishing of transport current in the $Mg^{11}B_2$ sintered at high temperature should be attributed to the depression of inter-grain connectivity in the wire that is caused by the big microcracks and high porosity.

6.4. Conclusions

The effects of sintering temperature on the superconducting performance and morphology of $Mg^{11}B_2$ monofilament wires made from isotopically pure boron powder were investigated in this work. It was found that increasing the sintering temperature led to the evolution of microstructure and characteristic changes in the transport current capacity. Un-reacted Mg and B-rich phase existed in the wire sintered at low temperature. The $Mg^{11}B_2$ fraction, as well as the transport performance, was reduced because of the un-reacted Mg and B-rich phase impurities. With increasing sintering temperature, better phase composition and crystallinity were obtained. The best transport J_c = 2 × 104 A/cm^2 was reached at 4.2 K and 5 T in the $Mg^{11}B_2$ wire sintered at 750 °C. It should be noted that although high magnetic J_c was detected in the wire sintered at 800 °C, the transport current was totally absent. The evolution of the morphology could be clearly seen in the wires corresponding to different sintering temperatures. Due to the abnormal growth and high mobility of $Mg^{11}B_2$ grains at relatively high ambient temperature, numerous big microcracks, voids, and $Mg^{11}B_2$ clusters formed in the wire sintered at 800 °C. As a result, the inter-grain connectivity was significantly suppressed, resulting in the inferior transport performance. The results obtained in our work can be a constructive guide for fabricating $Mg^{11}B_2$ wires to be used as magnet coils in fusion reactor systems such as ITER-type tokamak magnets.

6.5. References

1. Mitchell, N. et al. The ITER Magnet System. IEEE Trans. Appl. Supercond. 18, 435–440, 2008.

2. Devred, A. et al. Challenges and status of ITER conductor production. Supercond. Sci. Technol. 27, 044001, 2014.

3. Noda, T., Takeuchi, T. & Fujita, M. Induced activity of several candidate superconductor materials in a tokamak-type fusion reactor. J. Nucl. Mater. 329–333, 1590–1593, 2004.

4. Noda, T. et al. Induced activity and damage of superconducting materials for a fusion reactor. Fusion Eng. Des. 81, 1033–1037, 2006.

5. Mooring, F. P., Monahan, J. E. & Huddleston, C. M. Neutron cross sections of the boron isotopes for energies between 10 and 500 keV. Nucl. Phys. 82, 16–32, 1966.

6. Nagamatsu, J., Nakagawa, N., Muranak, T., Zenitani, Y. & Akimitsu, J. Superconductivity at 39 K in magnesium diboride. Nature 410, 63–64, 2001.

7. Hishinuma, Y. et al. Development of MgB_2 superconducting wire for the low activation superconducting magnet system operated around core D-T plasma. Fusion Eng. Des. 98–99, 1076–1080, 2015.

8. Hishinuma, Y. et al. Effect of boron particle size on microstructure and superconducting properties of in-situ Cu addition MgB_2 multifilamentary wire. J. Phys. Conf. Ser. 507, 022009, 2014.

9. Glowacki, B. A. et al. Superconductivity of powder-in-tube MgB_2 wires. Supercond. Sci. Technol. 14, 193–199 , 2001.

10. Matsumoto, A., Kumakura, H., Kitaguchi, H., Fujii, H. & Togano, K. The annealing effects of MgB_2 superconducting tapes. Physica C 382, 207–212, 2002.

11. Serquis, A. et al. Microstructure and high critical current of powder-in-tube MgB_2. Appl. Phys. Lett. 82, 1754, 2003.

12. Markovskii, L. Y. Chemistry of magnesiothermal preparation of boron. Electron. Technol. 3, 95–102, 1970.

13. Massalski, T. B., Okamoto, H., Subramanian P. R. & Kacprzak, L. Binary Alloy Phase Diagrams. ASM International, 1990.

14. Chkhartishvili, L. Isotopic effects of boron. Trends Inorg. Chem. 11, 105–167, 2009.

15. Bean, C. P. Magnetization of high-field superconductors. Rev. Mod. Phys. 36, 31–39, 1964.

16. Fietz, W. A. & Webb, W. W. Hysteresis in superconducting alloys—temperature and field dependence of dislocation pinning in niobium alloys. Phys. Rev. 178, 657, 1969.

17. Takano, Y., Oguro, N., Kaieda Y. & Togano, K. Superconducting properties of combustion synthesized MgB_2. Physica C 412–414, 125–129, 2004.

Chapter 7

Evaluation of residual stress and texture in isotope based $Mg^{11}B_2$ superconductor using neutron diffraction

7.1. Introduction

While the current workhorse superconductors for the International Thermonuclear Experimental Reactor (ITER) are low-temperature NbTi and Nb_3Sn superconductors [1-3], MgB_2 shows electromagnetic performance superior to that of NbTi: it has lower induced radioactivity [4, 5], higher efficiency of the cryogenic reactor system [6-8], and a much higher transition temperature (T_c) [9-10]. Furthermore, the field performance, in terms of its transport critical current density (J_c) and upper critical field (B_{c2}), is close to that of NbTi superconductor [11-13]. Thus, MgB_2 is possibly a viable candidate to replace NbTi superconductors in the poloidal field (PF) coils and correction coils (CC) for the next-generation fusion reactors. Based on the analysis reported by Devred et al. and Hossain et al. of the conductor development and performance criteria for the ITER project, the critical current capacity of MgB_2 cables clearly fulfils the requirements for use in the PF and CC magnets, even at 20 K, in the ITER fusion reactor [13, 14]. The use of conduction-cooled low-cost MgB_2 at 20 K in PF and CC magnets to replace NbTi will make the next generation fusion reactor much more cost effective. MgB_2 wire filament is brittle after the heat treatment, and given the strain limit criterion of 0.2% for the magnet design, the maximum strain limit is well below 0.2% to provide a factor of two safety margin [15]. Despite the prospects for the use of MgB_2 as a fusion reactor superconducting material, many technological issues need to be resolved, and the current work aims to report the progress in this direction.

The critical point in reactor application is the use of boron-11 isotope enriched powder for the fabrication of the MgB_2 superconductor. Natural boron has 19.78 wt% boron-10 (^{10}B) and 80.22 wt% boron-11 (^{11}B) [16-18]. ^{10}B is well known as a neutron absorption material with a large nuclear reaction cross-section, leading to transformation into ^{7}Li and He via the (n, α) reaction [19-21]. In contrast, ^{11}B is stable in the presence of neutron irradiation without an (n, α) reaction and can reduce nuclear heating [22, 23]. Therefore, ^{11}B isotope based $Mg^{11}B_2$ superconductor is the most desirable, if not absolutely necessary, material for Tokamak type magnets in fusion reactors.

In recent ITER superconducting cable performance tests, damage to the superconducting filaments has been recognised as a significant issue [24]. It was demonstrated that the superconducting filaments in the cables are easily damaged when exposed to temperature and electromagnetic cycling, simulating ITER operational regimes, and that this microscale damage has a detrimental effect on superconducting properties. The root cause of the microscale damage is associated with electromagnetic (Lorentz) forces as well as thermally generated stresses due to cooling to cryogenic temperatures and residual stresses generated during the production process [25-28].

Therefore, it is essential to assess and, if possible, to control the stress and strain state of the filaments, both when it originates from the manufacturing process and when it occurs due to the operating conditions. This knowledge can be used to predict and, ideally, eliminate possible damage to the superconducting filaments. In this respect, the residual stress is not only a partial cause of the damage, but also a quantity that can be studied to assess the degree of microscale damage. In case of development of microscale damage, the residual stresses become relaxed to a certain degree, and this effect can be studied experimentally.

Knowledge of the residual stresses is also important for understanding the effects of applied stress/strain on the superconducting properties, i.e. the critical current (I_c), which have been experimentally observed multiple times in MgB_2 superconducting systems (Kitaguchi 2001, 2005; Katagiri 2005; Nishijima 2012) [29-32]. The residual stresses were measured successfully on several occasions for Nb_3Sn using neutron diffraction [33, 34], and this technique proved to be the most suitable for the powder-in-tube system due to its ability to penetrate through the sheath material. There are no published results on measurements of the residual stress in MgB_2 wires, however, presumably due to the fact that manufacturing ^{11}B isotope based $Mg^{11}B_2$ wires is a prerequisite for such neutron measurements. Nevertheless, it is conceptually clear that, depending on the sign and magnitude of the residual stress, the combined effect of the residual and applied stress/strain can be different.

From this point of view, understanding the stress/strain behaviour of the $Mg^{11}B_2$ wires and coils for the magnet system of a fusion reactor is a critical issue in terms of current-carrying capability. Direct stress/strain measurements on the $Mg^{11}B_2$ filaments in the wire are difficult, because the $Mg^{11}B_2$ filamentary region, for practical use, is covered with a Monel (Ni-Cu alloy) sheath and Nb barrier. A high penetration depth of radiation, such as in the form of neutrons or high-energy synchrotron X-rays, is required to measure residual stress and texture on the superconducting wire [35].

In this report, we used neutron diffraction for a full quantitative residual stress analysis of the constituents in ^{11}B isotope based $Mg^{11}B_2$ wires ($Mg^{11}B_2$), in correlation with the fabrication conditions and the transport critical current density (J_c), for the first time. This assessment is the first step on the way to optimising the properties and manufacturing conditions for $Mg^{11}B_2$ superconductor intended for magnets in fusion reactors, with the possibility of mitigating unwanted stress and strain inside the wire filaments.

7.2. Experimental Details

The wire samples were prepared by using the conventional in-situ powder-in-tube (PIT) method. The ^{11}B low crystalline powder (from Pavezyum Kimya, Turkey), which consists of amorphous and crystalline components, was sintered by the Moissan method [36] with 840 nm particle size and isotopic purity of 99.25 ± 0.01% of ^{11}B. Magnesium powder (100-200 mesh, 99% purity), a niobium barrier, and a Monel (Ni-Cu alloy) sheath tube were also used for the production of the $Mg^{11}B_2$ wire. This particular ^{11}B powder was chosen from a selection of several candidates on the

basis of precursor powder and wire product characterisation (e.g. the isotopic purity reported above was determined by means of neutron transmission experiments and accelerator mass-spectrometry), and a study giving the details will be published separately elsewhere. The tube was swaged and drawn to an outer diameter of 1.08 mm, and then the wires were subjected to heat treatment at 700°C, 750°C, and 800°C for 1 hour (ramp rate of 5°C/min) under a high purity argon gas atmosphere. Scanning electron microscopy (SEM, JEOL JSM-6490LV) and X-ray diffraction (XRD, GBC-MMA) were employed to observe the microstructure and the phase composition using sectioned wires. The core, $Mg^{11}B_2$ based ceramic, was extracted from the Nb-Monel sheath for the X-ray diffraction. The volume fractions of ^{11}B-rich phase, Mg, and MgO for $Mg^{11}B_2$ were obtained using the MAUD program based on the X-ray diffraction [37].

For neutron experiments, the individual $Mg^{11}B_2$ wires were cut into pieces ~5mm in length and bunched together to form bulk samples with approximate dimensions of 5×5×5 mm^3. Measurements of residual stress were performed on the niobium, $Mg^{11}B_2$, and Monel phases. The measurements of residual stress on the $Mg^{11}B_2$ wires were carried out using the KOWARI neutron diffractometer [38] at the Open Pool Australian Lightwater (OPAL) research reactor at the Australian Nuclear Science and Technology Organization (ANSTO). The $Mg^{11}B_2$ phase was measured in a 90° geometry using the wavelength λ = 1.5 Å for the $Mg^{11}B_2$ (211) reflection and gauge volume size of 4×4×4 mm^3. Two principal directions, transverse and axial, were measured with constant rotation of the samples around their axis for better averaging.

A specially prepared pure $Mg^{11}B_2$ cylindrical pellet sample (5 mm diameter, 3 mm height) was used to determine the unstressed lattice spacing, d_0. For the production of this pellet, a high temperature (HT) 800°C thermal regime was used to produce a uniform (no Monel sheath, no Nb barrier) and high purity sample to ensure the absence of macro- and microstresses.

The stress (σ) was calculated for the measured transverse and axial strains, $\varepsilon_t = (d_t - d_0)/d_0$ and $\varepsilon_a = (d_a - d_0)/d_0$, respectively, of the $Mg^{11}B_2$ (211) reflections in the corresponding directions using the (*hkl*)-dependent Young's modulus (E) and Poisson's ratio (ν) calculated from the single crystal elastic constants in the isotropic approximation, E (211) = 316.2 GPa, and ν (211) = 0.17. The two principal stress components, transverse and axial, were computed accordingly to the following relationship $\sigma_{a,t} = \frac{E}{1+\nu}\left\{\varepsilon_{a,t} + \frac{\nu}{1-2\nu}(\varepsilon_a + 2\varepsilon_t)\right\}$ adapted for the case of the cylindrical symmetry stress state from the general Hooke's law [39, 40].

To further study aspects of the anisotropic stress state, neutron texture measurements were performed on the wires, including three phases, $Mg^{11}B_2$, Monel sheath, and Nb barrier (only for the sample sintered at 700°C, since the other samples were essentially identical). Several representative pole figures were collected to judge the crystallographic isotropy/anisotropy using the same KOWARI diffractometer. We consider that the effect of crystallographic texture [41], which requires experimental determination, is three fold. First, it determines the anisotropy of the elastic and thermal properties (e.g. Young's modulus and the coefficient of thermal expansion), which is important for proper stress calculation procedures, as well as for stress evaluation if a finite element method (FEM) simulation is to be done. Second, if some crystallographic preferred orientation is found, it can shed light on the mechanism of MgB_2 phase formation and growth in

the sintering process. Third, for the polycrystalline layered superconductors, e.g. yttrium barium copper oxide (YBCO), with extremely high anisotropy of the critical current, the effect of texture is so high that the current can be practically destroyed due to unfavourable crystallographic alignment of the grains [42]. Although the single crystal anisotropy of MgB_2 is much less pronounced, control of the degree of preferred orientation is required.

7.3. Results and Discussion

The crystallographic anisotropy was quantified by neutron texture analysis, and the results are shown in Figure 7-1 as a set of representative pole figures for the three materials used in the wire, Monel, Nb, and $Mg^{11}B_2$ [41].

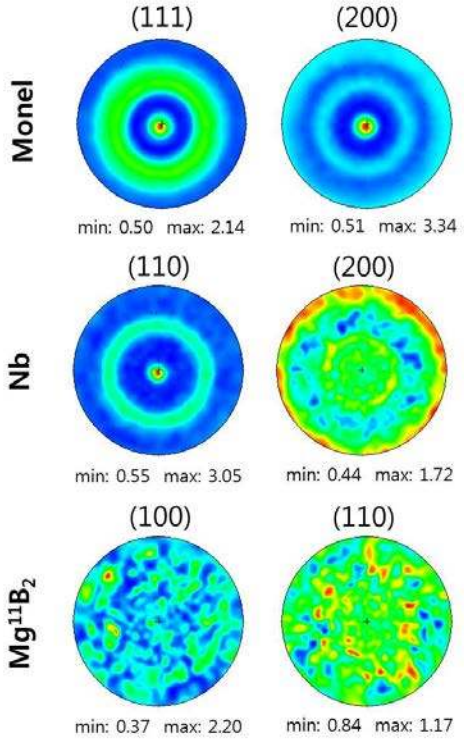

Figure 7-1. Pole figures of the phases in the $Mg^{11}B_2$ wire heat-treated at 700°C.

While there is strong anisotropy in the Monel-Nb sheath due to tensile plastic deformation during the swaging process, the crystal orientation of $Mg^{11}B_2$ has a random distribution (with only statistical oscillations visible in the pole figures of $Mg^{11}B_2$, while there is no pattern with preferred orientation). Thus $Mg^{11}B_2$ phase is crystallographically isotropic (with no preferred crystal orientation), and therefore, the elastic properties, which are important for the stress analysis of the system, have no anisotropy related to the crystalline preferred orientation. This does not eliminate the possibility of elastic anisotropy due to other micromechanical factors, however, e.g. microcracking determined, for example, by the deformation process. The results of the texture

analysis are to be used for macrostress calculations in the elastically anisotropic model of the sheath material and its interaction with the $Mg^{11}B_2$ interior, which is isotropic. The experimentally determined isotropy of the $Mg^{11}B_2$ interior is used here for model microstress calculations within the isotropic approximation. This trend is also observed in other samples and is the strong anisotropy of Monel and Nb due to plastic deformation while random distribution of $Mg^{11}B_2$ with isotropic phase.

Figure 7-2(a) shows that the cross-sectional microstructure of the wire consists of 49 vol.% Monel, 28 vol.% Nb, and 23 vol.% $Mg^{11}B_2$. Figure 7-2(b) presents the XRD patterns of the superconducting ceramic from the core of the $Mg^{11}B_2$ wires after sintering for one hour at 700°C, 750°C, and 800°C. While the major peaks are indexed as $Mg^{11}B_2$ phase, unreacted Mg, MgO, and ^{11}B-rich phase [43, 44] are present in the samples.

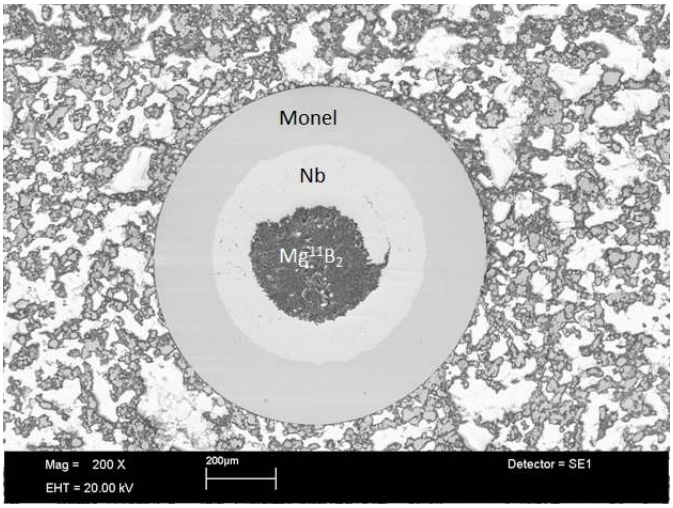

(a)

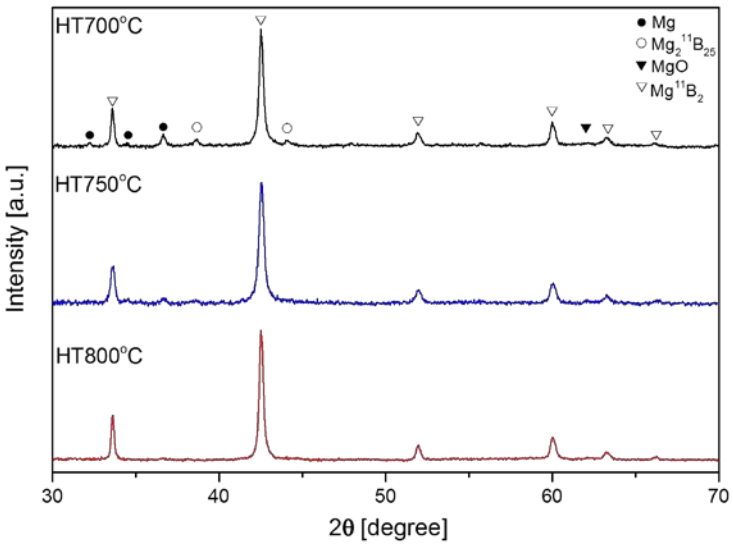

(b)

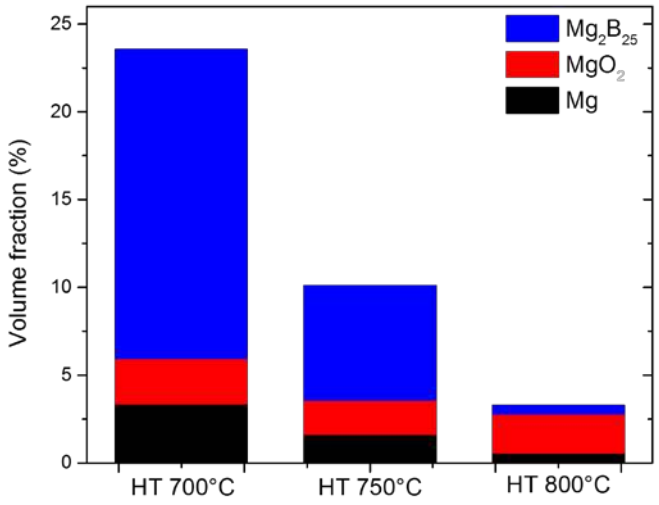

(c)

Figure 7-2. (a) The cross-sectional microstructure is shown in an SEM image of the Monel, Nb, and $Mg^{11}B_2$; (b) XRD patterns of the interior material of the $Mg^{11}B_2$ wires (Monel and Nb barrier are removed) after heat-treatment at 700°C, 750°C, and 800°C; (c) The volume fractions of boron-rich phase ($Mg_2{}^{11}B_{25}$), Mg, and MgO for $Mg^{11}B_2$ produced under different heat-treatment conditions.

Figure 7-2(c) shows the volume fractions of the secondary phases as functions of the sintering temperature. In the wires sintered at 700°C and 750°C, there are certain amounts of retained ^{11}B-rich phase and Mg phase, 10-20 vol.%, sufficient to produce significant and measurable microstresses. Further increasing the heat-treatment to 800°C diminished the volume fraction of the Mg and the ^{11}B rich phase to 0.37 % and 0.47%, respectively, resulting in the most fully reacted, most pure $Mg^{11}B_2$ superconductor.

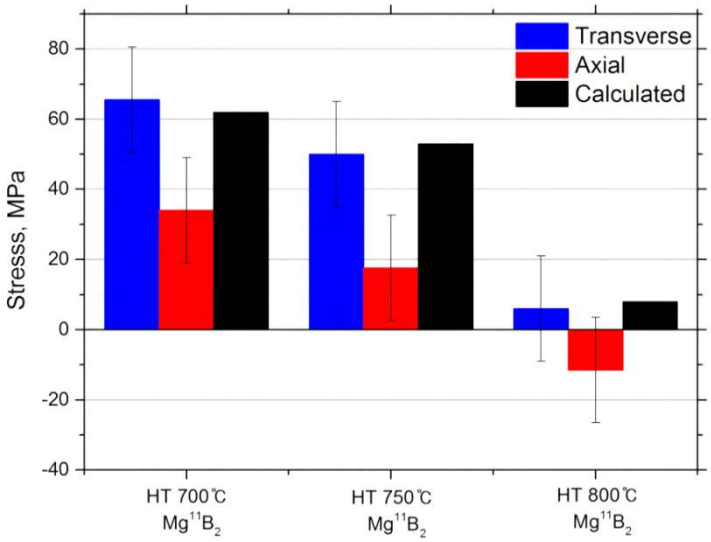

Figure 7-3. Residual stress in the $Mg^{11}B_2$ wires heat-treated at 700°C, 750°C, and 800°C.

Figure 7-3 shows the experimental results for the residual stress measurements of $Mg^{11}B_2$ wires in the transverse and the axial directions, with error bars showing the estimated uncertainty due to neutron counting statistics. The wires were characterised to have tensile stress of 66 ± 15 MPa (HT 700°C), 50 ± 15 MPa (HT 750°C), and 6 ± 15 MPa (HT 800°C) for the transverse component, which had a tendency to decrease with increasing heat-treatment temperature to almost negligible in the HT 800°C sample. The main contribution to the total stress was hydrostatic microstress (phase incompatibility stress) due to the interaction between the $Mg^{11}B_2$ matrix and the elastically harder unreacted ^{11}B rich phase upon cooling down from the sintering temperature [45]. This experimental result was corroborated by evaluating thermally generated phase stresses using a micromechanical model of the isotropic particulate composite based on the Eshelby inclusion formalism [46, 47]. The calculations were made accordingly to the evaluated volume fractions of the constituents ($Mg^{11}B_2$ as the primary phase, plus unreacted ^{11}B rich phase inclusions) and the thermal conditions for the composite formation in the Mg-B phase diagram [48]. A good numerical agreement with the experimental results was achieved. (Figure 7-3 combines the experimental and calculated results.) Thus, based on the XRD phase analysis results and the residual stress neutron measurements, it can be concluded that the higher heat-treatment temperature of 800°C is required for the full reaction of the ^{11}B rich and Mg phases to form $Mg^{11}B_2$, which ensures a low level of residual microstress.

In the axial direction, some compressive contribution to the total stress is present in addition to the hydrostatically-compressive microstress contribution discussed above, thus bringing the stress in the axial direction from tensile to less tensile, or even into compressive range, as in the 800°C heat-treated wire. This effect can be explained by the interaction between the Monel-Nb sheath and the $Mg^{11}B_2$, and is due to thermally generated macrostress. Taking account of the differences in the coefficient of thermal expansion (CTE) of the sheath and wire interior ($\Delta\alpha$) and the temperature drop from the sintering temperature to room temperature (ΔT), the thermal strain mismatch $\Delta\varepsilon = \Delta T \cdot \Delta\alpha$ determines the sign and magnitude of the macrostress in the sheath and in the interior of the wire. Based on the CTEs of the constituents, $\alpha(Mg^{11}B_2) = 8.3 \times 10^{-6}$/K [49], α(Monel) = 14×10^{-6}/K [50], and α(Nb) = 7.3×10^{-6}/K [51], a compressive axial stress should be generated in $Mg^{11}B_2$, compensated by the tensile stress in the Monel sheath. In the wires sintered at 700°C and 750°C, with some amount of unreacted Mg phase and ^{11}B rich phase, the same consideration is supposed to include Mg ($\alpha = 24.8\times10^{-6}$/K) [52] and ^{11}B ($\alpha = 6\times10^{-6}$/K) [53] as well as microstructure features (e.g. possible pores and cracking). The resultant effect is highly sensitive to the conditions on the contact between the Monel tube and the $Mg^{11}B_2$ composite interior. Yet another explanation of this partial stress relaxation in the axial direction could be the presence of oriented cracks and pores arising from contraction during the sintering process and the pores originating from the $Mg^{11}B_2$ phase formation reaction in the heat-treatment procedure.

Figure 7-4(a-d) shows the microstructure in the longitudinal direction of the $Mg^{11}B_2$ wires sintered at 700°C, 750°C, and 800°C. These secondary electron image (SEI) observations indicate that aggregation occurs along with the presence of some small pores and microcracks in the 700°C and 750°C wires (Figure 7-4(a, b)), while cracking and pores are more pronounced in the wire heat-

treated at 800°C (Figure 7-4(c, d)).

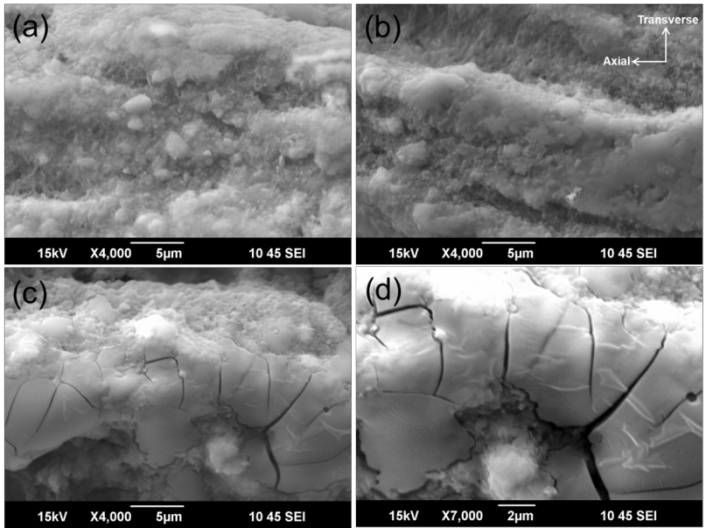

Figure 7-4. Low-vacuum SEM images of longitudinal sections of $Mg^{11}B_2$ wires heat-treated at (a) 700°C, (b) 750°C, and (c, d) 800°C.

As the heat-treatment temperature increases, the aggregation of the $Mg^{11}B_2$ growth proceeds continuously while creating pores. As a result of the aggregation, $Mg^{11}B_2$ has a porous structure, and it can be easily damaged by thermal stress caused by the temperature drop from above 700°C to room temperature.

Although the pores provide a precondition for the cracking-susceptible microstructure, the actual origin and mechanism of stress generation is twofold. First, due to the difference in CTE between the Monel/Nb sheath and the superconducting material, macrostress is generated, which in circumstances of porous microstructure leads to stress concentration. Second, due to the anisotropic thermal expansion of $Mg^{11}B_2$ (hexagonal crystal structure, $\alpha(a) = 5.4 \times 10^{-6}$/K, $\alpha(c) = 11.4 \times 10^{-6}$/K [54]), when the grains are randomly oriented, microstresses can also be generated. Although the overall average volume of these stresses is zero, the localised stresses can reach very large values, up to ~1 GPa accordingly to our estimates. Thus, through these thermal mechanisms, very high magnitude and locally concentrated stress fields are generated, leading to microcrack formation conditions. The exact morphology, phase composition, and other details of the microstructure play roles in the actual stress state of the superconducting material. Thus, the more porous structure of the 800°C sample makes it more cracking-prone than the lower temperature samples (700°C and 750°C) with more homogeneous structures. Also, while in less pure samples (700°C and 750°C), the local stress/strain fields can be accommodated by the plastically soft metallic Mg phase, this mechanism is substantially suppressed in the most pure (800°C) sample, and thus, cracks are more easily formed in the 800°C sample. Therefore, due to these two mechanisms, the most significant cracks on the scale of several microns are formed in the 800°C sample.

Furthermore, the brittle fracturing leads to extensive cracking in the $Mg^{11}B_2$ structure, as seen in

Figure 7-4(c, d), resulting in a harmful effect on the transport J_c properties in $Mg^{11}B_2$ wire [55, 56]. In fact, it was previously reported in our research results that the wire sintered at 800°C did not show a transport J_c, even though the sample was fully reacted with a high $Mg^{11}B_2$ superconducting phase fraction [57]. On the other hand, the wire sintered at 750°C has a superior transport critical current density, $J_c = 2 \times 10^4$ A/cm^2 at 4.2 K and 5 T compared with the multifilament wire manufactured by the National Institute for Fusion Science (NIFS) [57]. Therefore, based on the above discussion, the cracks and the pores have a detrimental influence on J_c through fracturing of the inter-grain connections, while, at the same time, these defects act as stress relief factors in the $Mg^{11}B_2$ wire sintered at 800°C. In other word, the electrical current can be reduced easily with less grain connectivity in the microstructure and thus the stress relief can be occurred as a result of the defect growth in the grain with the decreasing current carrying capacity in the superconductor.

The superconducting transition temperature (T_c) was observed at a temperature of 36.5 K and 36.9 K, for the samples sintered at 700°C and 800°C, respectively [57]. Compared to the reported results, e.g. 39.2 K in [58], the lower T_c in the present samples is most likely due to the presence and complex interactions of different types of MgB_2 lattice defects, such as lattice strains/stresses, poor crystallinity, the presence of point defects and defects with higher dimensions, and issues with chemical purity and phase purity (e.g. the presence of small amounts of MgO) [59]. The exact role of each factor might be difficult to address, however due to the intertwined nature of these mechanisms [60].

7.4. Conclusions

Due to its relevance to the superconducting properties, the stress state of $Mg^{11}B_2$ wires sintered (heat-treated) at different temperatures was investigated using neutron diffraction. We found that the stress in $Mg^{11}B_2$ is due to two contributions: one is the thermally generated hydrostatic microstress most clearly manifested in the transverse direction; the other is the contribution of the thermally generated macrostress, which has a uniaxial nature due to the “wire sheath-interior" interaction with its effects in the axial direction and/or possibly some contribution to stress relaxation due to oriented microcracking. We also found that, as the sintering temperature increases to 800°C, it leads to the formation and growth of cracks in the superconducting ceramic as well as presence of some pores. These defects are, most likely, not related to the thermally generated stress, in so far as it is the lowest in the 800°C sintered sample, but initiated during the sintering process itself and most likely involving the phase transformation mechanism. The extended cracking negatively affects the superconducting properties in the $Mg^{11}B_2$ wire, to the point of total loss of the superconductivity, even though the $Mg^{11}B_2$ superconducting ceramic sintered at 800°C is the most pure and would be expected to have better properties because the high sintering temperature gives rise to stress relief in the $Mg^{11}B_2$ wire. In other words, the noticeable relaxation of the residual stresses in the axial and the transverse directions implies that the poor transport J_c value is caused by insufficient grain connection in the $Mg^{11}B_2$ wire. Overall, the micromechanical and structural features of the $Mg^{11}B_2$-based wires are essential for their

performance, and neutron diffraction seems to be an appropriate analytical tool for assessment of the residual stress state as well as the crystallographic anisotropy (texture).

7.5. References

1. Devred, A. et al. Challenges and status of ITER conductor production. Supercond. Sci. Technol. 27, 044001, 2014.

2. Boutboul, T. et al. Status of the Procurement of the European Superconductors for the ITER Magnets. IEEE Trans. Appl. Supercond. 24, 6001004, 2014.

3. Mitchell, N. & Devred, A. The ITER magnet system: Configuration and construction status. Fusion Eng. Des. 123, 17-25, 2017.

4. Noda, T., Takeuchi, T. & Fujita, M. Induced activity of several candidate superconductor materials in a tokamak-type fusion reactor. J. Nucl. Mater. 329-333, 1590-1593, 2004.

5. Glowacki, B.A. & Nuttall, W.J. Assessment of liquid hydrogen cooled MgB_2 conductors for magnetically confined fusion. J. Phys. Conf. Ser. 97, 012333, 2008.

6. Yao, W. et al. A Solid Nitrogen Cooled MgB_2 "Demonstration" Coil for MRI Applications. IEEE Trans. Appl. Supercond. 18, 912-915, 2008.

7. Tomsic, M. et al. Overview of MgB_2 Superconductor Applications. Int. J. Appl. Ceram. Technol. 4, 250-259, 2007.

8. Iwasa, Y. Towards liquid-helium-free, persistent-mode MgB_2 MRI magnets: FBML experience. Supercond. Sci. Technol. 30, 053001, 2017.

9. Nagamatsu, J. et al. Superconductivity at 39 K in magnesium diboride. Nature 410, 63–64, 2001.

10. Buzea, C. & Yamashita, T. Review of the superconducting properties of MgB_2. Supercond. Sci. Technol. 14, 115-146, 2001.

11. Patel, D.et al. Rational design of MgB_2 conductors towards practical applications. Cryogenics 63, 160, 2014.

12. Wang, D. et al. Transport properties of multifilament MgB_2 long wires and coils prepared by an internal Mg diffusion process. Supercond. Sci. Technol. 30, 064003, 2017.

13. Hossain, M. S. A. et al. The roles of CHPD: Superior critical current density and n-value obtained in binary in situ MgB_2 cables. Supercond. Sci. Technol. 27,095016, 2014.

14. Devred, A. et al. Status of ITER Conductor Development and Production. IEEE Trans. Appl. Supercond. 22, 4804909, 2012.

15. Baig, T.et al. Conceptual designs of conduction cooled MgB_2 magnets for 1.5 and 3.0 T full body MRI systems. Supercond. Sci. Technol. 30, 043002, 2017.

16. Ogitsu, T., Schwegler, E. & Galli, G. β-Rhombohedral Boron: At the Crossroads of the Chemistry of Boron and the Physics of Frustration. Chem. Rev. 113, 3425–3449, 2013.

17. Chkhartishvili, L. Isotopic effects of boron (Review). Trends Inorg. Chem. 11, 105–167, 2009.

18. Sears, V. F. Neutron scattering lengths and cross sections, Neutron News 3, 26-37, 1992.

19. Eisterer, M. et al. Neutron irradiation of MgB_2 bulk superconductors. Supercond. Sci. Technol. 15, L9-L12, 2002.

20. Wilke, R. H. T., Bud'ko, S. L. & Canfield, P. C. Systematic study of the superconducting and

normal-state properties of neutron-irradiated MgB_2. Phys. Rev. B 73, 134512, 2006.

21. Putti, M. et al. Neutron irradiation of $Mg^{11}B_2$: From the enhancement to the suppression of superconducting properties. Appl. Phys. Lett. 86, 112503, 2005.

22. Mooring, F. P., Monahan, J. E. & Huddleston, C. M. Neutron cross sections of the boron isotopes for energies between 10 and 500 keV. Nucl. Phys. 82, 16–32, 1966.

23. Cheng, F. et al. Improved superconducting properties in the $Mg^{11}B_2$ low activation superconductor prepared by low-temperature sintering. Sci. Rep. 6, 25498, 2016.

24. Mitchell, N. et al. Reversible and irreversible mechanical effects in real cable-in-conduit conductors. Supercond. Sci. Technol. 26, 114004, 2013.

25. Nijhuis, A. A solution for transverse load degradation in ITER Nb_3Sn CICCs: Verification of cabling effect on Lorentz force response. Supercond. Sci. Technol. 21,054011, 2008.

26. Arp, V. Stresses in superconducting solenoids. J. Appl. Phys. 48, 2026-2036, 1977.

27. Bajas, H., Durville, D., Ciazynski, D. & Devred, A. Approach to Heterogeneous Strain Distribution in Cable-In-Conduit Conductors Through Finite Element Simulation. IEEE Trans. Appl. Supercond. 22, 4803104, 2012.

28. Osamura, K. et al. Local strain and its influence on mechanical–electromagnetic properties of twisted and untwisted ITER Nb_3Sn strands. Supercond. Sci. Technol. 25, 054010, 2012.

29. Kitaguchi, H., Kumakura, H. & Togano, K. Strain Effect in MgB_2/Stainless Steel Superconducting Tape. Physica C 363, 198–201, 2001.

30. Kitaguchi, H. &Kumakura, H. Superconducting and mechanical performance and the strain effects of a multifilamentary MgB_2/Ni tape. Supercond. Sci. Technol. 18, S284–S289, 2005.

31. Katagiri, K. et al. Stress–strain effects on powder-in-tube MgB_2 tapes and wires. Supercond. Sci. Technol. 18, S351–S355, 2005.

32. Nishijima, G. et al. Mechanical properties of MgB_2 superconducting wires fabricated by internal Mg diffusion process. Supercond. Sci. Technol. 25, 054012, 2012.

33. Harjo, S. et al. Residual Strains in ITER Conductors by Neutron Diffraction. Mat. Sci. Forum 777, 84-91, 2014.

34. Scheuerlein, C. et al. Residual strain in the Nb_3Sn 11 T dipole magnet coils for HL-LHC, Supercond. Sci. Technol. 30, 125002, 2017.

35. Hutchings, M. T., Withers, P. J., Holden, T. M. & Lorentzen, T. Introduction to the Characterization of Residual Stress by Neutron Diffraction (Taylor & Francis, Boca Raton London New York Singapore, 2005) pp. 1-272.

36. Markovskii, L. Y. Chemistry of magnesiothermal preparation of boron. Electron. Technol. 3, 95–102, 1970.

37. Lutterotti, L., Matthies, S. &Wenk, H.-R. MAUD (Material Analysis Using Diffraction) Program. Available from: http://maud.radiographema.eu/ (2017).

38. Kirstein, O., Luzin, V. & Garbe, U.The Strain-Scanning Diffractometer Kowari, Neutron News 20(4), 34-36, 2009.

39. Kröner, E. Elastic moduli of perfectly disordered composite materials. J. Mech. Phys. Solids. 15, 319-329, 1967.

40. Hutchings, M. T., Withers,P. J.,Holden, T. M. & Lorentzen, T. Introduction to the Characterization of Residual Stress by Neutron Diffraction (Taylor & Francis, Boca Raton London New York Singapore, 2005) pp. 213-273.

41. Tomé, C. N., Wenk, H. R. & Kocks, U. F. Texture and Anisotropy: Preferred Orientations in Polycrystals and Their Effect on Materials Properties (Cambridge University Press, 2000).

42. Hilgenkamp, H & Mannhart, J. Grain boundaries in high T_c superconductors, Rev. Mod. Phys. 74, 485-549, 2002.

43. Bhagurkar, A. G. et al. Microstructural evolution in infiltration-growth processed MgB_2 bulk superconductors. J. Am. Ceram. Soc. 100, 2451–2460, 2017.

44. Giunchi, G., Orecchia, C., Malpezzi, L. & Masciocchi, N. Analysis of the minority crystalline phases in bulk superconducting MgB_2 obtained by reactive liquid Mg infiltration. Physica C 433, 182–188, 2006.

45. Giunchi, G., Cavallin, T., Bassani, P. & Guicciardi, S. The mechanical properties of the MgB_2 bulk materials obtained by reactive liquid Mg infiltration. AIP Conf. Proc. 986, 396-404, 2008.

46. Eshelby, J. D. The determination of the elastic field of an ellipsoidal inclusion and related problems. Proc. R. Soc. Lond. A241, 376-396, 1957.

47. Eshelby, J. D. The Elastic Field outside an Ellipsoidal Inclusion. Proc. R. Soc. Lond. A252, 561-569, 1959.

48. Massalski, T. B., Okamoto, H., Subramanian, P. R. & Kacprzak, L. Binary Alloy Phase Diagrams. (ASM International, 1990).

49. Goldacker, W., Schlachter, S. I., Zimmer, S. & Reiner, H. High transport currents in mechanicallyreinforced MgB_2 wires. Supercond. Sci. Technol. 14, 787-793, 2001.

50. National Bureau of Standards Publications (U.S.). Thermal expansion of nickel, Monel metal, Stellite, stainless steel, and aluminium, 497-519 (Scientific Papers of the Bureau of Standards17, 1921).

51. Cverna, F. ASM Ready Reference: Thermal Properties of Metals, 9-13 (ASM International 06702G, 2002).

52. Perry, D. L. & Phillips, S. L. Handbook of Inorganic Compounds (CRC Press, 1995) p. 234.

53. Holcombe, Jr., C. E. et al. Physical-Chemical Properties of beta-Rhombohedral Boron. High Temp. Sci. 5, 349–357, 1973.

54. Jorgensen, J. D., Hinks, D. G. & Short, S. Lattice Properties of MgB_2 versus Temperature and Pressure. Phys. Rev. B 63, 224522, 2001.

55. Jiang, C. H., Kumakura, H. & Dou, S. X. Enhancement of the low-field J_c properties of MgB_2/Fe tapes by a modified in situ process. Supercond. Sci. Technol. 20, 1015–1018, 2007.

56. Liu, Y., Xue, F. & Gou, X. The Influence of Dispersedly Distributed Cracks on Critical Current of the Nb_3Sn Strand. J. Supercond. Nov. Magn. 1-6, 2017.

57. Qiu, W. et al. Improvement in the transport critical current density and microstructure of isotopic $Mg^{11}B_2$ monofilament wires by optimizing the sintering temperature. Sci. Rep. 6, 36660, 2016.

58. Margadonna, S, et al. Phase in homogeneities and lattice expansion near T_c in the $Mg^{11}B_2$

superconductor. J. Phys.: Condens. Matter 13, L795-L802, 2001.

59. Kim, J H, et al. The effects of sintering temperature on superconductivity in MgB_2/Fe wires, Supercond. Sci. Technol. 20, 448–451, 2007.

60. Flükiger, R. MgB_2 Superconducting Wires, Basics and Applications (World Scientific, 2016).

Chapter 8

Conclusions and Future Prospects

8.1. Conclusions

Up to this time, most research and work have been focused on the NbTi and Nb_3Sn superconductors for application in the International Thermonuclear Experimental Reactor (ITER). Nevertheless, we still need understand and study at least the possibility that MgB_2 superconductor can replace NbTi which has been used for the poloidal coils and the correction coils in the ITER fusion reactor. The final goal of this thesis was to demonstrate the possibility that MgB_2 superconducting material could be used in the range of low and moderate magnetic field of 5 – 6 T for fusion energy applications such as an ITER-type tokamak magnet. It has been shown that the boron- 11 isotope (^{11}B) powder which has the smallest particle size and the lowest crystallinity is the most suitable boron precursor instead of using the boron- 10 (^{10}B) rich powder known as the natural boron, and it has a normal T_c value in the range of 36–37 K. This result should be useful for guidance in the manufacture of the boron-11 based MgB_2 superconducting wire.

For the best J_c performance of the MgB_2 superconductor, the combination of the cold high pressure densification (CHPD) with the hot isostatic pressure treatment (HIP) during the manufacturing process has been tried and demonstrated. This processing technique should be useful for the further practical application of industrially viable and economical MgB_2 with outstanding J_c values. Furthermore, boron-11 rich powder was used which was doped with carbon in order to control the manufacturing conditions for superior superconducting properties compared with boron-10 rich MgB_2. In this thesis work, glycine was used as a carbon precursor, and the bulk MgB_2 superconductor had enhanced critical current density (J_c) over the entire field in contrast with the boron-10 rich powder based MgB_2 and the high-purity boron-11 based MgB_2.

It has been first proved clearly that the monofilament of the boron-11 based MgB_2 wire obtained the best transport critical current density (J_c) = 2×10^4 A/cm^2 at 4.2 K and 5 T, which is even comparable to multi-filament boron-11 based MgB_2 wires reported in other work involving control of the inter grain connections of the MgB_2. It will be challenging work to devise the construction guidelines for manufacturing the boron-11 based MgB_2 wire to be used in the fusion reactor in magnet coils. Finally, parallel to this result, this thesis also demonstrates the correlation between the fabrication conditions and the transport critical current density (J_c) of the boron- 11 based MgB_2 wire by the neutron diffraction method. That there are applied stress/strain effects is well known, and there are numerous research and study results, but the residual stress/strain of the boron-11 based MgB_2 superconductor was never measured or reported before. In these results, we have performed the analysis of the boron- 11 based MgB_2 wire by using the neutron diffraction method to connect the full quantitative residual stress analysis with the defect, such as cracks and pores, and the superconducting properties. These results will be useful guidelines for attempting the practical production and testing for the real implementation of a prototype of the 2nd generation

superconducting cable for the fusion reactor.

8.2. Future Prospects

It is anticipated that the outcomes of this thesis will provide a strong assessment of the mechanical properties, design, thermomechanical processing routes, and performance of the next-generation boron-11 based MgB_2 ($Mg^{11}B_2$) superconducting cables. The study of these properties, which are characteristic of the formation mechanism and directly linked to the superconducting performance, will allow optimization of the fabrication process for the cables made of the MgB_2 multifilament wires. This thesis work will lay down the technological foundation for the industrial production of the $Mg^{11}B_2$ based cables with excellent properties and performance for the fusion reactor application. Specifically, $Mg^{11}B_2$ can replace NbTi which has been used for poloidal and correction field coils in the fusion reactor manufactured by techniques achieved in the Chapter 4.
For practical application, study of the mechanical properties and performance of the $Mg^{11}B_2$ superconductors derived from various production routes and multifilament wire designs are needed. Indeed, the activation properties of $Mg^{11}B_2$ superconducting wire in an operation environment under heavy neutron irradiation are also extremely important for targeting fusion and high energy physics applications. The results will be used in local-scale practical application. A longer and higher critical current density $Mg^{11}B_2$ multi-cored cable is to replace the existing copper coil in the magnetized plasma device to test this superconducting coil in a plasma environment in order to generate stronger magnetic fields. At the next step, a potential use of the cables on larger-scale facilities will be assessed.

Appendix

Publications

1. **Hyunseock. Jie**, Yusuke Yamauchi, Vladimir Luzin, Md. Shahriar A, Hossain, "Micromechanics modelling for the $Mg^{11}B_2$ superconductors", Under preparation, 2018.
2. **Hyunseock Jie**, Wenbin Qiu, Jeonghun Kim, Keun Hwa Chae, Hyung-il Choi, Vladimir Luzin, Vladimir Levchenko, Yusuke Yamauchi, Md. Shahriar Al Hossain, "Assessment of Isotopic Boron Powders for the fabrication of low activation $Mg^{11}B_2$ superconductor for fusion magnets", Submitted, 2018.
3. **Hyunseock Jie**, Wenbin Qiu, Jung Ho Kim, Yusuke Yamauchi, Vladimir Luzin, Md. Shahriar A, Hossain, "Evaluation of residual stress and texture in isotope based $Mg^{11}B_2$ superconductor using neutron diffraction", Revision process in scientific report, 2018.
4. Dipak Patel, Md Shahriar Al Hossain, Wenbin Qiu, **Hyunseock Jie**, Yusuke Yamauchi, Minoru Maeda, Mike Tomsic, Seyong Choi & Jung Ho Kim, "Solid cryogen: a cooling system forfuture MgB_2 MRI magnet", *Sci. Rep. 7, 43444, 2017*.
5. **Hyunseock Jie**, Wenbin Qiu, Motasim Billah, Mislav Mustapic, Dipak Patel, Zongqing Ma, Daniel Gajda, Andrzej Morawski, Tomasz Cetner, Mohammed Shahabuddin, Ekrem Yanmaz, Matt Rindfleisch, Jung Ho Kim, Md Shahriar A Hossain, "Superior transport J_c obtained in in-situ MgB_2 wires by tailoring the starting materials and using a combined cold high pressure densification and hot isostatic pressure treatment", *Scr. Mater., vol. 129, pp. 79-83, 2017*.
6. Qi Cai, Qianying Guo, Yongchang Liu, Zongqing Ma, Huijun Li, Wenbin Qiu, Dipak Patel, **Hyunseock Jie**, Jung Ho Kim, Mehmet Somer, Ekrem Yanmaz, Arnaud Devred, Vladimir Luzin, Amanullah Fatehmulla, Wazirzada Aslam Farooq, Daniel Gajda, Yoshio Bando, Yusuke Yamauchi, Subrata Pradhan and Md. Shahriar A. Hossain, "Doping-Induced Isotopic $Mg^{11}B_2$ Bulk Superconductor for Fusion Application", *Energies, 10, 409, 2017*.
7. Ananya Kundu, Dipak Patel, Nitish Kumar, Arun G. Panchal, Wenbin Qiu, **Hyunseock Jie**, Zongqing Ma, Ekrem Yanmaz, Mohammed Shahabuddin, Jung Ho Kim, Subrata Pradhan, Md Shahriar Al Hossain, "Fabrication, Transport Current Testing, and Finite Element Analysis of MgB_2 Racetrack Coils", *J. Supercond. Nov. Magn., Volume 30, Issue 10, pp 2957–2962, 2017*.
8. Wenbin Qiu, **Hyunseock Jie**, Dipak Patel, Yao Lu, Vladimir Luzin, Arnaud Devred, Mehmet Somer, Mohammed Shahabuddin, Jung Ho Kim, Zongqing Ma, Shi Xue Dou & Md. Shahriar Al Hossain, "Improvement in the transport critical current density and microstructure of isotopic $Mg^{11}B_2$ monofilament wires by optimizing the sintering temperature", *Sci. Rep. 6, 36660, 2016*.